Study of S=-2 Nuclear Systems with Hybrid Emulsion Method(Dissertation_全文)

AUTHOR(S):

Ichikawa, Atsuko

Study of $S = -2$ Nuclear Systems with Hybrid Emulsion Method

Atsuko Ichikawa

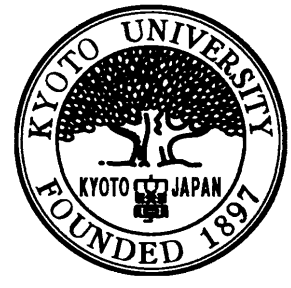

Abstract

A hybrid emulsion experiment KEK-PS E373 was carried out to study double-strangeness nuclei produced via Ξ^- hyperon capture at rest with the expectation of ten times larger statistics than a previous experiment. The experiment employed a 1.66 GeV/c separated K^- beam and 69 l nuclear emulsion. The Ξ^- hyperons were produced in a diamond target via the (K^-, K^+) reaction and were brought to rest in the emulsion. The (K^-, K^+) reaction was tagged by a spectrometer system. Scintillating-fiber detectors were used both to measure the Ξ^- hyperon track and to select events to be analyzed in the emulsion. Tracks of the Ξ^- candidates were searched for and traced in the emulsion by a newly-developed automatic track scanning system.

Until now, 6% of the total emulsion has been analyzed. We found one twin Λ hypernuclei event and one double-Λ hypernucleus at Ξ^- hyperon stopping points. The two events were reconstructed kinematically using the information about the ranges and angles of the tracks.

The twin-hypernuclei event was interpreted as the decay from a Ξ^-+^{14}N atomic state to ${}^{5}_{\Lambda}$He+${}^{5}_{\Lambda}$He+^{4}He+n. The species of the Ξ^--atom and the fragmentation products were uniquely identified for the first time for twin-hypernuclei events.

A sequential weak decay of the double-Λ hypernucleus was observed. The event was interpreted as a two-body decay, $\Xi^- + {}^{12}\mathrm{C} \rightarrow {}^{10}_{\Lambda\Lambda}\mathrm{Be} + t$, or a decay involving neutrons. Combined with the result of the previous experiment, the allowed region for the $\Lambda\Lambda$ interaction energy ($\Delta B_{\Lambda\Lambda}$) are -1.11 ± 0.21 MeV and $+1.93 \pm 0.21$ MeV for ${}^{10}_{\Lambda\Lambda}$Be, and $+4.9 \pm 0.8$ MeV and 0.94 ± 0.47 MeV for ${}^{13}_{\Lambda\Lambda}$B.

Contents

Chapter 1

Introduction

1.1 Physics of $S = -2$ nuclear systems

Since Gell-Mann and Zweig introduced the idea of quarks and flavor $SU(3)$ symmetry ($SU(3)_f$) in 1964, many attempts have been made to explain the mass spectra of hadrons and the interaction between hadrons based on that idea. The interaction between quarks are described explicitly by quantum-chromodynamics (QCD), a theory of strong interaction. Although the exact calculation is not yet succeeded due to the non-perturbative feature of QCD, phenomenological quark models have achieved a great success to explain the baryon mass spectra utilizing the characteristics of the flavor $SU(3)$ symmetry or spin-flavor $SU(6)$ symmetry. Especially the mass difference between the octet baryons and decuplet baryons is well explained by the color-magnetic interaction,

$$\Delta_c = -\sum_{i>j} \vec{\sigma_i} \cdot \vec{\sigma_j} \vec{\lambda_i} \cdot \vec{\lambda_j} M(m_i, m_j), \tag{1.1}$$

where the σ_i and λ_i are the spin Pauli matrix and flavor Gell-Mann matrix for the i-th quark and m_i is the mass of the i-th quark and M measures the QCD interaction strength. The term corresponds to the lowest-order gluon exchange interaction. In the $SU(3)_f$-symmetry limit, i.e. $m_s = m_u = m_d = 0$ and for color-singlet hadrons containing only quarks and no anti-quarks, the term becomes

$$\Delta_c = [8N - \frac{1}{2}C_6 + \frac{4}{3}J(J+1)]\overline{M}, \tag{1.2}$$

where $\overline{M} = M(0,0)$, N is the total number of quarks, J is their angular momentum, and C_6 is an eigenvalue of the color-spin $SU(6)$ Casimir operator. The value of the term is $\Delta_c = -8\overline{M}$ for the octet baryons and $\Delta_c = +8\overline{M}$ for the decuplet baryons, giving heavier masses for the decuplet baryons.

As for the interaction between baryons, the nucleon-nucleon (NN) interaction is known to obey $SU(2)$ isospin symmetry very well, which are considered to have revealed as a part of $SU(3)_f$. Only the isospin $T = 0$ channel has a binding state as deuteron. At a short distance, a hard core exists in the NN interaction. It

is explained by Pauli-blocking and the color-magnetic interaction. The energy difference due to the color-magnetic interaction between two nucleons in a very close distance and two free nucleons is naively calculated to be

$$\begin{aligned} \Delta M(NN^1S_0) &\equiv \Delta_c(NN^1S_0)) - \Delta_c(N) \times 2 \\ &= +24\overline{M}, \end{aligned} \tag{1.3}$$

giving the repulsive force at a short distance.

What would happen when the NN interaction is extended to the hyperon-nucleon (YN) and hyperon-hyperon (YY) interactions? Figure1.1 shows the irreducible representations for the $SU(3)_f$ two-baryon systems. From the studies on the NN interaction, information about only 27_s and $\overline{10}_a$ multiples have been obtained. The YN interaction have been studied experimentally via the YN scattering and hypernuclei. Although the information is still poor compared to the NN sector, multiplets except for 1_s can be studied through these experimental results. As for the 1_s sector, which is a doubly strange system, only the indirect and limited information has been obtained from experiments. The experimental status is briefly reviewed in the next section. With the most symmetric configuration of the 1_s sector ($J^\pi = 0^+$, flavor singlet), C_6 has the largest eigenvalue 144. Hence, the color-magnetic term, Δ_c becomes negative value,i.e. $\Delta_c(1_s) = -24\overline{M}$, and the energy difference between the six quarks in this configuration and two free baryons becomes

$$\begin{aligned} \Delta M(1_s) &\equiv \Delta_c(BB, 1_s) - \Delta_c(B) \times 2 \\ &= -8\overline{M}. \end{aligned} \tag{1.4}$$

giving an attractive force at a short distance. In 1977, Jaffe proposed the possible existence of a 1_s six-quark state confined in a bag using the MIT-bag model with this color-magnetic interaction[1]. The state was labeled as the H-dibaryon. It comprises two up, two down and two strange quarks. It's quantum numbers are $J^{PC} = 0^{++}, I = 0, S = -2$ and $B = 2$. The predicted value of the mass of the dibaryon is 2150 MeV/c^2, which is 80 MeV/c^2 below two Λ's threshold, and hence the state was expected to be stable against strong decay. Since then, it's mass has been calculated in various theoretical models. A variety of QCD-in-spired models predicted widely-ranging H masses from ones below NN threshold to those above 2Λ mass. A review of the theoretical status can be found in Ref.[2]. Experimentally, many searches have been performed with various techniques using protons, heavy ions, kaons, etc. However, no evidence of its existence has been established. Reviews of the previous and ongoing H-search experiments can be found in Refs.[3, 4].

The information about the ΛN interaction has been obtained through the studies on single-Λ hypernuclei. In the same way, the information about the $\Lambda\Lambda$ interaction can be obtained through the studies on double-Λ hypernuclei. Firstly, from the mass of a double-Λ hypernucleus, the $\Lambda\Lambda$ interaction energy defined by

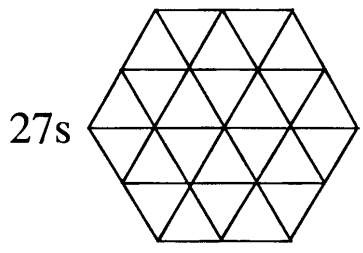

27s

S=0 NN(T=1)
S=-1 ΣN(T=3/2) ΣN-ΛN(T=1/2)
S=-2 ΣΣ(T=2) ΞN-ΣΛ-ΣΣ(T=1) ΞN-ΣΣ-ΛΛ(T=0)
S=-3 ΞΣ(T=3/2) ΞΣ-ΞΛ(T=1/2)
S=-4 ΞΞ(T=1)

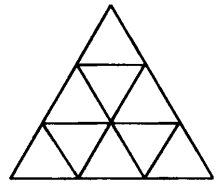

$\overline{10}$a

S=0 NN(T=0)
S=-1 ΣN-ΛN(T=1/2)
S=-2 ΞN-ΣΛ(T=1)
S=-3 ΞΣ(T=3/2)

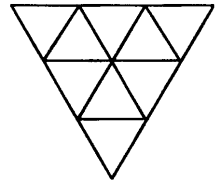

10a

S=-1 ΣN(T=3/2)
S=-2 ΞN-ΣΛ-ΣΣ(T=1)
S=-3 ΞΣ-ΞΛ(T=1/2)
S=-4 ΞΞ(T=0)

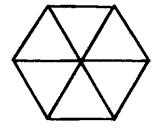

8s

S=-1 ΣN-ΛN(T=1/2)
S=-2 ΞN-ΣΛ(T=1) ΞN-ΣΣ-ΛΛ(T=0)
S=-3 ΞΣ-ΞΛ(T=1/2)

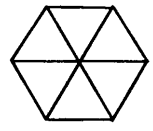

8a

S=-1 ΣN-ΛN(T=1/2)
S=-2 ΞN-ΣΛ-ΣΣ(T=1) ΞN(T=0)
S=-3 ΞΣ-ΞΛ(T=1/2)

1s ●

S=-2 ΞN-ΣΣ-ΛΛ(T=0)

Figure 1.1: Irreducible representations for two-baryon system based on $SU(3)_f$.

$$\Delta B_{\Lambda\Lambda}({}^{A}_{\Lambda\Lambda}Z) = B_{\Lambda\Lambda}({}^{A}_{\Lambda\Lambda}Z) - 2B_{\Lambda}({}^{A-1}_{\Lambda}Z) \quad (1.5)$$

$$= 2M({}^{A-1}_{\Lambda}Z) - M({}^{A-2}Z) - M({}^{A}_{\Lambda\Lambda}Z) \quad (1.6)$$

can be extracted. Here the $B_{\Lambda\Lambda}$ and B_{Λ} are the binding energy of the two Λ's in the double-Λ hypernucleus $({}^{A}_{\Lambda\Lambda}Z)$ and that of the Λ in the single-Λ hypernucleus $({}^{A-1}_{\Lambda}Z)$, respectively. It's sign would indicate whether the $\Lambda\Lambda$ interaction is attractive or repulsive as a whole in the nucleus. It's magnitude would give the strength of the interaction.

Double-Λ hypernuclei are deeply related to the H-dibaryon. The existence of the H would have a great influence on the ground state of nuclei with $S = -2$. If the H-mass (M_H) is lighter than the mass of two Λ's in a nucleus, the two Λ's could decay into H by the strong interaction. In a calculation made by Kerbikov for the case of ${}^{6}_{\Lambda\Lambda}$He [5], the rate of strong decay was found to be $10^{18} \sim 10^{20} s^{-1}$, much more rapid than the weak decay rate($\sim 10^{10} s^{-1}$). Therefore, the binding energy of two Λ's in a nucleus provides the lower limit of the H-mass,

$$M_H \geq 2m_{\Lambda} - B_{\Lambda\Lambda}. \quad (1.7)$$

Couplings to the $\Xi^0 n$ and $\Xi^- p$ channels would also have an influence on double-Λ hypernuclei because the mass of $\Lambda\Lambda$ is smaller than those of $\Xi^0 n$ and $\Xi^- p$ only by 23 and 28 MeV/c^2, respectively. This is quite different from the case of nuclei with $S = -1$, where the mass of ΛN is smaller than ΣN by about 80 MeV/c^2. The ground state of nuclei with $S = -2$ might therefore be a mixed state of $\Lambda\Lambda$, $\Xi^0 n$ and $\Xi^- p$. In the extreme case, the $\Sigma\Sigma$ state may appear. In terms of baryon configuration, the $SU(3)_f$ 1_s state can be written as

$$|H> = \sqrt{\frac{1}{8}}|\Lambda\Lambda> + \sqrt{\frac{4}{8}}|N\Xi> - \sqrt{\frac{3}{8}}|\Sigma\Sigma> . \quad (1.8)$$

Hence the H state may appear as a result of the mixing of $\Lambda\Lambda$, ΞN and $\Sigma\Sigma$ states in a nucleus. The binding energy of $\Lambda\Lambda$ was calculated including or not-including the effect of the hyperon mixing in various manner such as few-body approaches using the effective $\Lambda\Lambda$ interaction derived from the one-boson-exchange models[6][7, 8, 9][10] and the quark-cluster model[11], and relativistic mean field approaches[12]. The calculated $\Delta B_{\Lambda\Lambda}$'s are ranging from -6 MeV to 10 MeV.

1.2 Experimental studies

Even today, a nuclear emulsion is the only detector that has a position resolution of a few μm. A hypernucleus having a energy of a few MeV can traverse a several μm before stopping and decaying. Double-Λ hypernuclei can, therefore, be identified in the emulsion by their sequential decay topology, that is, three vertices of the production and two decays.

Until now, three different emulsion experiments reported events in which double-Λ hypernuclei were emitted from Ξ^- stopping points [13, 14][15][16]. First two events were reported more than 30 years ago. The event reported by Danysz *et al.* was interpreted as ${}^{10}_{\Lambda\Lambda}$Be with $B_{\Lambda\Lambda} = 17.7 \pm 0.4$ MeV in a later analysis[14]. The event reported by Prowse was interpreted as ${}^{6}_{\Lambda\Lambda}$He with $B_{\Lambda\Lambda} = 10.9 \pm 0.8$ MeV. However, in these two event, the positive identification of the incoming track as that of a Ξ^- hyperon could not be made. Dalitz *et al.*[14] reported that the number of Ξ^-'s brought to rest was estimated to be one or two in the experiment by Danysz *et al.* and less than one in the experiment by Prowse. These two events were accompanied by two pionic sequential decays. For the event by Danysz *et al.*, the branching ratio for two pionic decays is naively estimated to be about 4%. Therefore, in these two experiments, the probability to find such events is extremely low. Furthermore, for the event by Danysz *et al.*, there were several interpretations in the original paper[13]. For the latter event, only the drawing is left, the emulsion having been lost, and there was no study or analysis of that event independent of the sole author.

For these two experiments, the emulsion was scanned all over the volume. Since the emulsion is sensitive to all charged particles, the measurement using only emulsion in charged particle beam is not effective in searching for a very rare reaction. In order to overcome this weak point, the emulsion-counter hybrid technique has been developed. In this technique, a specific reaction is selected by analyzing counter data and the vertex of the selected event is studied in detail by the emulsion. This technique has been successfully applied to the detection of short lived particles like charm and beauty hadrons with high energy beams at CERN and FermiLab[17, 18, 19]. In these days, the technique is drawing much attention by the possibility to detect the τ lepton produced via the ν_τ charged current interaction in order to search for the $\nu_\mu \rightarrow \nu_\tau$ oscillation[20, 21, 22]. Using this technique, an experiment E176 was carried out at the KEK Proton Synchrotron to study double-strangeness nuclei in 1980s. Production of Ξ^- hyperons via the (K^-, K^+) reaction was identified with a spectrometer system. They reported about 80 events of Ξ^- capture at rest and found one double-Λ hypernucleus. Since the Ξ^- production was tagged by measuring the (K^-, K^+) reaction with the counter system, this event is more reliable than the previously reported ones. However there remained two interpretations for that event. In this event, two charged particles including the double-Λ hypernucleus were emitted from the Ξ^- capture point. The two tracks are collinear within the error of measured angles. If it was a two-body decay from a Ξ^- capture, the produced double-Λ hypernucleus is ${}^{10}_{\Lambda\Lambda}$Be, giving a $\Lambda\Lambda$ binding energy of 8.5 ± 0.7 MeV. If it included a neutron emission and was a three-body decay, then the produced double-Λ hypernucleus is ${}^{13}_{\Lambda\Lambda}$B, giving a $\Lambda\Lambda$ binding energy of 27.6 ± 0.7 MeV. The lower limit of the H mass obtained from this one event is 2203.7 ± 0.7 MeV taking the limit deduced from the interpretation as ${}^{13}_{\Lambda\Lambda}$B.

The $\Delta B_{\Lambda\Lambda}$ was reported to be 4$\sim$5 MeV by Danysz *et al.*[13, 14] or Prowse[15], suggesting an attractive $\Lambda\Lambda$ interaction. E176 reported that $\Delta B_{\Lambda\Lambda}$ is $-4.8^{+0.7}_{-0.8}$

MeV in the case of ${}^{10}_{\Lambda\Lambda}$Be and +4.9±0.8 MeV in the case of ${}^{13}_{\Lambda\Lambda}$B. Experimentally, the former one is more favorable because the two tracks from the Ξ^- capture is collinear within the error and the probability of this topology to occur for a three-body fragment was estimated to be about 6%. Theoretically, Dover *et al.* argued that the later one is more favorable[23] based on the consideration about the production mechanism. For the events by Danysz *et al.* and E176, there is a possibility that the single-Λ hypernucleus produced from the decay of the double-Λ hypernucleus might be in an excited state. In such a case, $\Delta B_{\Lambda\Lambda}$ is overestimated. It is therefore still unknown whether the $\Lambda\Lambda$ interaction is attractive or repulsive, and our knowledge is limited to the upper limit for $\Delta B_{\Lambda\Lambda}$, i.e. 4∼5 MeV.

On the other hand, E176 reported two so-called "twin-hypernuclei" events, in which two single-Λ hypernuclei were emitted from a Ξ^- stopping point[24][25]. The mass of the system from which twin-hypernuclei are emitted can provide the information on the $\Xi^- N$ interaction. However, with the energy resolution of emulsions many more events are necessary to extract the $\Xi^- N$ interaction.

A nucleus, having absorbed a Ξ^- hyperon sometimes emits a double-Λ hypernucleus, twin single-Λ hypernuclei or a single-Λ hypernucleus. Since the energy release of the reaction, $\Xi^- + p \rightarrow \Lambda + \Lambda$, is only 28.2 MeV, the phase spaces available for double-Λ hyperfragment channels depend on $\Delta B_{\Lambda\Lambda}$ very much. Therefore, the branching ratio from a Ξ^- capture on a nucleus to a double-Λ hypernucleus or twin Λ hypernuclei is expected to be sensitive to $\Delta B_{\Lambda\Lambda}$. These branching ratios will provide information about $\Delta B_{\Lambda\Lambda}$ and the production mechanism of these hypernuclei through Ξ^- capture. However, to make quantitative arguments about the production rate, more statistics is needed.

A hybrid emulsion experiment (E373) was carried out at the KEK proton synchrotron using a 1.66 GeV/c separated K^- beam. The purpose of this experiment was to study double-strangeness nuclei produced via Ξ^- capture at rest with ten times larger statistics than the previous experiment. In this experiment, Ξ^- hyperons were produced in a diamond target via the (K^-, K^+) reaction and were brought to rest in the emulsion. The (K^-, K^+) reaction were tagged by a spectrometer system. The position and angle of the Ξ^- hyperon track was measured by a high-resolution tracking detector using scintillating microfibers. Fast protons and π^-'s produced via the decay of hypernuclei can be detected with the range counter of scintillating mono-fiber blocks located both upstream and downstream of the emulsion. Also, these scintillating fiber detectors have been used to select events in which the Ξ^- hyperons are likely to be stopped in the emulsion. For the selected events, tracks of the Ξ^- candidates were searched for and traced in the emulsion by an automatic track scanning system. Until now, 6% of the total emulsion has been analyzed. We found one twin Λ hypernuclei event and one double-Λ hypernucleus.

In Chapter 2, the method and technique used in the experiment are described. Procedure of the event selection by the spectrometer and image data analysis are described in Chapter 3. Procedure of the emulsion scanning are described

in Chapter 4 together with details about the automatic track scanning system. Calibration and error estimation for the range and energy measurement with emulsion is discussed in Chapter 5. In Chapter 6, the twin Λ hypernuclei event is described in detail and the result of the event reconstruction is presented. Details about the double-Λ hypernucleus event and it's interpretation are presented in Chapter 7. The obtained result was compared with theoretical estimate. The production rate of $S = -2$ nuclei from Ξ^- capture at rest is discusses in Chapter 8. Finally, the work is concluded in Chapter 9.

Chapter 2

Experimental procedure

2.1 Overview

The experiment was carried out at the K2 beam-line of the KEK 12GeV Proton Synchrotron (PS) in '98, '99 and 2000.

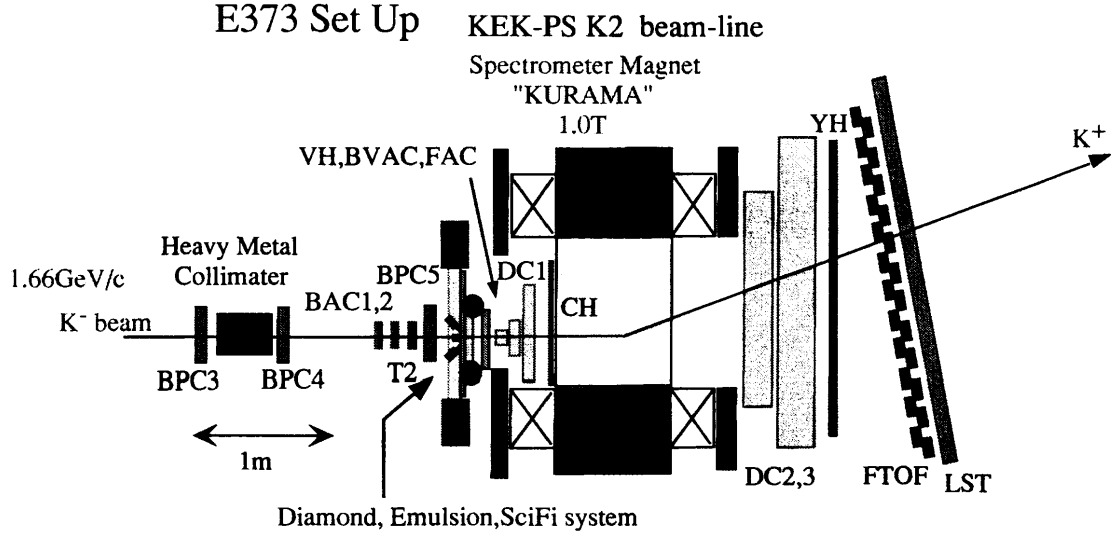

Figure 2.1: Schematic view of the experimental setup.

The experimental setup is shown in Figs.2.1, 2.2, 2.3 and 2.4. The Ξ^- hyperons were produced in a diamond target via the $p(K^-, K^+)\Xi^-$ quasi-free reaction. Some of them were slowed down and brought to rest in the nuclear emulsion stack placed downstream of the target. The stopped Ξ^- is expected to form Ξ^--atomic state with a nucleus in the emulsion at first, and to be absorbed by the nucleus with the strong interaction. Then a double-strangeness system will be produced with some probability. The (K^-, K^+) events were tagged by beam-line detectors and a spectrometer system. The position and angle of the Ξ^- hyperon track was measured by a high-resolution tracking detector using scintillating microfibers installed at the narrow gap between the target and the emulsion stack. Fast

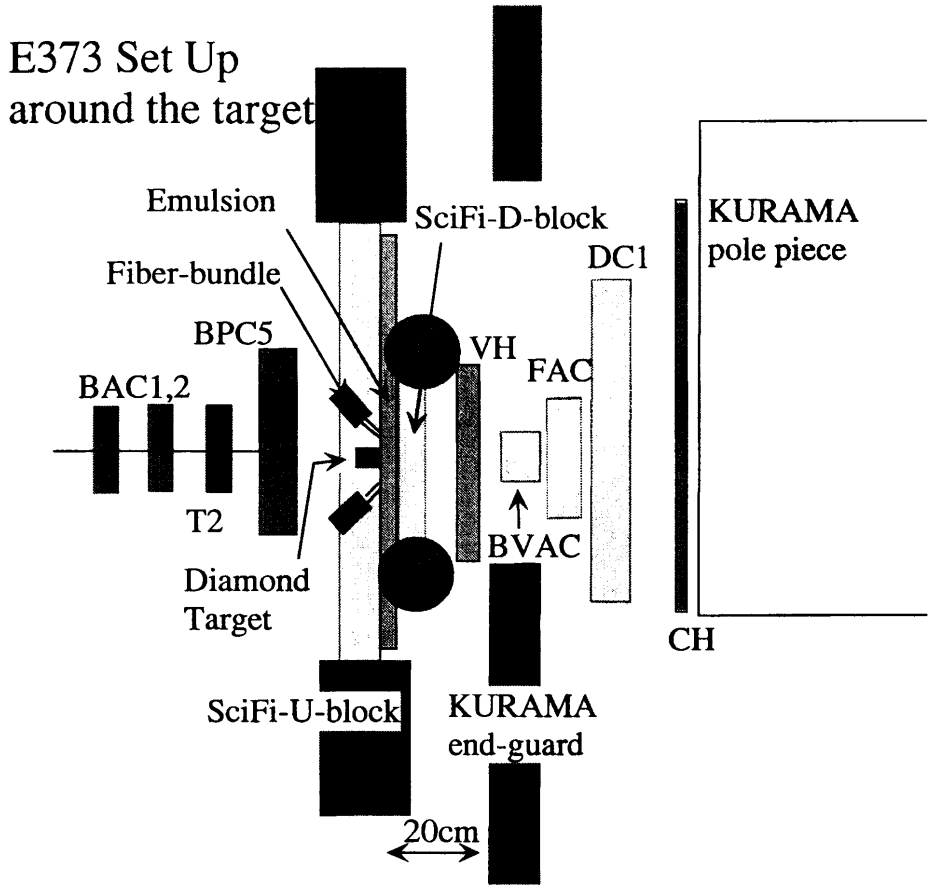

Figure 2.2: Schematic view of the experimental setup around the target region.

protons and π^-'s produced via the decay of hypernuclei can be detected with the range counter of scintillating mono-fiber blocks located both upstream and downstream of the emulsion stack. In addition, these scintillating fiber detectors have been used to select events in which the Ξ^- hyperons are likely to be stopped in the emulsion. Figure 2.5 shows a photograph around the target. This technique of using nuclear emulsion with other tracking detectors and counters is referred to as the 'hybrid-emulsion' method and is one of the most efficient and reliable ways to study short-lived particles.

To obtain 10 times larger statistics than the previous E176 experiment with the limited amount of emulsion, various ideas were introduced. In E176, the emulsion was used as both a (K^-, K^+) target and a Ξ^- absorber. The experiment E373 has used a diamond block as the (K^-, K^+) target. It is known that the forward angle cross section for the (K^-, K^+) quasi-free reaction is proportional to $A^{0.38}$[26] and that the absorption of the produced Ξ^- becomes larger for a larger mass number material. On the other hand, in order to bring the Ξ^- to rest effectively before it decays, the density of the material must be high. Diamond has the largest density among low mass number materials. By the use of a diamond block as the (K^-, K^+) reaction target, the thickness of the one emulsion stack

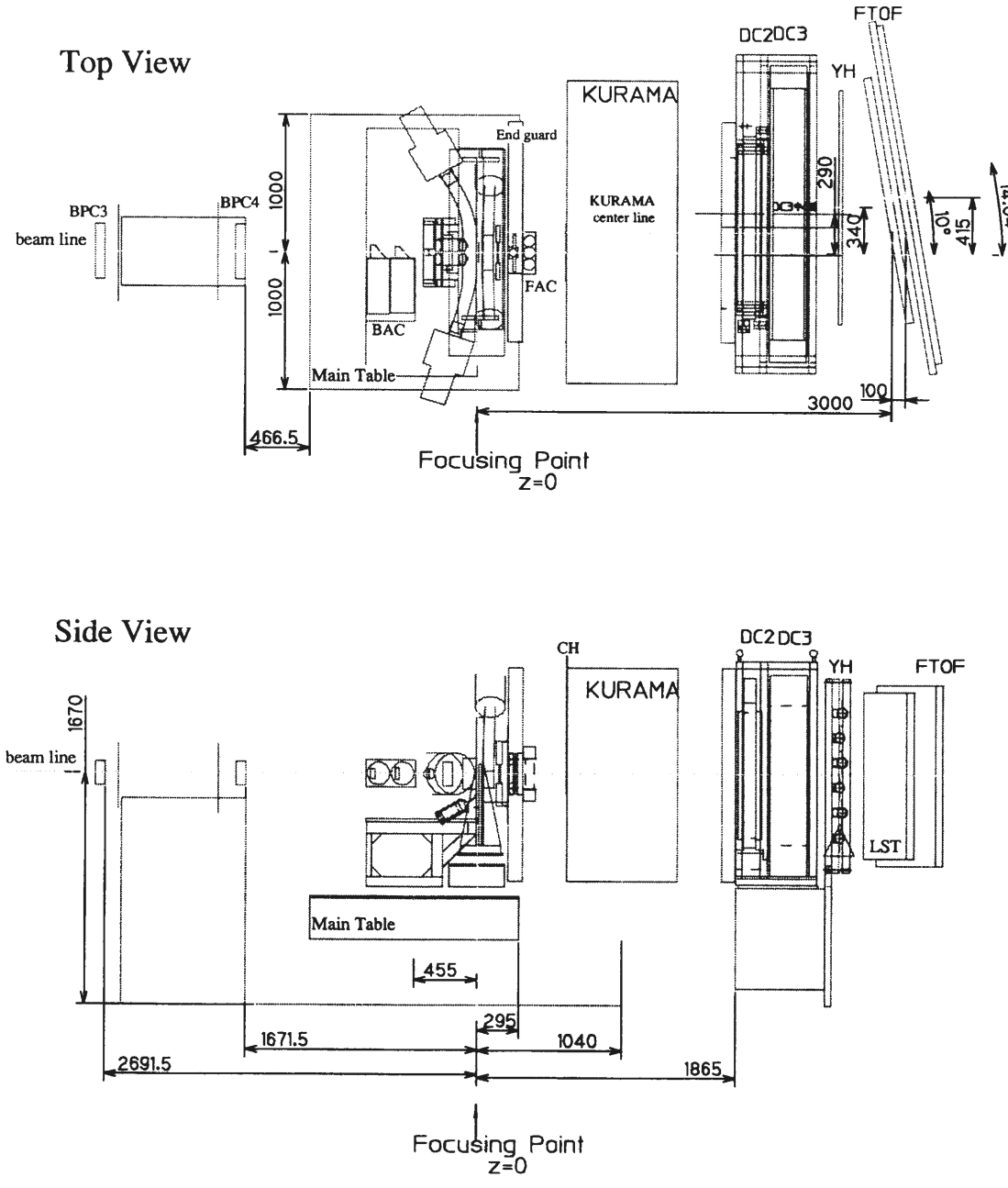

Figure 2.3: Plan view of the experimental setup.

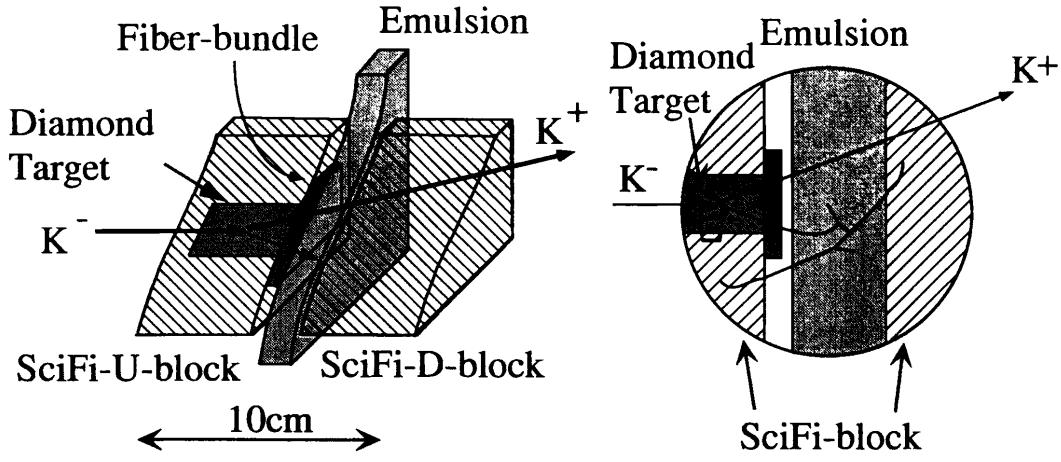

Figure 2.4: Schematic view around the target region.

was reduced to 1/5 of that of E176 and the total amount of the emulsion used in this experiment was only twice as much as that of E176. In the E176 experiment, the tracks of the outgoing K^+'s were searched for and traced to the reaction vertices in the emulsion. By directly searching and tracing the tracks of Ξ^-'s from the first, the time required for the emulsion scanning was reduced in this experiment.

Since the irradiatable track density in the emulsion is limited in order to secure the transparency of the emulsion plate after the development, the final yield would be reduced by the contamination of other particles, mainly π^-'s in the K^- beam. The high voltage of the electrostatic mass separator in the beam-line was set as high as possible, and a collimator was installed to kill the beam halo. Although the cross section of the (K^-, K^+) reaction is maximum at 1.8 GeV/c[27], the K/π ratio becomes worse at higher momentum. We had, therefore, decided to run at 1.66 GeV/c.

The detection of the K^+'s in the production angle close to 0 degree is very important, since the momentum transfer from the incident K^- to the Ξ^- becomes small. An aerogel Čerenkov detector was installed between the emulsion stack and the spectrometer magnet to veto only non-interacted K^-'s. We have obtained a very large acceptance (0.17 sr) including the zero degree.

2.2 K^- beam

2.2.1 K2 beamline

A 1.66GeV/c K^- beam from the K2 beam-line was used to induce the (K^-, K^+) reaction. The K^-'s were produced by protons from KEK-PS on a production target. These protons were accelerated to 12GeV in about 2 seconds. Then they were extracted from PS and transported to the primary production

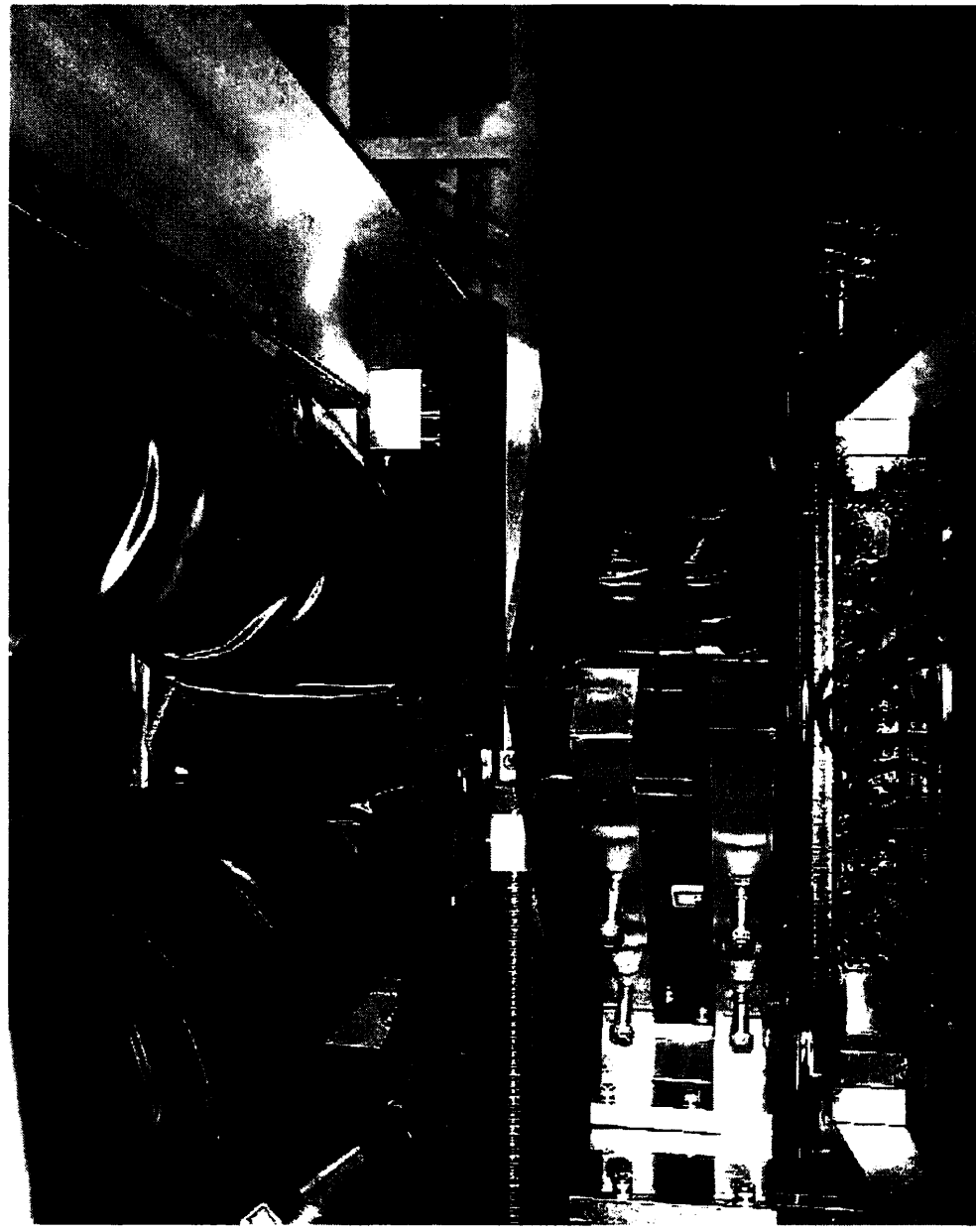

Figure 2.5: Photograph of the target region seen from the side. The beam entered from the left side of the picture. The two black blocks are scintillating fiber block detectors.

target of the K2 beam-line during about 2 seconds. The extraction period is called "spill".

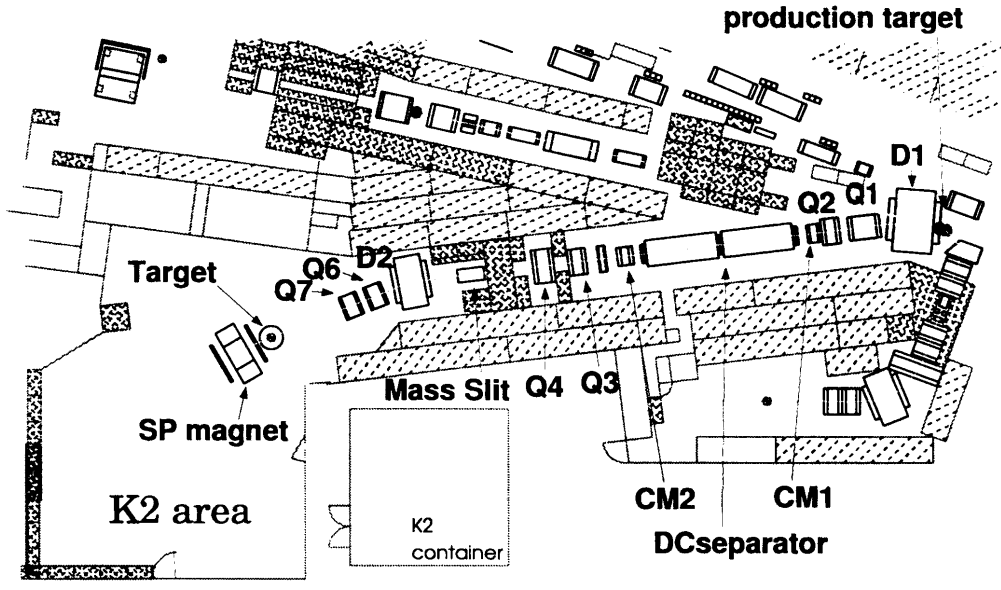

Figure 2.6: Plan view of the K2 beam-line.

Figure 2.6 shows a plan view of the K2 beam-line. The beam-line was designed to extract an enriched kaon beam with momenta from 1 GeV/c to 2 GeV/c[28]. In Table 2.1, the specifications of the K2 beam-line are listed. It consists of two dipole magnets (D1 and D2), six quadrupole magnets (Q1,Q2,Q3,Q4,Q5,Q6 and Q7), a pair of correction magnets (CM), and an electrostatic mass separator (SEP).

Table 2.1: Specifications of the K2 beam-line.

production angle	0 degree
solid angle acceptance	$\pm$50 mrad.(H)$\times\pm$6.5 mrad.(V)
momentum bite	3.6%
length	25.8m

The production target was made of a platinum rod of 6mm width, 3mm thickness and 60mm length. The secondary particle beam, consisting of K^-'s, π^-'s and $\bar{p}$'s is transported to SEP. The length of SEP is 6m and the distance between the electrodes is 10cm. A potential of 630 kV was applied across the positive and negative electrodes. It was filled with a mixed gas of Ne-He (33% He) with a pressure of about 3×10^{-4} torr in order to prevent electric discharges. The

particles are deflected according to their masses in SEP. Then the beam is focused vertically by the quadrupole doublet Q3-Q4 with a vertical magnification factor of about 0.8 at the position where the vertical slit (mass-slit) is placed. Considering the production target size and the magnification factor, the gap of the mass-slit was set to 2.7mm. The correction magnet CM was tuned to maximize the K/π ratio of the beam.

Finally, the beam was focused at the (K^-, K^+) reaction target by using a pair of quadrupole magnets (Q6 and Q7). The beam size on the target was 4.7mm (r.m.s.) in horizontal and 5.4mm (r.m.s.) in vertical. A portion of the π^--beam passes through the mass-slit and makes a bigger profile at the target. To reduce such a halo, a collimator made of tungsten-alloy blocks was placed just downstream of Q7. The shape of the collimator gap was trapezoidal in the horizontal plane to fit the profile of the K^--beam as shown in Fig.2.7. The thickness of the tungsten-alloy blocks was larger than 30mm, and those blocks were surrounded by iron blocks.

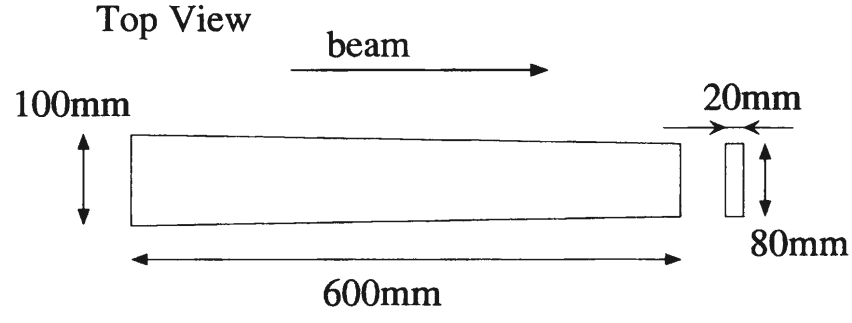

Figure 2.7: Shape of the collimator gap

Typical K^-/(all-charged-particle) ratio of the beam was 25%. Typical intensity of the K^--beam was 1.1×10^4/spill with 2×10^{12} primary protons during the beam-time in '98.

2.2.2 Particle identification

The identification of the incident particles was performed with TOF counters (T1, T2), and two aerogel Čerenkov counters (BAC1, BAC2).

T1 and T2 were made of plastic scintillators (Bicron BC418) of 5mm thickness and 5cm height. Their widths were 10cm and 5cm, respectively. Each of them was viewed by two sets of photo-multipliers (PMT), HAMAMATSU H2431-50, from both horizontal ends. The distance between T1 and T2 was 674 cm. They were used to get the time-of-flight (TOF) information of the incident particles. The TOF resolution was 75 psec(r.m.s.) after the correction of timing fluctuations due to the pulse-height difference in the discriminators using ADC information.

Each of BAC1 and BAC2 contained a hydrophobic-silica-aerogel block[29]. Figure 2.8 shows a schematic drawing of BAC's. The size of the block was 10cm

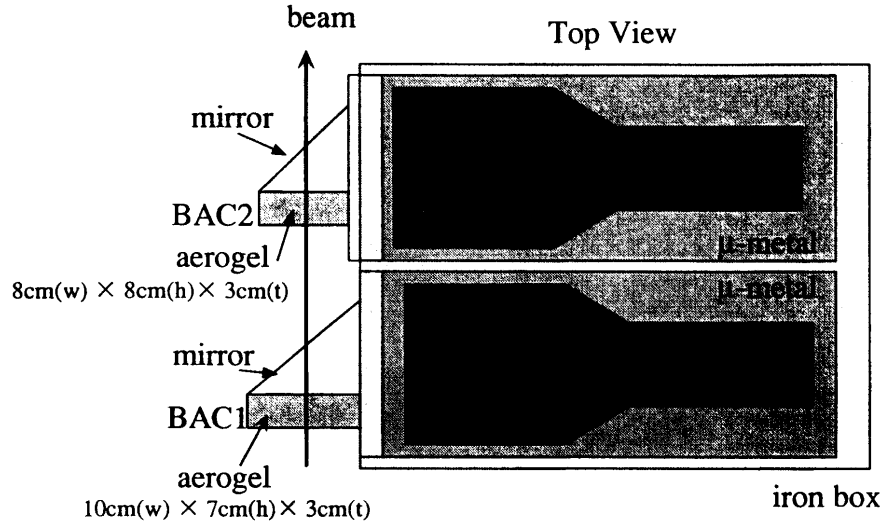

Figure 2.8: Top view drawing of BAC1 and BAC2.

wide, 7cm high and 3cm thick for BAC1, and 8cm wide, 8cm high and 3cm thick for BAC2. They were used to distinguish π^-'s, μ^-'s and e^-'s from K^-'s in the incident beam. The refractive index of the aerogel blocks was 1.03, which corresponds to the Čerenkov-radiation β-threshold of 0.971. At 1.66 GeV/c, the β is 0.997 for π^- and 0.959 for K^-. So Čerenkov light was emitted by the passage of π^-, μ^- or e^- only, reflected by the mirror made of an aluminized-mylar film, and detected by a 5inch$^\phi$ PMT, Hamamatsu R1584 which has a UV transparent glass as input window, for each of BACs. To shield against the fringing field of the spectrometer magnet, the PMTs were put into an iron box after each was doubly covered by μ-metal pipes. The outer μ-metal pipes were extended by 2cm and 1cm from the cathode surface for BAC1 and BAC2, respectively. The iron box were extended by 2cm from the outer μ-metal pipes.

The performance of BACs was studied with 1.66 GeV/c K^+ and π^+ beams. In Fig.2.9, ADC spectra for BACs are shown. Their efficiencies are summarized in Table 2.2. These efficiencies were obtained with a threshold level below the one-photoelectron pulse height. BACs were used to make a veto for the online 1st level trigger. Due to the knock-on electrons generated with the beam, each had about a 5 % efficiency for the K-beam. By requiring a coincidence of two BACs for the veto, the over-killing of the K-beam was reduced to 0.52% while keeping the rejection efficiency of 99.8% for the π-beam.

For the monitoring of the beam profile and the tracking of the incident angle, five multi-wire proportional chambers (BPC1-5) were used. Their specifications are summarized in Table 2.3.

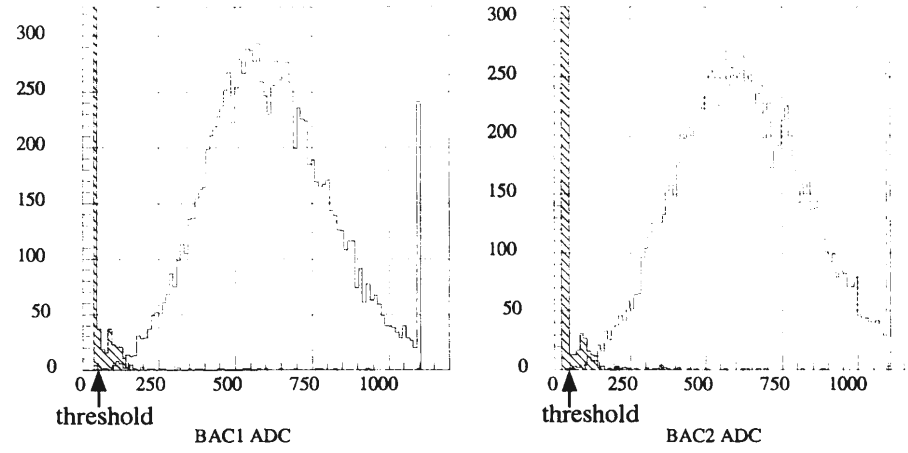

Figure 2.9: ADC spectra of BACs. White areas correspond to those for π^+ and hatched areas correspond to those for K^+.

Table 2.2: Efficiency of BACs. The threshold level was set below the one-photoelectron pulse height.

	efficiency for K	efficiency for π
BAC1	5.4%	99.81%
BAC2	4.9%	99.98%
total	0.52%	99.8%

2.3 Target

A diamond block was adopted as the target to produce Ξ^-'s via the (K^-, K^+) reaction. It was composed of $1\times1\times0.1$ cm^3 wafers of industrial diamonds, made by a chemical-vapor-deposition process, stacked and epoxied together[30]. The total dimension was 20mm square and 30mm thick with a density of 3.34 g/cm^3. Figure 2.10 shows a picture of the target.

2.4 K^+ tagging spectrometer

The outgoing K^+'s from the (K^-, K^+) reactions were identified with the momentum and velocity information obtained with the spectrometer system. The forward angle cross section for the (K^-, K^+) reaction is about $37\times A^{0.38}\mu$b[26]. Here A denotes the atomic number of the target nucleus. This is much smaller than those for the (K^-, K^-), (K^-, p) or $(K^-, \pi^\pm)$ reactions. The spectrometer system was designed to get a large acceptance while keeping sufficient resolutions for the momentum and velocity to distinguish K^+'s from K^-'s, p's or $\pi^\pm$'s. Some of the detectors were installed inside the spectrometer magnet to shorten the

Table 2.3: Specifications of BPC's

anode-wire spacing	1 mm
anode-wire diameter	10 μm
anode-wire material	Au-plated W
operation voltage	4 kV
gas mixture	Ar 73%,Iso-C_4H_{10} 24%,Freon 0.5%,Methylal 3%
active area	
BPC1	112 mm (X)
BPC2	112 mm (X)
BPC3	112 mm (X) $\times$ 64 mm (Y)
BPC4	112 mm (X) $\times$ 64 mm (Y)
BPC5	80 mm (X) $\times$ 64 mm (Y)

distance from the target to the magnet. The distance from the target to the forward TOF hodoscope (FTOF) was decided to be 3.1m by considering the TOF resolution and K^+'s decay rate.

The online 1st-level trigger distinguished K^+'s from $\pi^\pm$'s and K^-'s with aerogel Čerenkov detectors and scintillator hodoscopes. By the 2nd-level trigger, the TDC information was also used to distinguish K^+'s from protons.

At the offline analysis, the momentum of the outgoing particle was calculated from the bending angle of the track in the spectrometer magnet. The velocity was determined using the TOF information and the path length. The K^+ was identified by the mass calculated from the momentum and the velocity.

2.4.1 Spectrometer magnet and acceptance

A window-frame-type dipole magnet "KURAMA" was used as the spectrometer magnet. It has a 50 cm gap, 100 cm aperture and 80 cm long pole piece. End-guard plates of 10 cm thickness were installed both upstream and downstream of the magnet. Originally, the size of the plates was 160 cm wide and 154 cm high, but to reduce the fringing field of the magnet which would cause the distortion of IITs, additional plates were added to the front end-guard so that it covers an area of 190 cm width and 169 cm height. The downstream one has a 60 cm high and 110 cm wide window, while the front one has a 30 cm high and 30 cm wide window.

The magnet center was located 1040 cm and 15 cm from the target point along and perpendicular to the beam direction, respectively. The distance from the target to the front end guard was 22 cm. The field direction was vertical and the strength at the center was about 1 Tesla.

Detectors were designed and installed to measure all the K^+'s passing through KURAMA having a momentum from 1.0 GeV/c to 1.4 GeV/c. So the geomet-

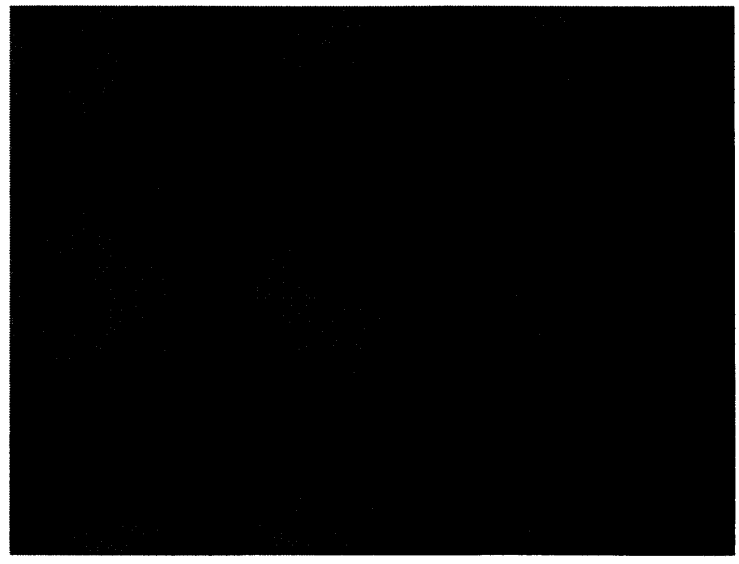

Figure 2.10: Picture of the diamond target.

rical acceptance of the spectrometer system was determined by the aperture of KURAMA. It was calculated to be 0.17 sr for the above momentum region by a MC simulation.

2.4.2 Aerogel Čerenkov counters

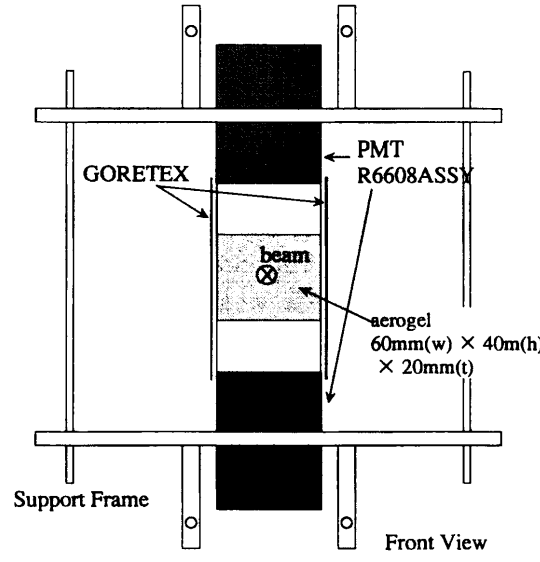

Figure 2.11: Drawing of BVAC

Two aerogel Čerenkov counters, BVAC and FAC, were used to identify the outgoing K^+ at the online trigger level. Like BACs, each of them also contained a hydrophobic-silica-aerogel block.

BVAC worked as a veto for non-interacted K^-'s. Although the 1st-level trigger can distinguish the charge of the outgoing particle as described in Sec.2.7, some of the non-interacted K^-'s decay in the spectrometer magnet and misidentified as a plus charge particle. Therefore, the veto was necessary to reduce the trigger rate. The aerogel block had a refractive index of 1.05, which corresponds to the Čerenkov β-threshold of 0.952. Kaon has β's of 0.959 and 0.943 at the momentum of 1.66 GeV/c and 1.4 GeV/c, respectively. So, BVAC should be efficient for the non-interacted K^-'s and inefficient for the scattered K^+ in the momentum region of our interest. This enabled us to accept very-forward-scattered K^+'s, for which low-momentum Ξ^-'s are expected to be associated with a high probability.

Figure 2.11 shows a schematic drawing of BVAC. The size of the aerogel block was 60mm(W)×40mm(H)×20mm(T). It was installed at the aperture of the front end-guard of KURAMA, just covering the beam profile. To be operated in the strong magnetic field, fine-mesh type PMTs, Hamamatsu R6608ASSY, which have 2-inch$^\phi$ UV-transparent input windows, viewed the block from both top and bottom sides. Not to cut off the acceptance of the spectrometer, the PMTs were attached across some distances from the aerogel block. The space between two PMTs including the aerogel block were covered by a highly-diffusing white sheet, "GORETEX".

The performance of BVAC was studied with K^- and K^+ beams. The efficiency is 97% at 1.66 GeV/c and 13% at 1.2 GeV/c.

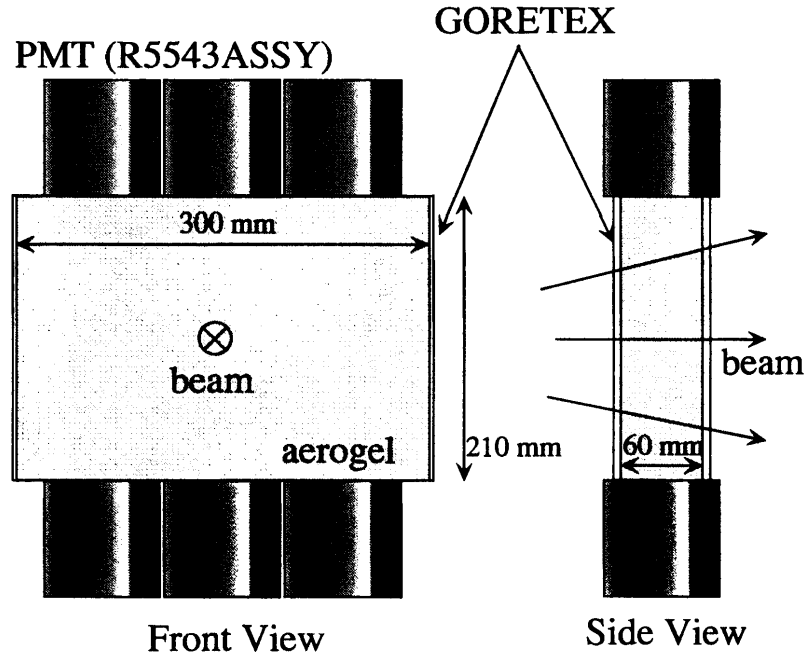

Figure 2.12: Schematic drawing of FAC.

FAC was installed for the separation of outgoing K^+'s from π^+'s. Figures 2.12 and 2.13 shows a schematic drawing and picture of FAC. The dimension of

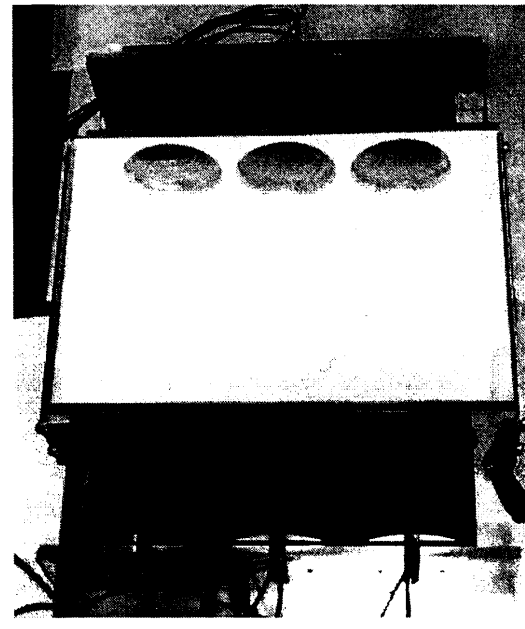

Figure 2.13: Picture of FAC.

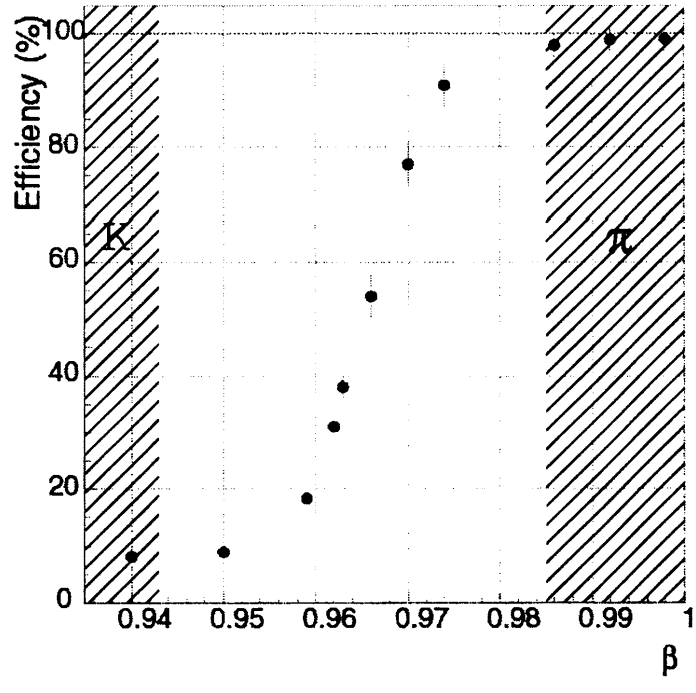

Figure 2.14: FAC efficiencies at various β's. The two hatched areas correspond to β region for the kaon's and the pion's, respectively.

Table 2.4: Characteristics of the spectrometer drift chambers. (Here, "X" and "Y" corresponds to the horizontal and the vertical direction, respectively.)

chamber	DC1	DC2	DC3
plane	XX'YU	XX'YY'	XX'YY'
sense-wire spacing	10 mm	9 mm	XX':56 mm YY':60 mm
sense-wire diameter	20 μm		
sense-wire H.V (kV)	-	-	+1.00
sense-wire material	Au-plated W		
potential-wire diameter	75 μm	200 μm	150 μm
potential-wire H.V	-1.75 kV	-2.10 kV	-3.00 kV
potential-wire material	Au-plated Cu-Be	Al	Au-plated Cu-Be
number of channels	XX':48 Y:32 U:48	XX':128 YY':96	XX':32 YY':16
active area (X×Ymm^2)	500×350	1200×1200	1800×900
gas mixture	Ar 50%:C_2H_6 50%		
resolution (r.m.s.)(μm)	100	160	250

the aerogel block was
300mm(W)×210mm(H)×60mm(T). The block was covered by a "GORETEX" sheet and was viewed by six PMTs from the top and bottom ends. It was installed between the front end-guard and the pole-piece of KURAMA. Fine-mesh type 3-inch PMTs, HAMAMATSU R5543ASSY, were used. The refractive index of the aerogel block was 1.041, corresponding to the Čerenkov β-threshold of 0.962. The performance was studied with the beam of π^+, K^+ and p at various momenta. The obtained efficiencies are plotted against β in Fig.2.14. For the momentum region from 0.8 GeV/c to 1.4 GeV/c, the rejection efficiency for pions was higher than 98%, and those for kaons was about 8%. Position dependence of the sensitivity was found to be negligible.

2.4.3 Scintillator hodoscopes and wire chambers for the trigger and tracking.

Tracks of outgoing particles were measured with four plastic-scintillator hodoscopes (VH, CH, YH and FTOF), three drift chambers (DC1, DC2 and DC3) and a limited-streamer chamber(LST). The hodoscopes were used also to make a data-taking trigger.

Characteristics of the drift chambers are summarized in Table 2.4. As shown in Fig.2.1, DC1 was installed between the front end-guard and the pole piece of KURAMA, just downstream of FAC. DC2 and DC3 were installed downstream

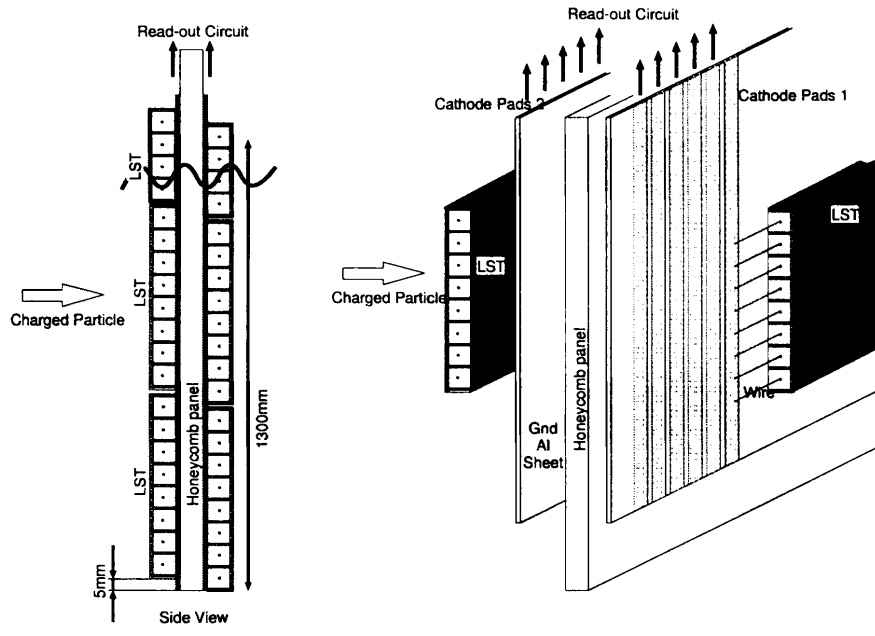

Figure 2.15: LST schematic view.

Table 2.5: Specifications of LST

effective area	$2000mm(W)\times 1200\text{mm(H)}$
anode-wire diameter	$100\mu m$
anode-wire H.V	4.95 kV
cell size	10 mm
tube width	84 mm
tube length	2500 m
gas mixture	Ar 23%,Iso-C_4H_{10} 77%
strip width	4 mm
strip spacing	6 mm
r.m.s resolution	4.5 mm

of KURAMA. More details about these drift chambers are described in Ref.[31].

LST was composed of two layers of plastic limited-streamer tubes of the Iarocci type as shown in Fig.2.15. Each tube has 8 square cells. One cell has one anode wire surrounded by a resistive graphite coating on the inner surface that serves as the cathode except for the one side out of the four sides. On the open side, the cathode strips made of PVC and aluminum sheets were attached perpendicularly to the anode wire. The induced pulses on the cathode strips were discriminated to get the position information with the accuracy of the strip spacing. As shown in Fig.2.1, LST was installed most downstream to measure the position in the horizontal direction. Table 2.5 summarizes the specifications of LST. More details

Table 2.6: Specifications of the scintillator hodoscopes. (Here, "X" and "Y" mean the horizontal and the vertical direction, respectively.)

	VH	CH	YH	FTOF
direction of the array	X and Y	X	Y	X
number of channels	X:32 Y:18	24	6	24
thickness(mm)	2	2	5	30
width(mm)	X:6.6 Y:9.0	19	200	80
spacing(mm)	X:4.4 Y:6.0	17.5	180	75
PMT Type No. (HAMAMATSU)	X:R5600U[1] Y:R3164-10	H3165-01	H1161	H1949
scintillator Type No.	SCSN-50	SCSN-50	SCSN-56	SCSN-56
diameter of PMT(mm)	X:10 Y:10	13	50	50
effective area(mm×mm)	143×110	421.5×300	1700×1100	1805×1200
note	All scintillators were coupled via lucite light-guides to PMTs.			

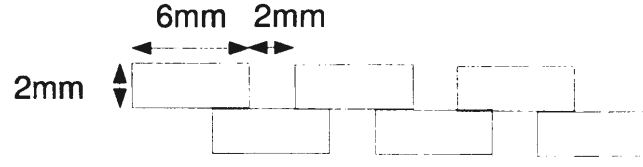

Figure 2.16: Schematic top view of the VH scintillator array.

are described in Ref.[32].

The scintillator hodoscopes were used for the tracking and/or the data-taking trigger. Table 2.6 summarizes the specifications for those.

VH(Vertex Hodoscope) has two planes of an array of plastic scintillators to measure the position of the track in the horizontal and vertical directions. The scintillator rods were staggered as shown in Fig.2.16, so that the detector has a position accuracy of 1/3 of the width of each rod. It was installed just upstream of the front end-guard of KURAMA. For the shielding against the magnetic field, each of the readout PMTs was covered by a μ-metal pipe, and iron plates sandwiched the whole detector except the detection area. It worked not only for the tracking, but also to make the trigger. By requiring charged particle hits on VH, some of the neutral particles like K_s which can decay into charged particles inside KURAMA can be rejected at the online trigger level.

CH and YH were used to make the trigger, which will be described in Sec.2.7.

[1]metal package PMT

CH was installed just in front of the pole-piece of KURAMA. The lucite light-guides were extended through the narrow gap between the coil and the pole-piece to the top of KURAMA, and connected to PMTs there. YH was installed downstream of KURAMA.

FTOF (Forward TOF hodoscope) measured time-of-flight of the outgoing particles together with T2. The plastic scintillator rods were installed vertically at a distance of 3.1 m from the target. Each scintillator rod was viewed by PMTs from the top and the bottom. The 12-bit TDCs, REPIC HR-TDC, were used to measure the timing. They have a time resolution of about 27.5 psec/count, which was precisely determined by calibration measurements with a TDC-calibrator, REPIC TDC-TESTER. At the offline analysis, the fluctuations of timing due to the pulse-height differences in the discriminators were corrected with functions inversely proportional to the 1/4th power of the pulse-height obtained with ADC modules. The offset values to get the absolute time-of-flight from the TDC data were determined from the analysis of (π^-, π^+) calibration runs. The average r.m.s resolution of time-of-flight from T2 to FTOF was 120 ps.

Also, the vertical hit position on FTOF was obtained from the time difference between the two signals from the top and bottom PMTs. The r.m.s resolution for that was 18 mm.

2.5 Scintillating-fiber detectors

Two kinds of scintillating-fiber detectors were constructed. One is a scintillating-microfiber bundle detector (Fiber-bundle) to measure the position and angle of the Ξ^- track. The other is a scintillating-fiber block detector (SciFi-block) to measure the ranges of particles emitted from the decay of hypernuclei. Two blocks were installed.

Fiber-bundle and SciFi-blocks were also used to select the events of interest among those tagged as the (K^-, K^+) reaction.

These detectors were viewed by the chains of three or four image intensifier tubes (IIT) (Fig.2.17). They amplify lights from fibers with 2-dimensional information. We adopted an electrostatically focusing type as the 1st stage of the chains because of their higher quantum efficiencies and higher rate capability. The last two stages were gatable micro-channel-plate (MCP) type. Phosphor on the IIT's anode holds images during the decay time of phosphorescence and can work as an "optical delay" of the image. Only the images of interest can be selected by gating the next stage IIT using trigger pulses from the counter system. In the E373 experiment, the MCP type IIT's were gated by the first or second level trigger.

Each of the output windows of the last stage IITs was connected to the charge coupled device (CCD), SONY XC-77RR, via a tapered optical fiber plate.

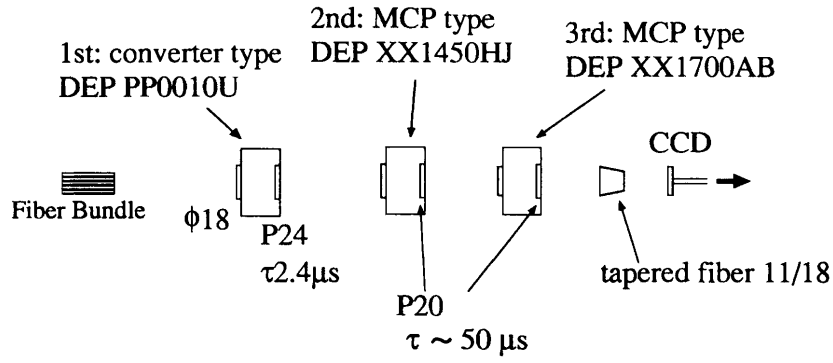

(a) Fiber-Bundle IIT System

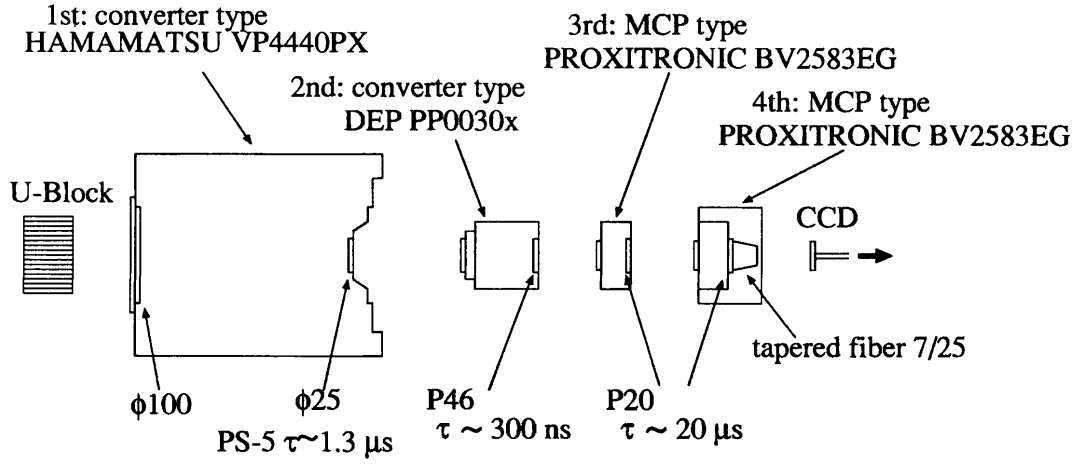

(b) U-Block IIT System

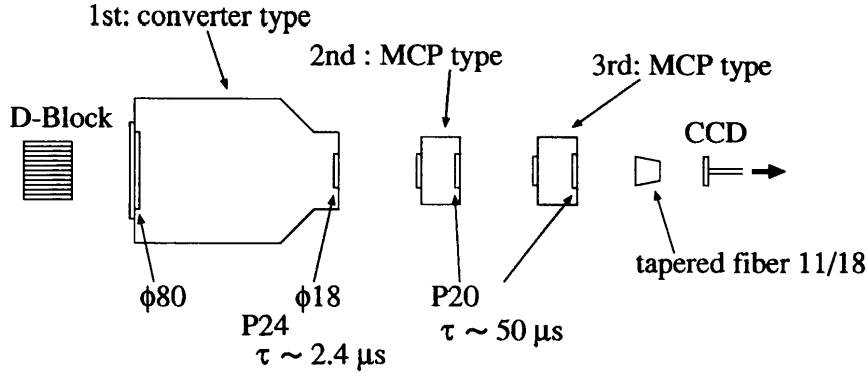

(c) D-Block IIT System : DEP PP0040C

CCD : Sony XC-77RR

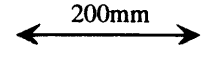

Figure 2.17: Schematic drawing of the structure of IIT chains for Fiber-bundle (a), U-Block (b) and D-Block (c).

The CCD consists of 768 × 493 pixels, where the dimension of each pixel is $11\mu m \times 13\mu m$.

2.5.1 Scintillating-microfiber bundle detector for the Ξ^- tracking

The position and angle of the Ξ^- track was measured by a scintillating-microfiber bundle detector. It was installed in the narrow gap between the diamond target and the emulsion stack. Due to the short lifetime of the Ξ^- hyperon, a very thin and high resolution tracking detector was required. A scintillating microfiber-bundle (fiber-bundle) is a coherent fused bundle of very thin (tens of micro meters) scintillating fibers. As scintillating fiber detectors of high pre-

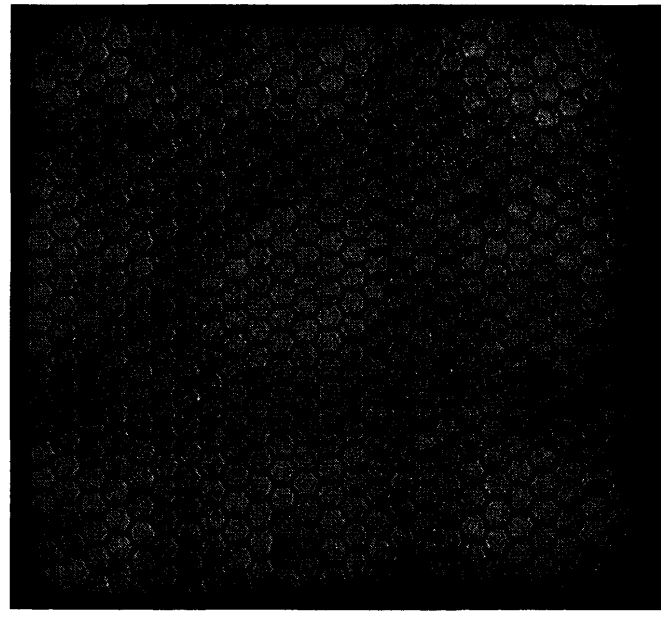

Figure 2.18: End view of a 1mm-square fiber-bundle. The diameter of one fiber is $30\mu m$.

cision, three kinds of microfiber-bundles are known : scintillating glass fibers, liquid scintillator in glass capillaries and plastic scintillating fibers. We adopted a plastic scintillating fiber[33, 34, 35, 36, 37, 38, 39] because it is easy to handle and has rather high light yield. Figure 2.18 shows an end view of a 1mm-square fiber bundle. The core is made of polystyrene doped with PMP (1-phenyl-3-mesityl-2-pyrazoline) as a wavelength shifter with a large stokes shift[40, 41]. It is surrounded by two claddings, an inner layer of normal PMMA (polymethyl methacrylate), and an outer layer of fluorinated poly-methacrylate with a refractive index of 1.42[42]. The diameter of a fiber and the density of the wavelength shifter were optimized to obtain a large light yield and a small track residual by measuring the light yield and the attenuation length. Details of the measurement and study of the performance as a tracking detector are described in Ref.[43]. We

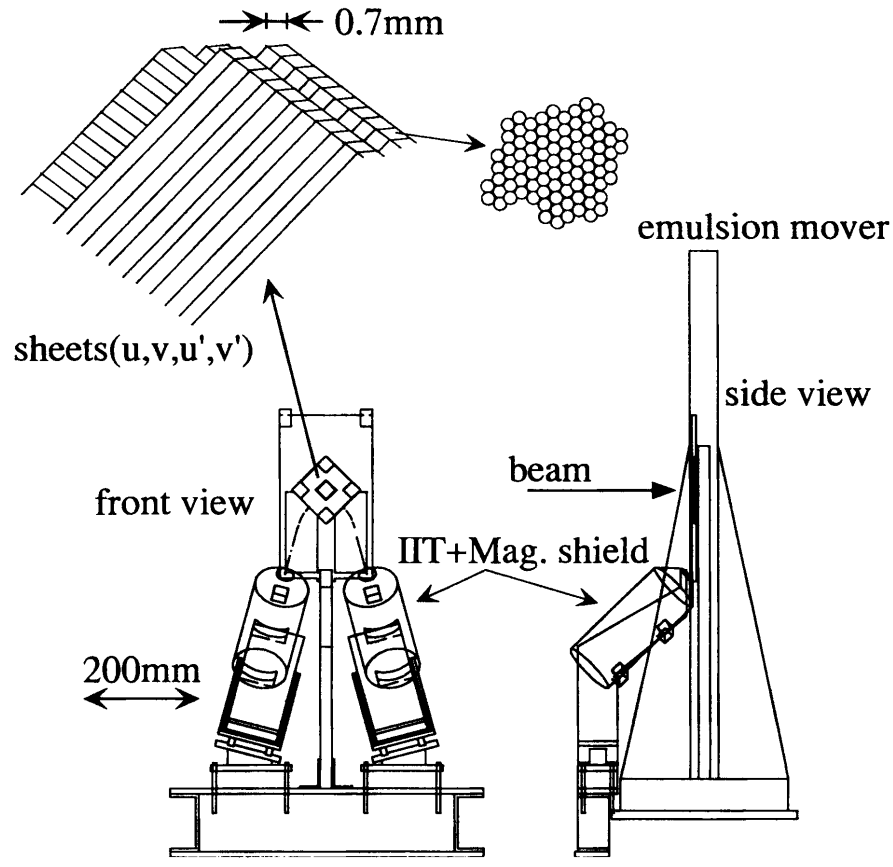

Figure 2.19: Schematic drawing of the Fiber-bundle detector.

adopted 0.7 mm square bundles made of 45 μm^{ϕ} fibers [2]. The density of PMP was 2.0 wt%.

Figure 2.19 presents a schematic view of the Fiber-bundle detector. Each sheet was made of sixty fiber bundles by bonding them with black acrylic water paint. Four sheets were stacked as a u,v,u' or v' sheet. Here, the u and v directions are perpendicular to the beam direction. The sheets were fixed with adhesive double coated tapes. The total thickness of the detector was 3.4 mm with adhesive double coated tapes and mylar sheets.

At the output edge, each sheet was divided into five pieces and piled so that all sheets could be viewed from the input window($18mm^{\phi}$) of two IIT chains (one for the u direction sheets and the other for the v direction sheets). The average length of the fiber bundles was about 23 cm.

Each IIT chain for this detector consisted of three image intensifier tubes, DEP-PP0010U, DEP-XX1450HJ, and DEP-XX1700AB and one CCD chip (Fig.2.17(a)). The first stage of the IIT chain is an electrostatically focusing type with approximately no magnification. The second and third stages are both of a gatable

[2]In '00, 1 mm square bundles were used to obtain better angular resolution

micro-channel-plate type. The output part of the 3rd stage IIT is connected to the CCD via a tapered optical fiber plate. The magnification of this tapered fiber plate is 11/18. The phosphors of the 1st, 2nd and 3rd IIT are P24, P20 and P20, respectively. The mean decay times of P24 and P20 are 2.4 μs and 50 μs, respectively. The photo-cathodes are bialkali, S20 and S20 respectively. The resolution of the IIT-CCD system was measured by illuminating a 10μm slit positioned at the input window of the IIT with an LED[43]. The two track resolution of the IIT-CCD system is 33μm(r.m.s), and the position accuracy for a photoelectron is 9.3μm(r.m.s).

The precision of track connection from Fiber-bundle to the emulsion in the '98 run is described in Appendix A.

2.5.2 Scintillating-fiber block detectors

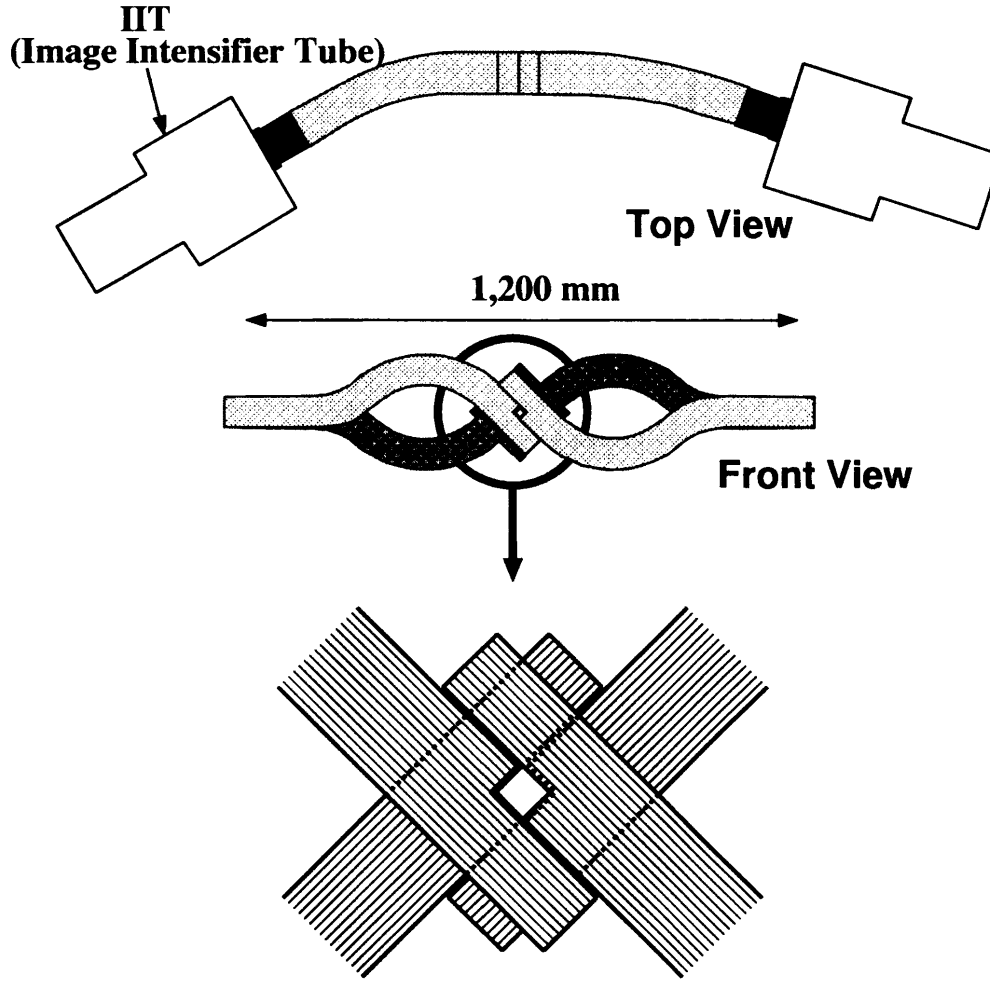

Figure 2.20: Schematic view of the Upstream SciFi-block.

Figure 2.21: Photograph of the Upstream SciFi-block. The white square block at the center is the diamond target.

Scintillating fiber block detectors were installed just upstream and downstream of the emulsion stack as shown in Figs.2.4 and 2.5. Their main purpose is to measure the range and hence the energy of high momentum π^-'s and protons which are produced via the decays of hypernuclei in the emulsion and leave the emulsion. The second purpose is to detect the decay of Λ or the H-dibaryon emitted from the Ξ^- stopping points. In addition, they are used to select the events for the emulsion scanning. For example, the event in which the Ξ^- hyperon had decayed before stopping in the emulsion is rejected by the human eye scanning.

The schematic view of the upstream block (U-Block) and downstream block (D-Block) were shown in Fig.2.20 and 2.22, and a photograph of U-block is shown in Fig.2.21. The blocks were made by stacking plastic scintillating fiber sheets. We adopted 0.5 mm $\times$ 0.5 mm square fibers, KURARAY SCSF-78. The core of the fiber is made of polystyrene having a refractive index of 1.59 and a density of 1.06 g/cm^3. It is surrounded by a 10 μm thick cladding made of PMMA (polymethylmethacrylate) having an index of 1.49 and a density of 1.18 g/cm^3. The concentration of the dyes in the fiber was determined to obtain large light yield. The sheets were stacked and packed with the accuracy within 0.2 mm. The number of fibers per one sheet is 144 for U-Block and 120 for D-Block. The

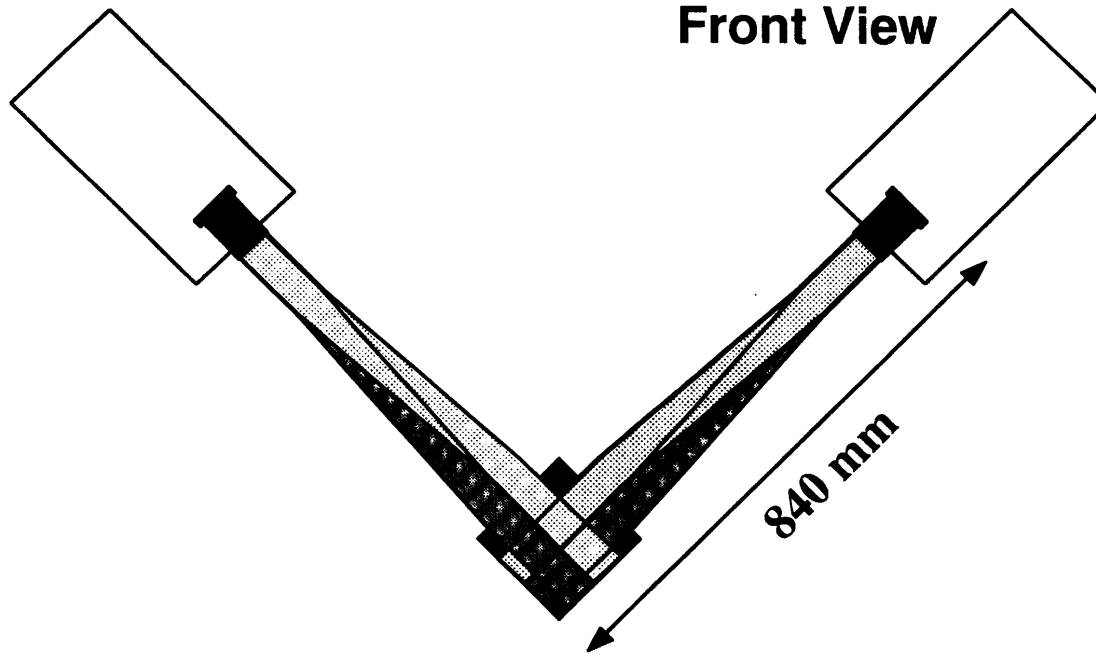

Figure 2.22: Schematic view of the Downstream SciFi-block.

U-Block consists of 98 fiber sheets and D-Block 90 fiber sheets.

As shown in Fig.2.20, there was a 20 mm × 20 mm square hole in the center of U-Block in order to insert the diamond target and to path the beam through. To make the hole without making unreadable dead spaces, each one sheet was divided into two partial sheets. One is extended to the left side IIT and the other to the right side IIT. The partial sheets from the u- and v-direction were piled up alternately at the input window of each IIT chain. Hence two images of uz- and vz-projection were read out by one IIT chain. It is, therefore, necessary to divide one obtained image to images corresponding the sheets and reconstruct the original two images. The one end of each sheet which is opposite of the readout-end was polished and evaporated with aluminum so that the photons are reflected by this end. Effect of this mirror was studied by measuring the yield of scintillation light induced by the passage of β-ray. It was found that the light yield was increased by 1.6 times by the mirror. In the readout-end of the fiber sheets, 0.3 mm thick black vinyl-chloride sheets were inserted between fiber sheets to make the separation easier. At the detection area, 0.3 mm thick aluminum plates were inserted as degraders between fiber sheets in order to increase the momentum acceptance of the block as a range counter. Each IIT chain of U-Block consisted of four image intensifier tubes and a CCD (Fig.2.17(b)). The input window of the first stage was 100 mm^{ϕ} in diameter. The first and second stages of the IIT chain were electrostatically focusing type. The third and fourth were MCP type. A tapered optical fiber plate with a magnification of 7/25 was inserted between the fourth stage and the CCD chip. Only the first stage had a magnification factor of 25/100, and the total magnification is 7/100. The phosphors of stages

Table 2.7: Thickness of the magnetic shield.

	iron (mm)	μ-metal
18^{ϕ} IIT-chain for Fiber-bundle	7	1
100^{ϕ} IIT-chain for U-block	30	2
80^{ϕ} IIT-chain for D-block	10	2

were PS-5, P46, P20 and P20, respectively.

The structure of D-Block is shown in Fig.2.22. In order to utilize the full aperture of the IIT, each sheet was divided to two partial sheets and they were piled up alternately at the input of each IIT. Like U-Block, black vinyl-chloride sheets of 0.2 mm thickness were inserted at the readout-end of fiber sheets, and Al degraders of 0.3 mm thickness were inserted at the detection area. Black acrylic plates evaporated with aluminum were attached as mirrors to the end of the block which is opposite to the readout-end. The IIT chain of D-Block consisted of three image intensifier tubes and a CCD (Fig.2.17(c)). The input window of the first stage was 80 mm^{ϕ}. The first stage of the IIT chain was an electrostatically focusing type with a magnification of 16/80. The second and third IITs were MCP type. A tapered optical fiber plate with a magnification of 11/18 was inserted between the third stage and the CCD. The total magnification was 11/90. The phosphors of the first, second and third stages are P24, P20 and P20, respectively.

The position resolution of the SciFi-block detectors was evaluated using tracks of minimum ionizing particles. The track residual and track separation are 290 μm and 350 μm for the U-Block, and 250 μm and 290 μm for the D-Block. As a range counter, the energy resolution was evaluated using stopping π^- and protons. The energy resolution was 0.86 MeV and 1.4 MeV for 38 MeV π^- and 47 MeV proton, respectively. Details about the performance are described in Refs.[44, 45].

2.5.3 Magnetic shield

The fringing magnetic field of KURAMA was 100 $\sim$ 200 Gauss around the target region. All the IIT's were covered by cylindrical magnetic shields to eliminate the distortion by the field. Figures 2.23 and 2.24 show schematic views of the magnetic shields for the 18^{ϕ} IIT chain and 100^{ϕ} IIT chain. Each shield consisted of two layers. The outer shield was made of iron (SS400) and the inner shield was made of μ-metal. The typical thicknesses of the shields are summarized in Table 2.7. The region around the input window of the chain was covered by a tapered cap.

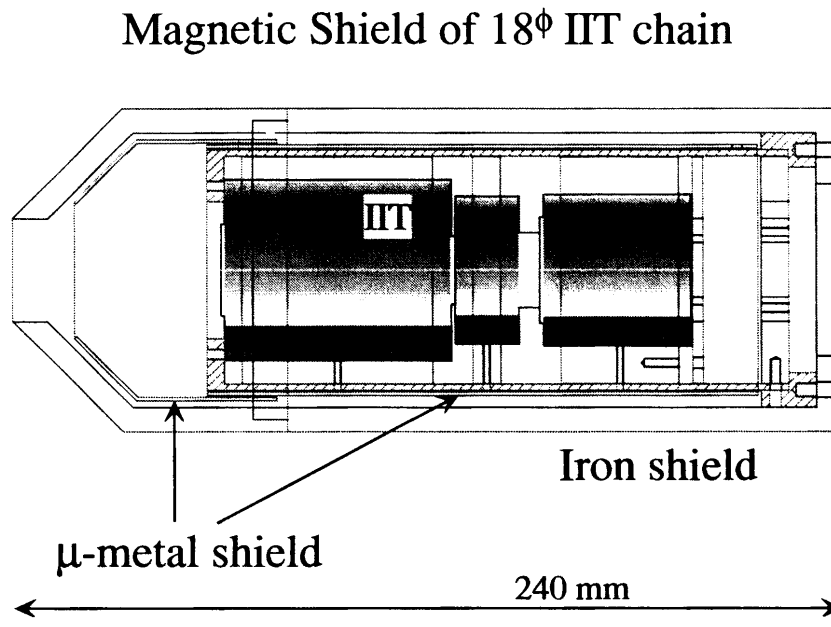

Figure 2.23: Schematic view of the Magnetic shield of the 18^{ϕ} IIT-chain.

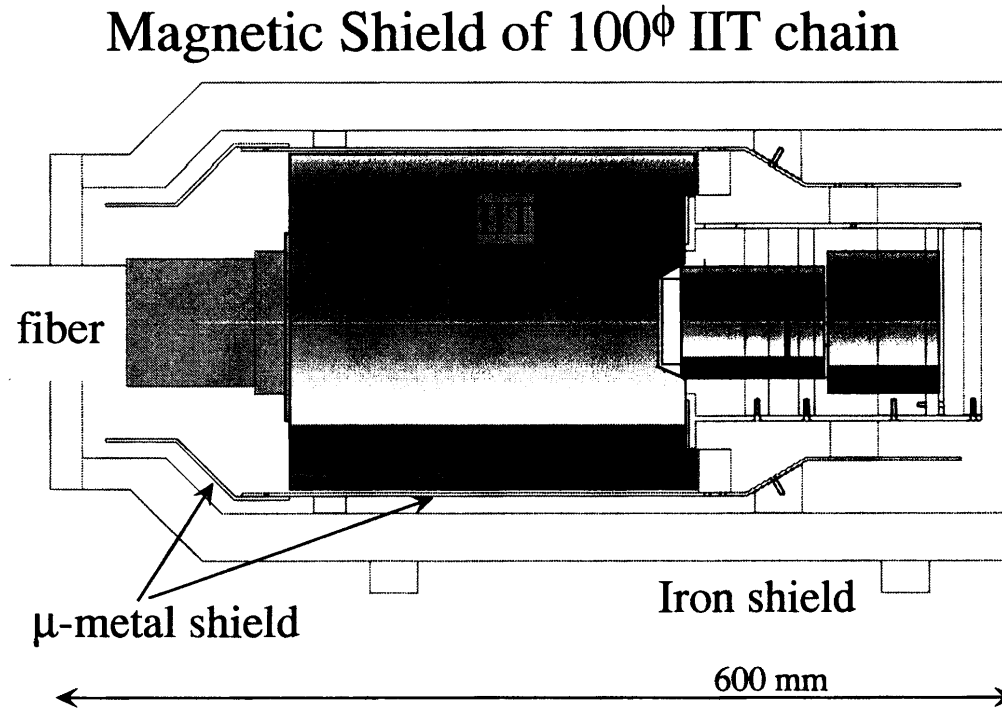

Figure 2.24: Schematic view of the Magnetic shield of the 100^{ϕ} IIT-chain.

2.6 Nuclear emulsion

Downstream the target, a stack of emulsion plates was placed perpendicular to the beam direction. One hundred stacks made of 69 l emulsion gel were irradiated. Each stack was composed of 12 emulsion plates of 250×245 mm^2 area. Each plate was made by coating Fuji ET-7C or ET-7D emulsion gel on both sides of an acrylic or polystyrene film base. The most upstream plate (thin-type plate) has 70 μm or 100 μm thick emulsion gel on both sides of a 200 μm base. Other plates (thick-type plates) have 500 μm thick gel on both sides of a 50 μm or 40 μm thick base. According to the position and angle of tracks predicted with Fiber-bundle, tracks were searched for in the most upstream thin-type plate. The thin-type plate was used as a "tracker" because the distortion generated during the development process is small. It would become difficult to search tracks if the distortion was large. The thick-type plates were used as Ξ^- absorber. The fabrication of the emulsion plates had been done at Gifu University[46]. The composition of the ET-7C/D emulsion gel is summarized in Table 2.8. The density of the emulsion was 3.60 g/cm^3 on average. The emulsion plates were

Table 2.8: The composition of the ET-7C/D emulsion

material	weight ratio(%)	mol ratio(%)
I	0.3	0.06
Ag	45.4	11.2
Br	33.4	11.1
S	0.2	0.2
O	6.8	11.3
N	3.1	5.9
C	9.3	20.6
H	1.5	40.0

stacked into a vacuum chamber cassette to keep the position and the flatness of the plates during the beam exposure. Figure 2.25 shows a picture of the cassette. The upstream part of the cassette was covered by a 150 μm thick stainless foil, while the downstream part was covered by a 1 mm thick black rubber plate. To obtain the uniform irradiation over the whole stack, the cassette was moved horizontally and vertically by an emulsion mover system between spills. The schematic drawing of the emulsion mover is shown in Fig.2.26. The gap between Fiber-bundle and the cassette was 1mm. To keep this distance for all stacks, the cassette was fixed to the movable stage of the emulsion mover by two pins under the bottom and one screw on the top. The emulsion mover was controlled by a personal computer (PC). Figure 2.27 shows an outline of the control system. A positioning board (HPC-PPD203) received the command from PC where the stage should be located and output pulses to a position feedback board (HPC-

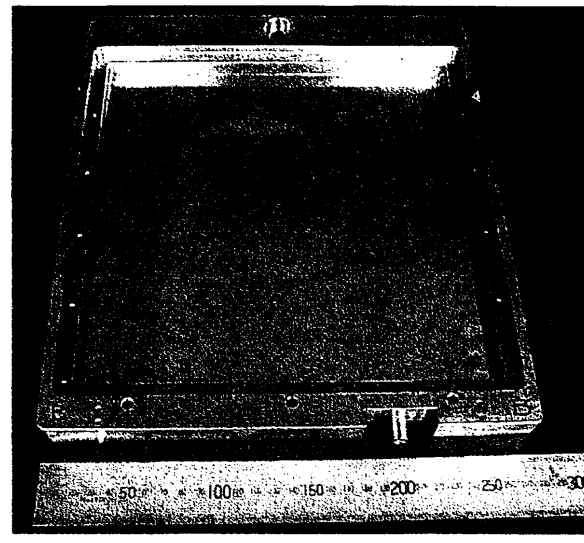

Figure 2.25: Photograph of the emulsion chamber cassette.

POS203). The position feedback board received the signals about the actual position of the stage from linear encoders in addition to the pulses from the positioning board and output analog pulses to servo-amplifiers according to the difference between the goal position and the actual position. The servo-amplifiers drived the DC motors.

At first, the cassette was moved in the horizontal direction by the distance proportional to the beam intensity in the previous spill. Typical distance of each movement was $\sim$2 mm, and typical exposure density was 1×10^6 particles/cm^2. When the cassette reaches the end in the horizontal direction, it was moved vertically by 2mm and then moved in the horizontal but opposite direction. The beam intensity for each spill was monitored by counting coincident signals from T1 and CH with a counter board on the PC. The position of the cassette was measured with linear encoders having a resolution less than 1 μm, and the data were sent by an I/O board to the data acquisition system of the experiment. Details about the emulsion mover is described in Ref.[47].

To obtain the relative position between Fiber-bundle and the emulsion stack, X-ray collimated with a tungsten slit was applied through Fiber-bundle to the four corners of the emulsion stack. The X-ray was extracted from a generator of 70 kV and 15 mA for 0.15 seconds at each position. The tungsten collimator has three 220 μm$^\phi$ holes at 5 mm horizontal intervals.

After the beam exposure, 60 μm$^\phi$ marks were printed at every grid points of 10 mm pitch on the plates by using a black film with holes and a stroboscope. These marks were used to correct the distortion of the plates generated during the development process.

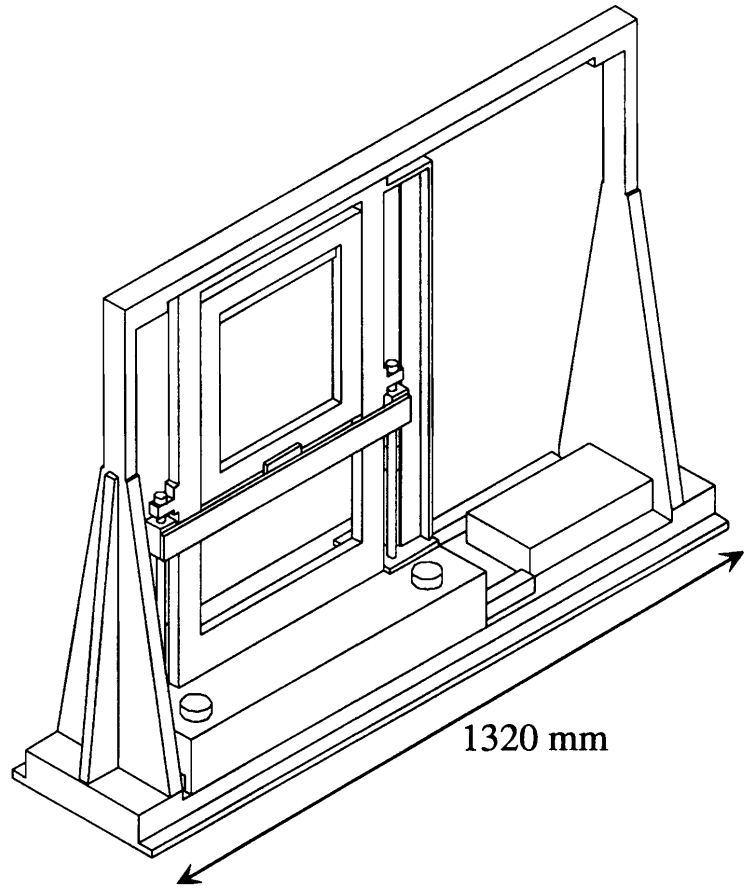

Figure 2.26: Schematic view of the emulsion mover. The emulsion chamber cassette was installed on the square frame located on the upper-left side of the emulsion mover in this figure.

2.7 Trigger

The data-taking trigger was formed in two levels. The first-level trigger distinguished K^+ mesons from pions and K^- mesons using the aerogel Čerenkov counters and the scintillator hodoscopes. The schematic logic diagram of the first-level trigger is shown in Fig.2.28. The K^- beam signal was defined as :

$$K_{beam} = SPILL \otimes T1 \otimes T2 \otimes \overline{BAC1 \otimes BAC2}, \tag{2.1}$$

where $\otimes$ represents the "AND" logic. The $SPILL$ is the spill-gate signal made using the signal from the accelerator. The $T1 \otimes T2$ is the coincidence signal of the TOF counters, which indicates that a particle passed through the beam-line. The $BAC1$ and $BAC2$ are signals from the aerogel counters. The coincident signal of them was used as a veto in order to reduce the overkilling for K^-'s.

The first-level trigger was formed as :

$$K_{beam} \otimes \overline{BVAC} \otimes \overline{FAC} \otimes (CH - FTOFmatrix) \otimes YH \otimes \overline{BUSY}. \tag{2.2}$$

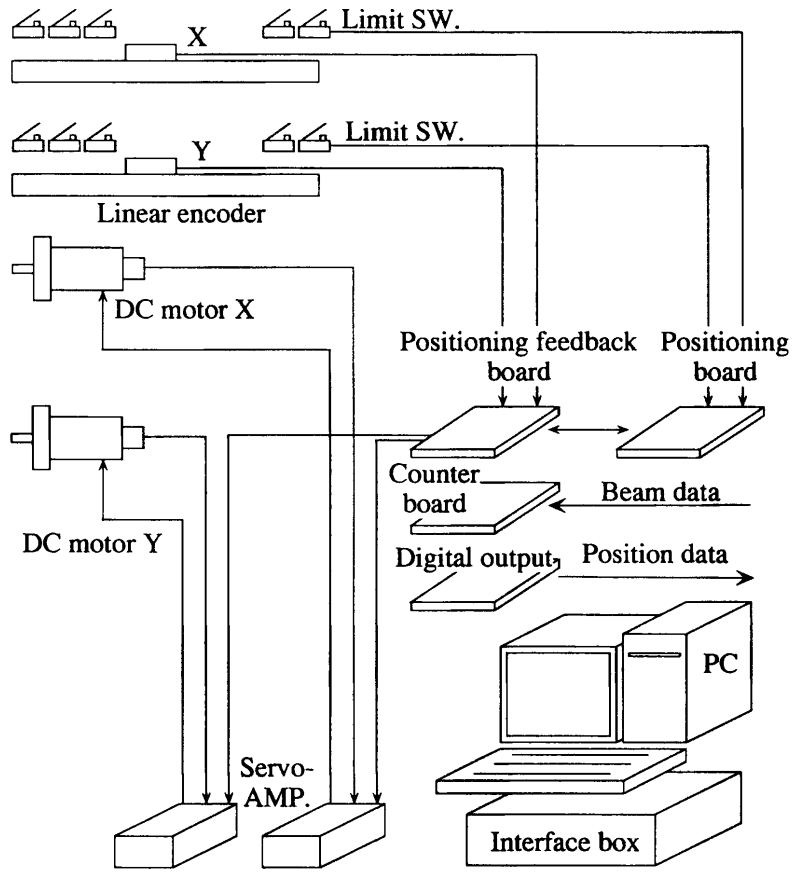

Figure 2.27: Outline of the control system of the emulsion mover.

For the BVAC and FAC detectors, the analog signals from all the PMTs for each detector were summed up using a linear-fan-in-fan-out modules, and the BVAC and FAC logic signals were made from them. The $\overline{BVAC}$ was required to kill the K^-'s which did not interact or were scattered to a small angle, and the $\overline{FAC}$ killed pions. The $(CH - FTOFmatrix)$ is a logic which selects the charge and momentum of a scattered particle. The momentum of a scattered particle was approximately calculated with a combination of two hodoscopes (CH and FTOF). The YH represents the "OR"ed signal from the YH hodoscope. It was required to eliminate the event in which neutral particles hit FTOF.

The timing of the first-level trigger was determined by the T2 signal. Typical trigger rate for the first-level trigger was 75/spill with the K^- intensity of 1.1×10^4/spill. In order to make the decision time short, logic modules for the first-level trigger were located at the experimental area, not at the counting house. The decision time of the first-level trigger was 150 ns. The first-level trigger opened the gate of the 2nd/3rd IIT at 260 ns after a particle passed T2. This includes a delay between the logic-unit for the first-level trigger to the IIT.

The second-level trigger was formed as :

$$(1st\ level) \otimes (mass\ trigger) \otimes (VHx \oplus VHy). \tag{2.3}$$

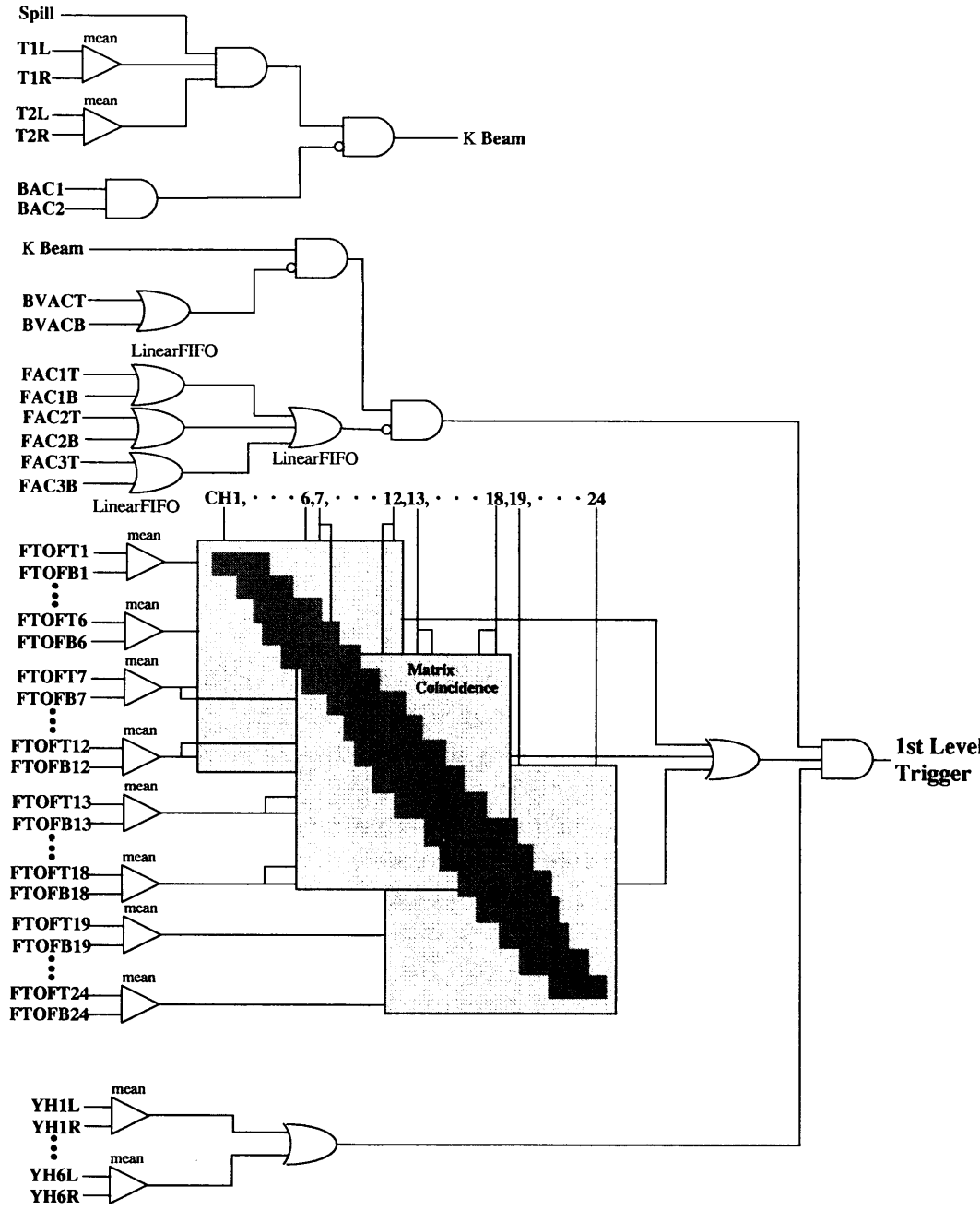

Figure 2.28: Logic diagram of the first-level trigger.

The events selected by the first-level trigger contained protons produced via the (K^-, p) reaction as the major background. The K^+ mesons were distinguished from protons with the so-called "mass trigger" using TDC information. The hit positions of CH and FTOF were encoded and stored in the FI/FO memory (Lecroy Data-Stack). The momentum information can be deduced from the bending angle given by the combination of the hits of CH and FTOF. The time-of-flight from T2 to FTOF was digitized with the fast encoding TDC system consisting of TAC's (Lecroy 4303) and ADC's (Lecroy 4400B FERA). The TDC value was examined for every momentum by checking with a pre-loaded table in the Memory-Lookup-Unit (Lecroy MLU). When the data was in the region corresponding to K^+'s, the mass trigger was fired. Details about the mass trigger are described in Refs.[31, 48]. Hits on the x or y plane of VH were required mainly in order to kill K^0_S's produced via the $(K^-, \overline{K^0})$ reaction [3]. Typical decision time of the mass trigger was 14 μs, during which the *BUSY* signal was generated.

Figure 2.29 shows mass distributions of the scattered particle without and with the mass-trigger. With the mass-trigger, the proton contamination was reduced to 18%.

Typical trigger rate for the second-level trigger was 13/spill, and typical dead time of the data taking was 1% in the '98 run.

2.8 Data acquisition

The online data acquisition was controlled by a VME on-board workstation, Hewlett-Packard Model 743 (HP) working with a operating system HP-RT 2.2. A multi-process data-acquisition software system (UNIDAQ) was used.

Signals from the photo-tubes and wire chambers were digitized with CAMAC or TKO[50] modules, and the digitized data were stored in CAMAC or VME memory modules (seven modules were on CAMAC and one was on VME). The digitization was started by the first-level trigger, however, if the second-level trigger was not fired, the data were cleared. The data from the personal computer for the emulsion mover system were stored in CAMAC input-register modules, which contained the information about the position of the emulsion chamber. The CAMAC modules were controlled via Kinetic K3922 Crate Controller and Kinetic K2917 CAMAC-VME interface in the VME crate.

The acquisition of the images from the CCD cameras were performed with the three types of modules, a clock-and-coordinate generator (CCG) module and flash ADC (FADC) modules and first-in-first-out (FI/FO) memory modules. The CCG module provided a common clock (14MHz) to synchronize the whole system, and generated two-dimensional coordinates of each CCD pixel. It initiated a sequence

[3] In '99 and 2000, it was replaced by a new trigger called momentum-selection trigger (MS) which utilized the hit combination of VH, DC1 and FTOF[49]

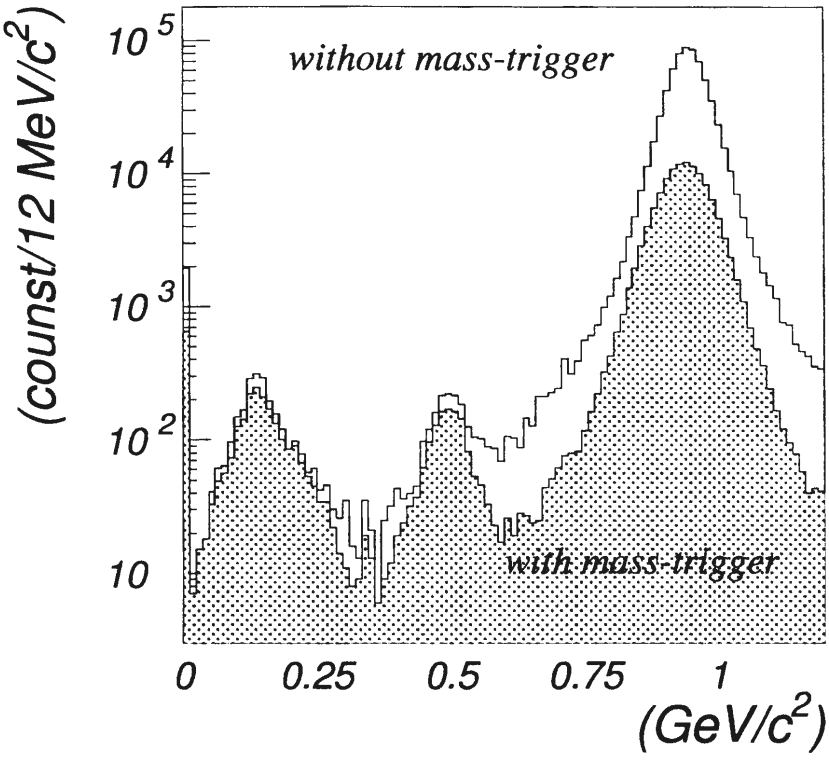

Figure 2.29: Mass distribution for the scattered particles. The white area corresponds to the events taken with only the first-level trigger. The dotted area corresponds to the events taken with the second-level trigger.

of digitization when the second-level trigger was fired. The timing chart of the sequence is shown in Fig2.31. In the NTSC format, the video signal of one frame consists of two parts, namely, the even-field and odd-field. The two fields are read-out alternately triggered by the vertical synchronization signal (VD). In the '98 run, triggers were not inhibited while acquiring the image data because it would increase the dead time of the data taking pretty much. (At least 15 ms is necessary for the image data taking for one event.) As a result, tracks of two or more successive triggered events appeared in one image, occasionally. There are two kinds of such a overlap image, i.e. half-overlap and full-overlap. As shown in Fig.2.31, when two triggers are fired in two successive fields timing, then three fields data are acquired. The tracks of first event appears in the first two fields, and those of the second event appears in the last two fields. Therefore, only the middle field have the images of the two event. Such a half-overlap image can be resolved into two images by an offline analysis. On the other hand, when two triggers are fired in one field timing, then two fields data are acquired. Both two fields have the images of the two events. Such a full-overlap image cannot be resolved. Track information from the spectrometer system can be used to identify

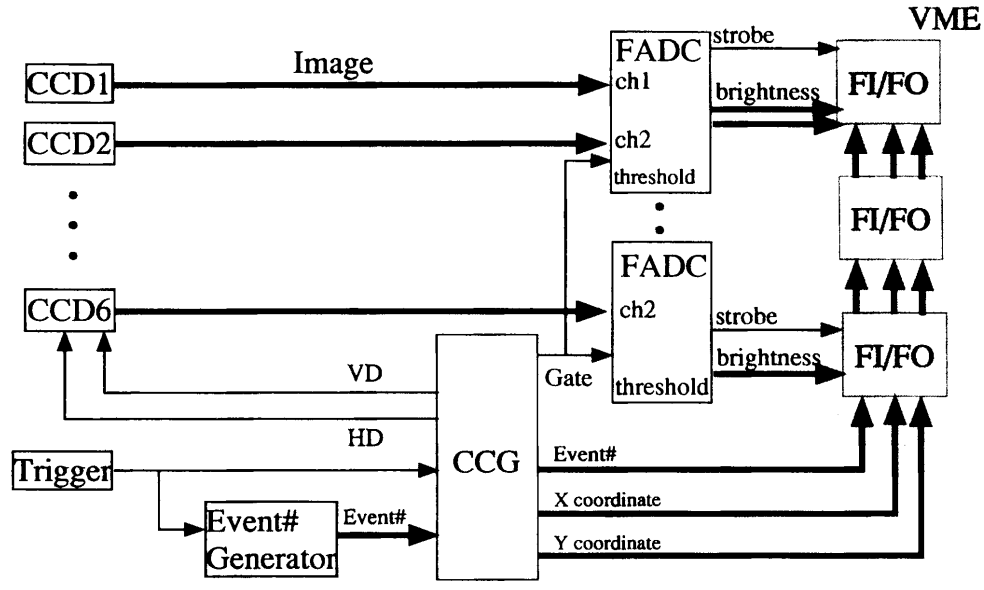

Figure 2.30: Schematic diagram of the image data acquisition.

each event.

The FADC modules digitized the pulse height of the video signals into 8-bit brightness data for each pixel. For the pixels having brightness above some threshold, the write-strobe signals to the corresponding FI/FO module were generated. Then the data on the brightness (8-bit), the coordinates (H:10-bit, V:10-bit) and the event number (4-bit) were stored in the memory of the FI/FO module. Each of the FI/FO modules had four FIFO chips, i.e. IDT-7207 for Fiber-Bundle and SciFi-U-block and IDT-7208 for SciFi-D-Block. The total memory size of a module was 128 kB (IDT-7207×4) or 256 kB (IDT-7208×4).

Details about the image data acquisition system are described in Ref.[51].

During the beam-off period between spills, the data on the memory modules were transfered to HP via VME-bus, and then written to a digital audio tape connected with HP via SCSI-bus. The typical data size was 350 kB/spill.

During the experiment, sample data were transfered from HP to a personal computer working with a operating system Linux via Ethernet. A network buffer manager (net-NOVA) utilizing the TCP/IP protocol controlled the transfer. The data were analyzed on-line on the personal computer to monitor the experimental status. In addition to a normal monitoring of ADC, TDC and register data of the counters and chambers, image data were checked by human eyes with an image browser. The K/π ratio of the beam was monitored for each spill. For the monitoring of the mass trigger setting, sample data were acquired for the events which were selected by the first-level trigger, but not-selected by the second level trigger with a typical pre-scale factor of 1/4. The mass trigger window setting

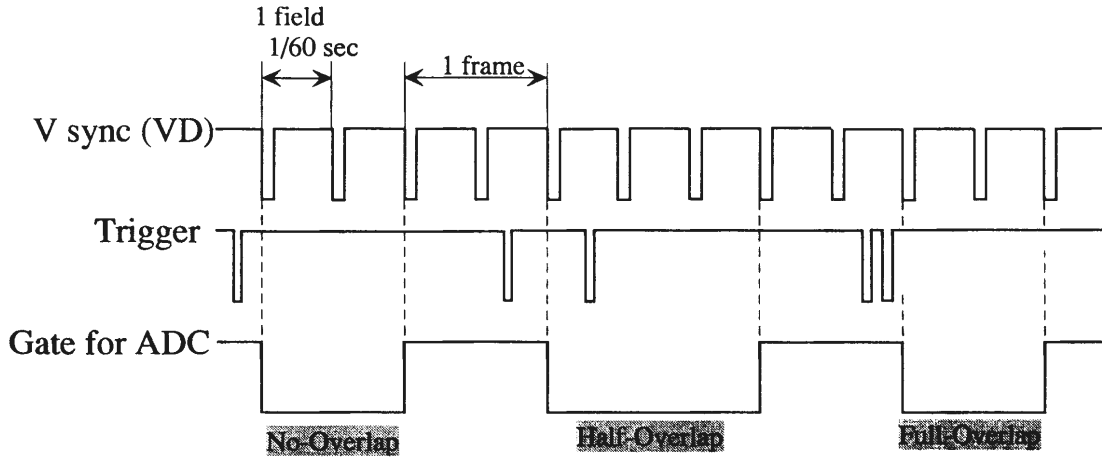

Figure 2.31: Timing chart of the image data acquisition.

was checked by comparing the FERA histograms for all the acquired events and those for the (K^-, K^+) events selected using the reconstructed mass of outgoing particle.

Chapter 3

Spectrometer and image data analysis

In the 1998 run, totally 2.7×10^9 K^-'s were delivered to the diamond target and nuclear emulsion, and data were collected for 7.1×10^6 events with the second-level trigger. The events involving the (K^-, K^+) reaction were selected according to the results of particle identification by the spectrometer data analysis. Among the (K^-, K^+) reaction events, events in which the Ξ^- are likely to have stopped in the emulsion were selected using the image information from SciFi-detectors to reduce the number of events to be analyzed with the emulsion.

3.1 Selection of (K^-, K^+) events by spectrometer data analysis

Even for the events selected with the second-level trigger, the number of K^+'s in outgoing particles was still two orders of magnitude smaller than that of protons. The outgoing K^+'s were identified by reconstructing their masses with the data obtained from the spectrometer system. To reduce the contamination from protons and π^+'s, various cuts were applied. However, emulsion can provide a clear identification of the production of $S = -2$ nuclei with almost no backgrounds. The misidentification of the protons or π^+'s as outgoing K^+'s is not a serious problem. The selection of the clear (K^-, K^+) events is rather important to decrease the number of events to be analyzed with emulsion. From such a standpoint, the criteria to select the (K^-, K^+) reaction events were set rather loosely.

The K^-'s in the beam were selected using the Čerenkov counter at the stage of the online trigger. Figure 3.1 shows a TOF spectrum of the beam particles obtained with T1 and T2. The timing fluctuations due to the pulse-height difference was corrected using ADC information. The events whose TOF value is within the gate indicated by the arrows in Fig.3.1 were selected. The contamination of π^-'s in the beam was 0.27% at this stage.

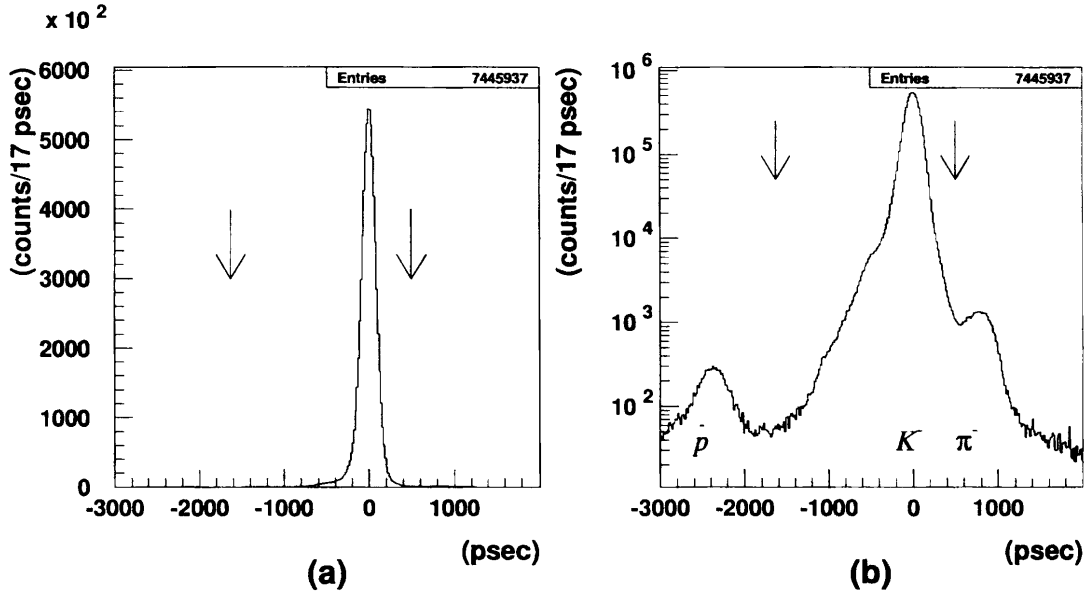

Figure 3.1: The time-of-flight spectra of the beam particles in a linear scale(a) and a logarithmic scale(b). The arrows represent the gate for the TOF value to select K^-'s.

3.1.1 Track reconstruction

Tracks were searched for using an simple straight-line fit in the horizontal and vertical planes, respectively. The track of the incident K^-'s were reconstructed with BPC3,4,5. For the outgoing K^+, track candidates were searched for both upstream and downstream of the spectrometer magnet separately. VH, DC1 and CH were used for the track upstream the magnet, and DC2, DC3, and LST were used for the track downstream. The reaction vertex position was obtained as the closest point of the incident K^- and outgoing K^+ tracks.

To calculate the momentum of an outgoing particle, the particle trajectory through the spectrometer was approximated with a combination of two straight lines upstream and downstream the magnet as shown in Fig.3.2. The crossing position of the two tracks in the horizontal plane was required to be in a region close to the center of the magnet. The field of the spectrometer magnet was modeled by an uniform field with strength B_0 and an effective pole length L_{eff}. To give a correct bending angle, the product of B_0 and L_{eff} was taken to be 1.01 Tesla·m for the particle which traversed the central part of the magnet gap, while the field strength at the center of the magnet pole was 1 Tesla and the pole length was 0.8 m. For the particle which traversed the area close to the pole-piece, the $B_0 \cdot L_{eff}$ was corrected. Within this approximation, the momentum component transverse to the field $p_\perp$ can be expressed as:

$$p_\perp[\mathrm{GeV}] = 0.3 \cdot B_0[\mathrm{Tesla}] \cdot \rho[\mathrm{m}] \tag{3.1}$$

$$= 0.3 \cdot B_0[\mathrm{Tesla}] \cdot \frac{L_{eff}[\mathrm{m}]}{\sin\theta_{in} - \sin\theta_{out}}, \tag{3.2}$$

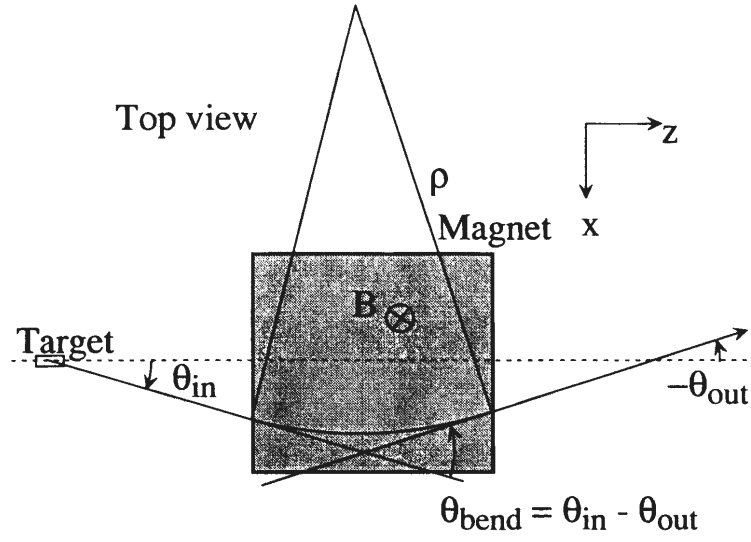

Figure 3.2: Conceptual drawing to show the method to calculate the momentum of the outgoing particle.

where θ_{in} and θ_{out} are the angles of the two straight tracks upstream and down stream the magnet, respectively, projected onto the X-Z plane (see Fig.3.2). The momentum p (GeV/c) was then calculated using the angles of the track upstream the magnet in the X-Z and Y-Z planes. The flight path length L_{path} was calculated by adding the length of two straight lines, from the vertex to the field entrance and from the field exit to FTOF, and the length of the helix orbit in the magnet, using a value of 1.0 m as L_eff.

To eliminate events in which the outgoing particles decayed or scattered before reaching FTOF, the corresponding hit on FTOF was required within ±65 mm in horizontal and ±65 mm in vertical for the track downstream the magnet. The width of a FTOF scintillator was 100 mm. The vertical hit position of FTOF was determined with the r.m.s accuracy of 18 mm from the difference of the timing between two PMT's of FTOF. In order to reduce the deterioration of the timing due to the nuclear interaction in the FTOF scintillator, the hit with a high pulse hight was invalidated. Matching between the position extrapolated from the track downstream the magnet and the hit position on the Y-plane of DC1 was also required.

Tracks were searched for as far as the event had at least two hit planes for each region. The cut parameters were set widely ($\geq 3\sigma$). The inefficiency of the track reconstruction due to the inefficiency of tracking detectors is, therefore, negligible compared to that of the data-taking trigger.

3.1.2 Reconstructed spectra

From the time-of-flight and flight-path-length information, the velocity of the outgoing particle was deduced, taking the distance from T2 to the vertex

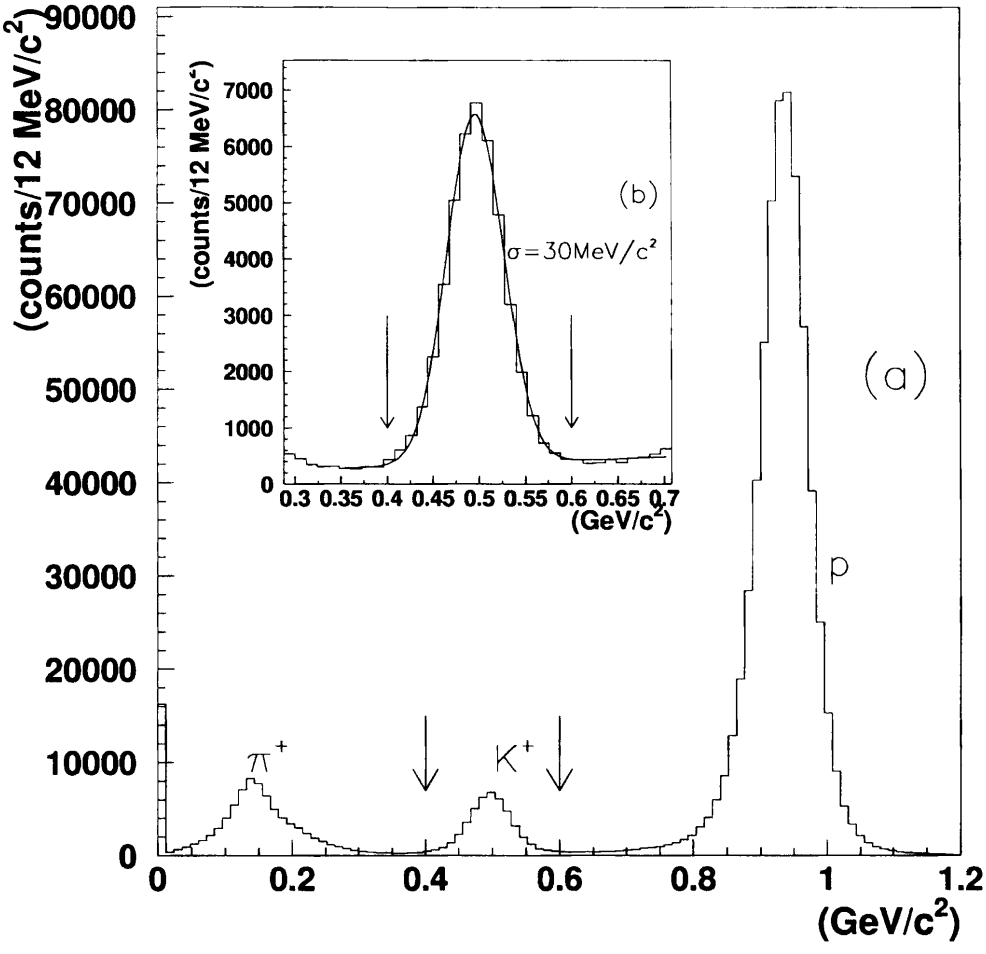

Figure 3.3: Reconstructed mass distribution. The arrows represent the gate for the K^+ selection.

position into account. The mass of the outgoing particles was reconstructed from the momentum and velocity. Because momenta of K^+'s from the quasi-free (K^-, K^+) reaction are expected to be distributed between 0.8 GeV/c to 1.2 GeV/c, only the events in which the outgoing particle had a momentum from 0.4 GeV/c to 1.4 GeV/c were selected. Figure 3.3 shows a reconstructed mass spectrum. The reconstructed mass resolution was 30 MeV/c^2 for the K^+ mesons, from which the momentum resolution was estimated to be 4% (r.m.s) at 1 GeV/c, using a value of 120 ps as the TOF resolution. Particles having a reconstructed mass from 0.4 GeV/c to 0.6 GeV/c were selected as K^+'s. From the data taken in '98, totally 4.6×10^4 (K^-, K^+) events were obtained. The momentum spectrum for the outgoing K^+'s are shown in Fig.3.4(a). For the events selected as the (K^-, K^+) reaction event, missing mass was calculated

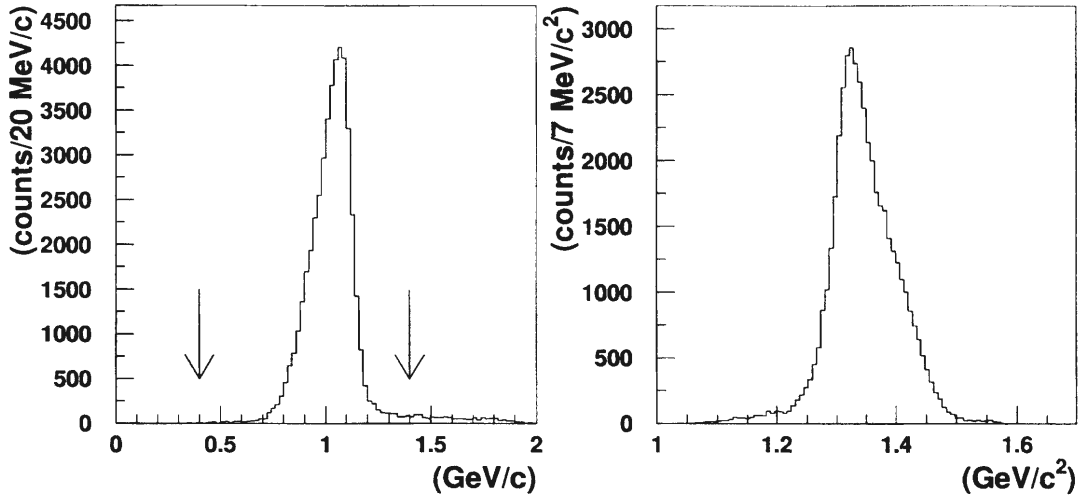

Figure 3.4: (a) Momentum spectrum for K^+'s. The arrows indicate the gate to select the (K^-, K^+) reaction events. (b) Missing mass spectrum of the (K^+, K^-) reaction events obtained assuming the interaction with a proton.

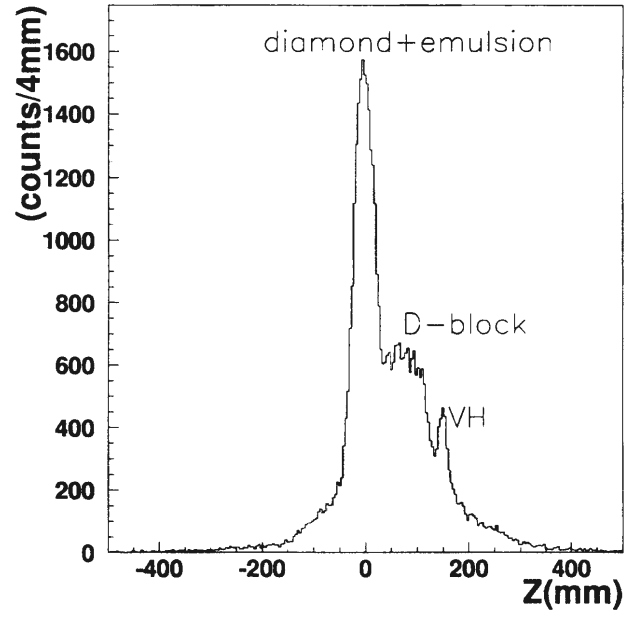

Figure 3.5: Distribution of the vertex positions in the beam direction for the (K^-, K^+) reaction events.

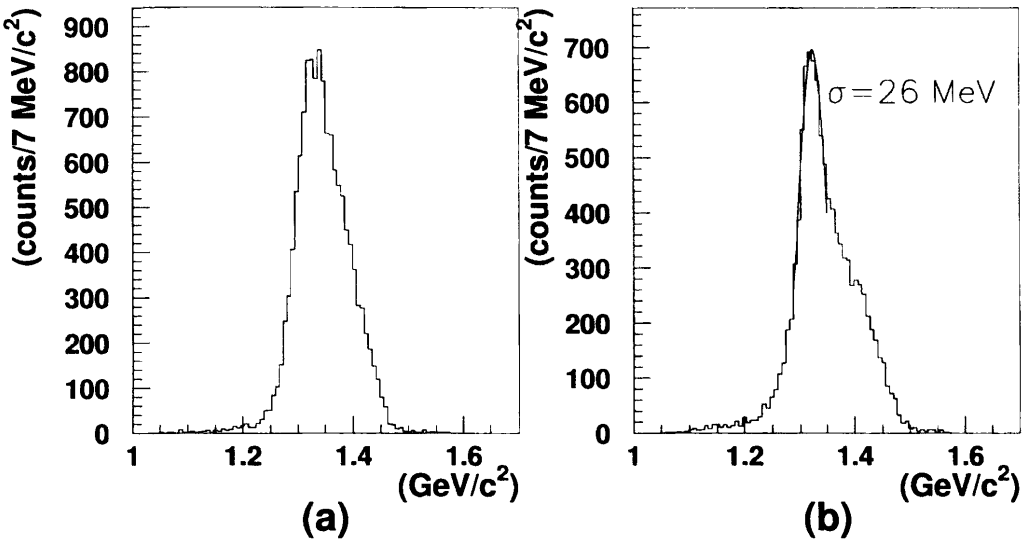

Figure 3.6: Missing mass spectra for (a) the diamond and emulsion region ($Z < 50$ mm) and (b) the D-block region (60 mm$< Z <$ 120 mm), where Z is the vertex position in the beam direction.

from the K^- and K^+ momenta assuming the reaction $K^- + p \rightarrow K^+ + X$. Here, energy loss for K^-'s and K^+'s in the target, emulsion and SciFi-block were taken into account. The obtained missing mass spectrum is shown in Fig.3.4(b). A broad peak corresponding the Ξ^-'s production can be seen. The peak was smeared out due to the Fermi momentum in the target nuclei. Figure 3.5 shows the distribution of the vertex positions in the beam direction. One can see a peak structure originating from the diamond target and emulsion stack, and a bump from the SciFi-D-block. The missing mass spectra for the peak region ($Z < 50$ mm) and the D-block region (60 mm$< Z <$ 120 mm) were obtained as shown in Fig.3.6, assuming the reaction $K^- + p \rightarrow K^+ + X$ again. A rather sharp peak at 1.32 GeV/c^2 in Fig.3.6(b) is considered to correspond to the events on the proton target in the plastic scintillator. From this peak, the missing mass resolution was estimated to be 26 MeV/c^2.

Background estimation

From the mass spectrum, the fraction of the contamination of protons and π^+'s were estimated to be 14% for the selected momentum region (from 0.4 GeV/c to 1.4 GeV/c), and 8% for the particles having a momentum around 1.0 GeV/c. The contamination of π^+ makes a problem because the Σ^- hyperons produced via the (K^-, π^+) reaction can be misidentified as the Ξ^- hyperons. Figure 3.7 shows momentum spectra for various regions of the reconstructed mass. The bump around 1.35 GeV/c in Figs.3.7(a) and (b) corresponds to the production of the Σ^- or $\Sigma(1385)^-$ hyperons via the (quasi-free) (K^-, π^+) reaction. The large peak around 1 GeV/c in Fig.3.7(a) is considered to be originated mainly by the $\pi^+\pi^-$

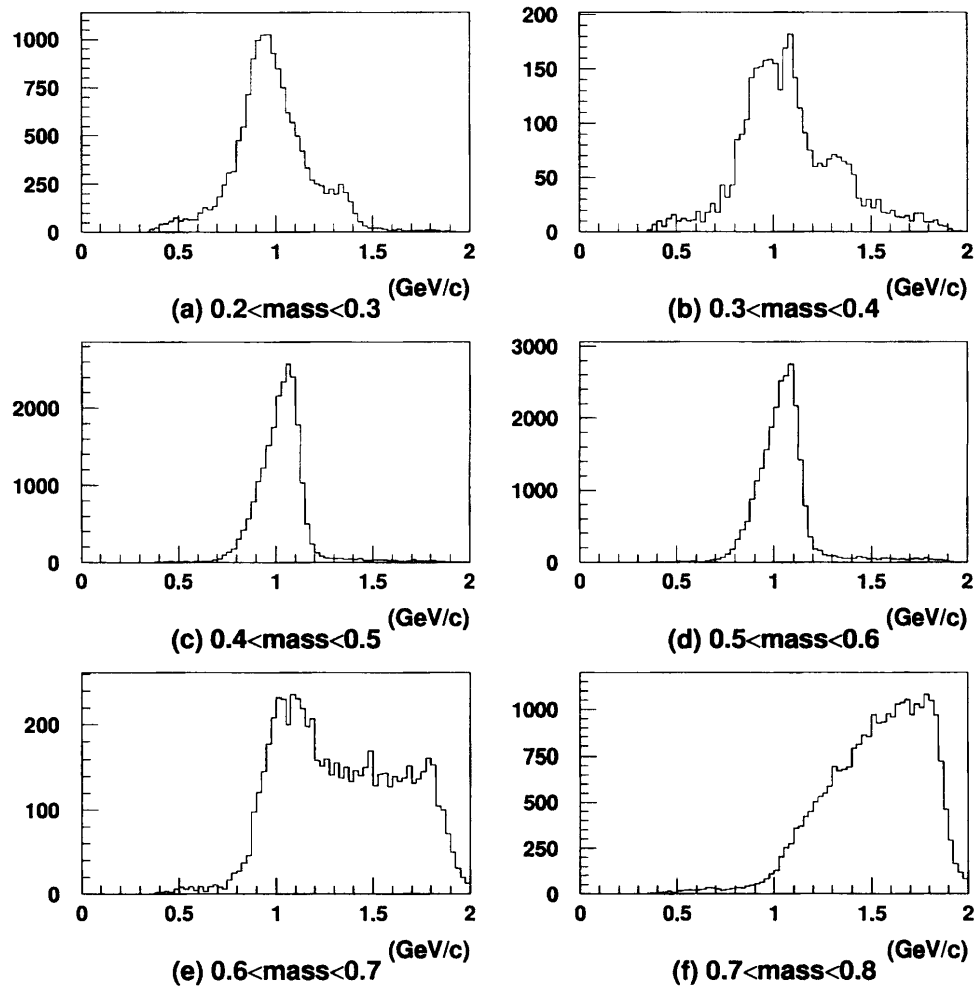

Figure 3.7: Momentum distributions for various regions of the reconstructed mass. A peak originated from the K^+'s can be seen at 1.05 GeV/c in (b) and (e) in addition to (c) and (d).

decay of K^0_s. The π^+ meson from the (K^-, π^+) reaction is expected to have a momentum around 1.45 GeV/c if a Σ^- hyperon was produced, and a momentum around 1.2 GeV/c if a $\Sigma(1385)^-$ hyperon was produced. The $\Sigma(1385)^-$ hyperon decays to $\pi^0\Sigma^-$ with a a branching ratio of 6%. To estimate the upper limit of the Σ^- contamination from the (K^-, π^+) reaction, it is assumed that the misidentified π^+'s having a momentum between 1.3 GeV/c and 1.4 GeV/c was associated with the Σ^- production, and that the misidentified π^+'s having a momentum between 1.05 GeV/c and 1.3 GeV/c was associated with the $\Sigma(1385)^-$ production. Reconstructed mass spectra for the outgoing particle like Fig.3.3 were made both in the outgoing particle's momentum region from 1.3 GeV/c to 1.4 GeV/c (Σ^- production) and from 1.05 GeV/c to 1.3 GeV/c ($\Sigma(1385)^-$ production). From the shape of these reconstructed mass distribution, the upper bound for the π^+ contamination was estimated. The fraction against the total selected events was 0.3% for the Σ^- associated events and 1.5% for the $\Sigma(1385)^-$ associated events. We, therefore, set the upper limit for the Σ^- contamination as 0.4% for the K^+ momentum region between 0.4 GeV/c to 1.4 GeV/c and 0.1% for the K^+ momentum region between 0.4 GeV/c to 1.3 GeV/c.

3.2 Selection of sopping Ξ^- candidates by image data analysis

3.2.1 Image reconstruction

Calibration of IIT+CCD system

Since images amplified by electrostatic IIT's are distorted due to the position dependence of magnification (pin-hole distortion) and the fringing magnetic field, position calibration is necessary. We used a third-order polynomial function to transform the CCD coordinates value to that on the input window of the IIT chain. That is,

$$X = a_x + b_x x + c_x y + d_x x^2 + e_x xy + f_x y^2 + g_x x^3 + h_x x^2 y + i_x xy^2 + j_x y^3 \quad (3.3)$$
$$Y = a_y + b_y x + c_y y + d_y x^2 + e_y xy + f_y y^2 + g_y x^3 + h_y x^2 y + i_y xy^2 + j_y y^3, \quad (3.4)$$

where (x,y) and (X,Y) are coordinates values on the CCD and the input window of the IIT chain, respectively. The parameters $a_x, b_x, ,,$ were determined using a test pattern images. The images were obtained by flashing a black sheet with holes attached on the input window of the IIT with LED. The spectrometer magnet was powered on during these calibration runs. Figure 3.8 shows images of the test pattern before and after the correction taken with a 100^ϕ IIT system for the SciFi-U-block. The distortion seen in Fig.3.8(a) disappeared in Fig.3.8(b).

Decode of "half-overlap" image

As mentioned in Sec.2.8, when two successive data taking triggers were fired

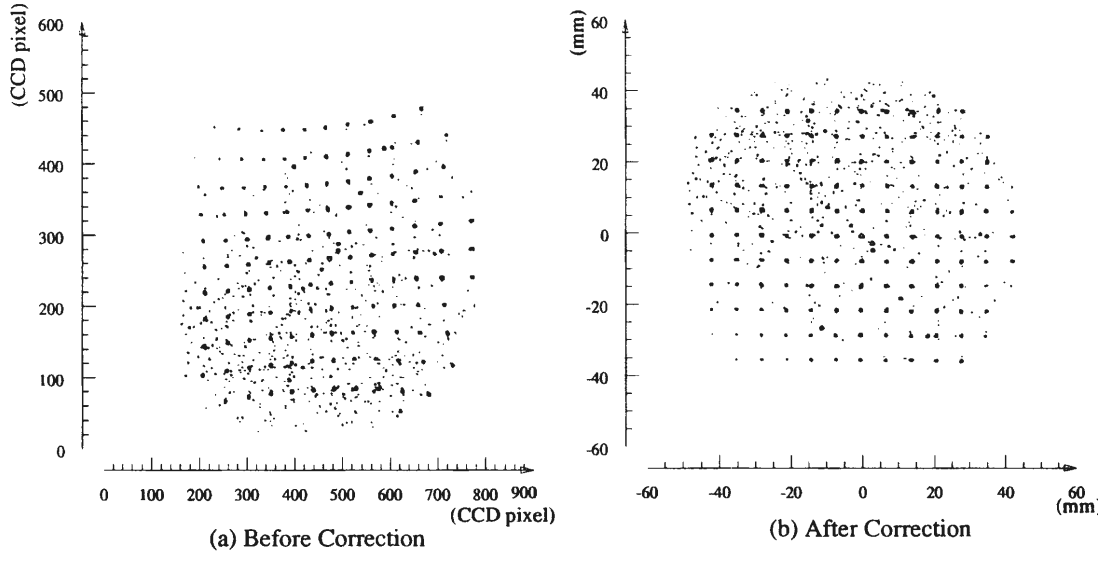

Figure 3.8: Test pattern images (a) before and (b) after the correction.

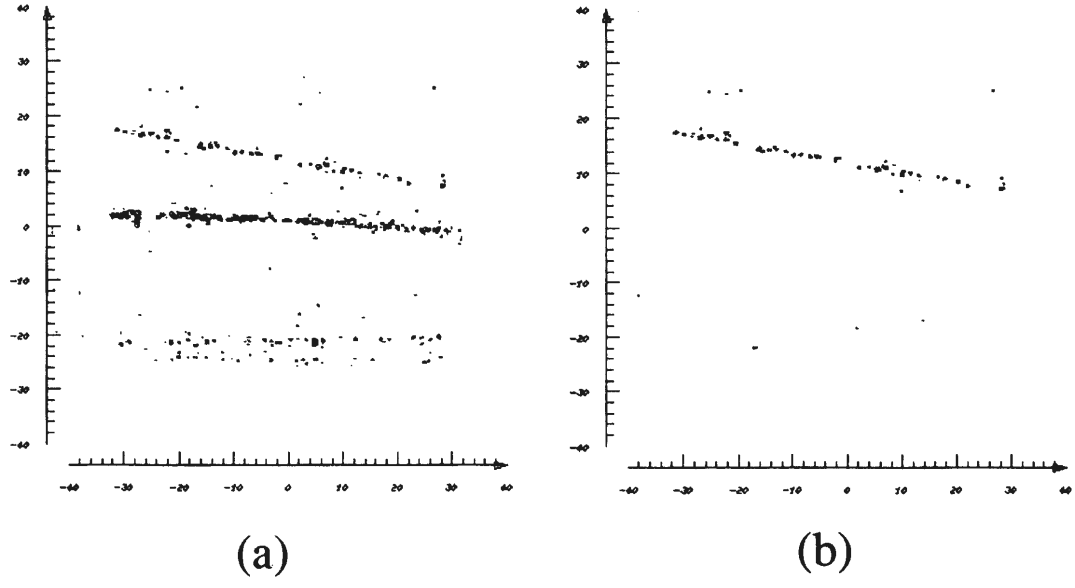

Figure 3.9: Example of an overlap image of the right-side channel of SciFi-D-block. (a)Original image. (b)Image after the "clean-up".

in two successive CCD fields timing, then three fields data were acquired. Tracks of the first event appear in the first two fields, and those of the second event appear in the last two fields. Such a "half-overlap" image can be resolved into two images by the following method. A single-photon image amplified by an IIT chain appears a cluster of several bright pixels on the CCD. Out of the first two interlaced fields (odd and even fields), tracks of the second event appears only in the second field. Therefore, the vertical cluster size of the photons from the second event becomes just one-pixel size. By selecting clusters whose size is larger than one, only the tracks of the first event can be extracted for the image composed of the first two fields. In the same manner, only the tracks of the second event can be extracted for the image composed of the last two fields. We call such an operation as "clean-up". An example of overlap images and the image after the "clean-up" are shown in Fig.3.9.

Image Reconstruction

Fibers consisting the SciFi-detectors were pulled out from the detection volume and were connected to the IIT systems in various manner (See Figs.2.19, 2.20 and 2.22). To get the original track image at the detection volume, the image obtained with the CCD must be reconstructed after the calibration. By accumulating many calibrated images obtained during the experiment on one image, the shape of each fiber-bundle or each mono-fiber sheet can be identified on the image. The position of each fiber-bundle and each mono-fiber sheet on the calibrated image was measured using these accumulated images. The reconstruction parameters were determined for each fiber-bundle or each mono-fiber sheet in order to reproduce the position of the fibers at the detection area in the reconstructed image. Figure 3.10 shows the accumulated images of the left channel of Fiber-bundle before and after the reconstruction.

Shown in Fig.3.11(a) is an example of the images obtained with the SciFi-U-block's right-side CCD. Tracks viewed from two orthogonal directions are superimposed in one image. After applying the reconstruction algorithm, the image of this event becomes as shown in Fig.3.11(b). Production and decay of a Ξ^- is clearly seen. More details about the reconstruction algorithm are described in Ref.[44].

3.2.2 Selection of Ξ^- stop candidates

Among the (K^-, K^+) reaction events selected by the spectrometer data analysis, events in which the Ξ^- is likely to have stopped in the emulsion were selected using the image information from SciFi detectors to reduce the number of events to be analyzed with the emulsion.

As the first step, the brightness information of Fiber-bundle were used to select the event in which highly ionizing particle passed through the Fiber-bundle. For both left- and right-side channels, brightness of an event was calculated by summing up the pulse height values of the pixels The selection criteria was de-

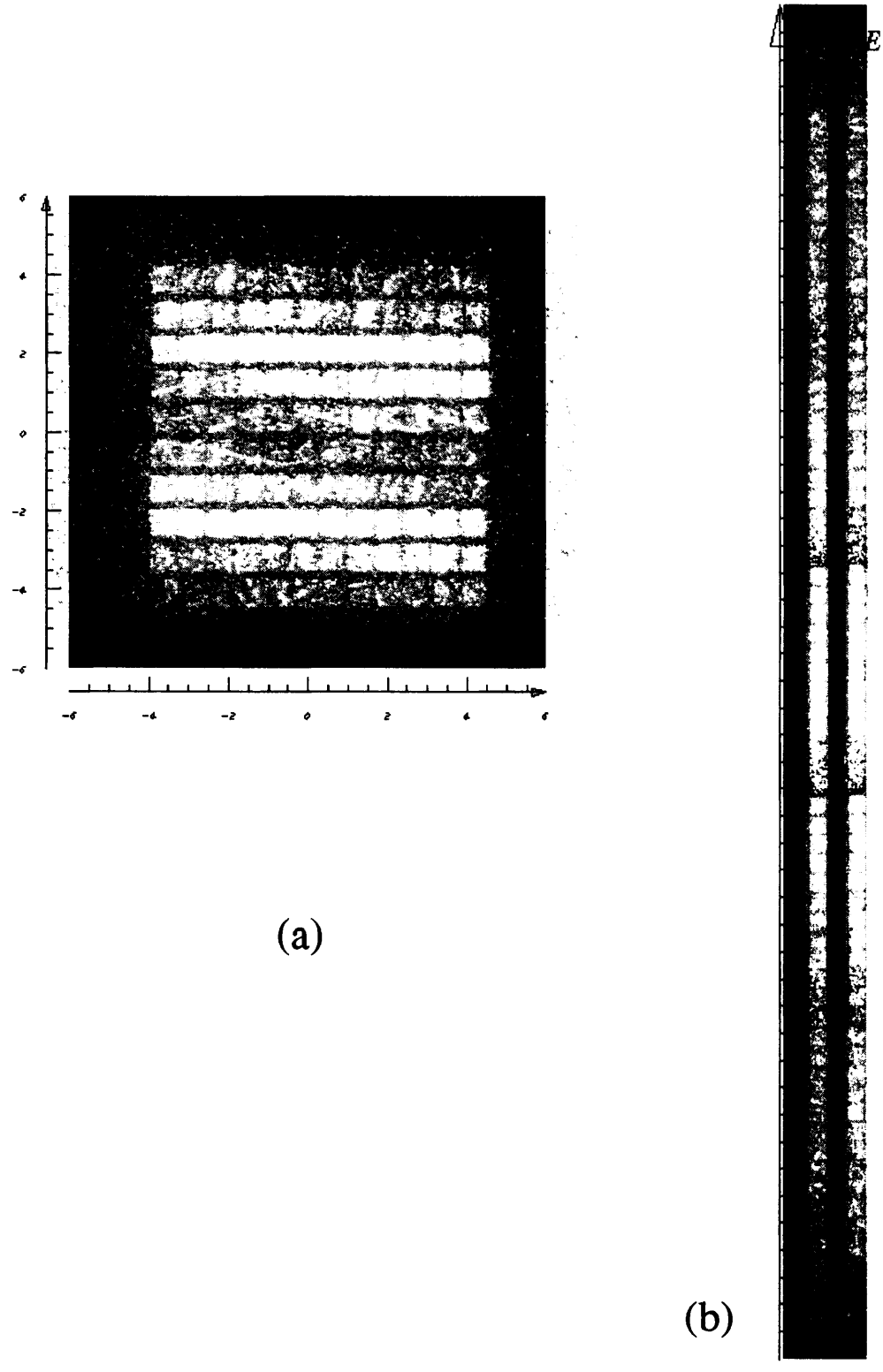

Figure 3.10: Accumulated images of the left channel of Fiber-bundle before(a) and after(b) the reconstruction.

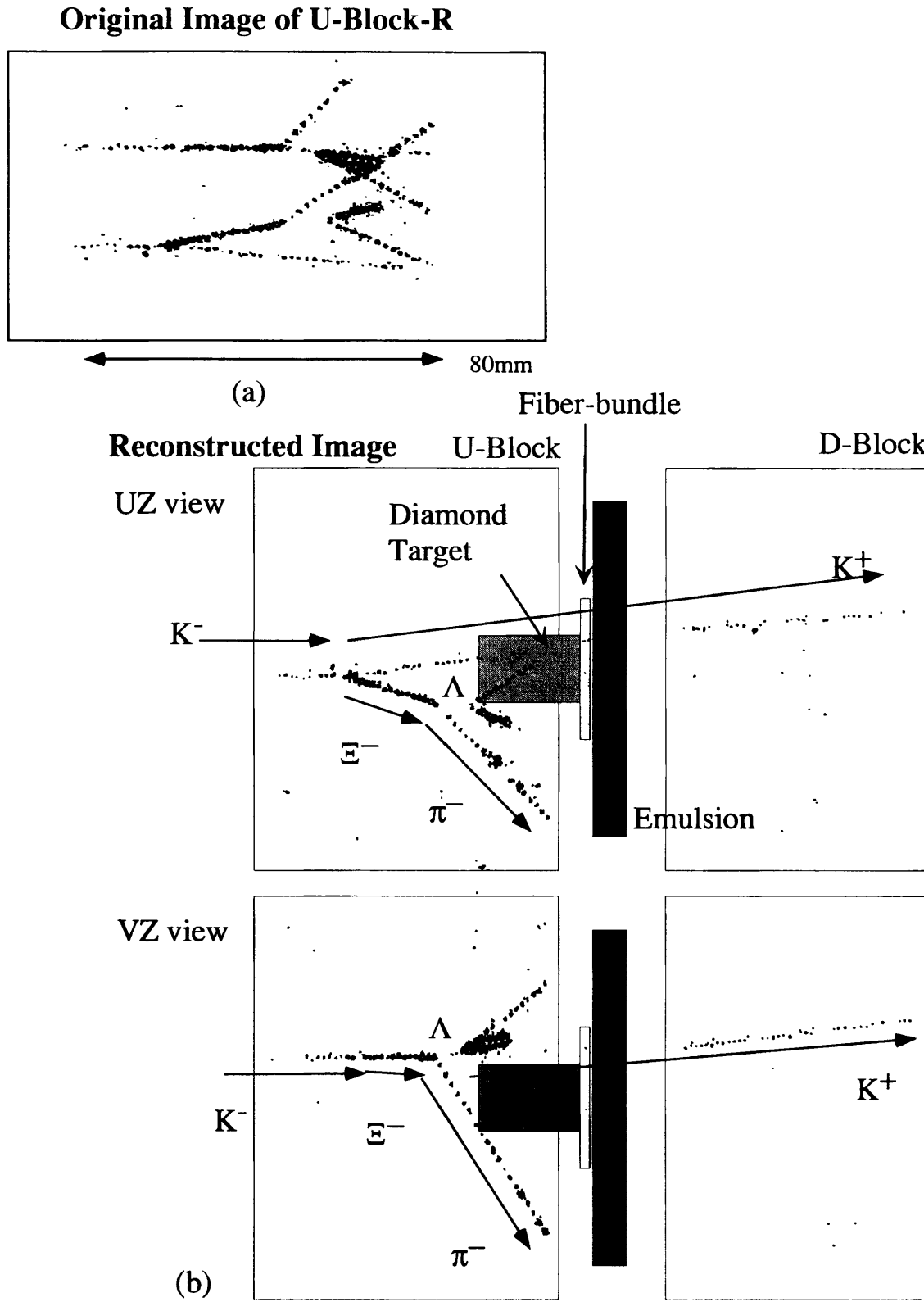

Figure 3.11: An example of images obtained with SciFi detectors. (a)Original image of SciFi-U-block right-side. (b)Reconstructed image of this event. Production and decay of a Ξ^- can be seen.

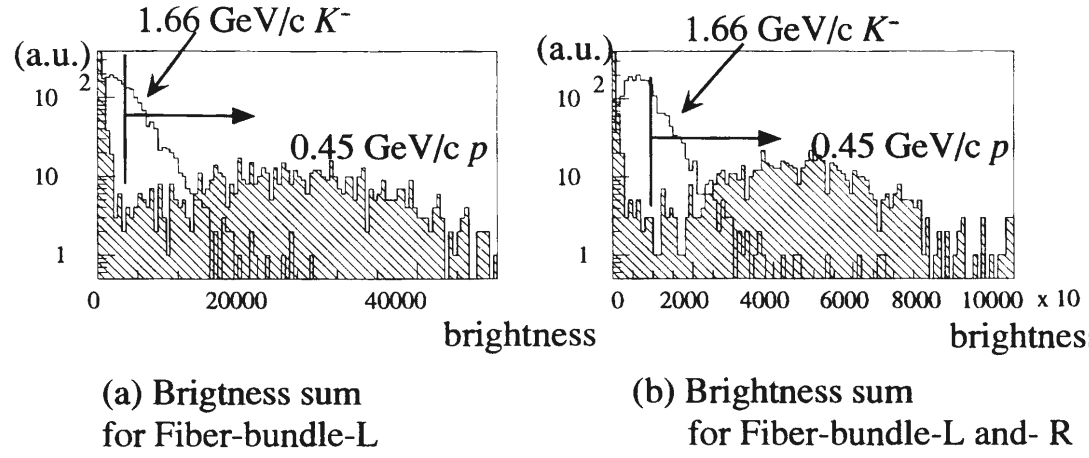

Figure 3.12: Distribution of the brightness from Fiber-bundle for 1.66 GeV/c K^-'s (white area) and 0.45 GeV/c protons (hatched area). (a) Obtained with the right-side channel. (b) Sum of the brightness from the right and left side channels. Since the protons were degrade from 0.55 GeV/c to 0.45 GeV/c in the diamond target, events in which the proton reacted in the target and didn't penetrate Fiber-bundle distribute around zero.

termined by comparing the brightness distribution for 1.66 GeV/c K^-'s and 0.45 GeV/c protons, which are shown in Fig.3.12. Momenta of the stopped Ξ^-'s in the emulsion were estimated to be less than 0.45 GeV/c at Fiber-bundle from a Monte Carlo simulation. If both left- and right-side brightnesses are higher than 3000 and the sum of the two brightnesses is higher than 10000, the event is selected.

For the events remained after the Fiber-bundle's brightness cut, the images from SciFi detectors were scanned by eyes. Firstly, the events were categorized into six types according to it's topology, i.e. "Ξ^- decay", "$H \rightarrow \Sigma^- p$", "two Λ 's", "single Λ", "Just Kink" and "other". The topologies are illustrated in Fig.3.13. The events showing the topology like Fig.3.11 were categorized as "Ξ^- decay" and were rejected. For the other events, the position of the (K^-, K^+) vertex was checked. If it was located downstream the emulsion stack, the event was rejected.

Next, it was checked whether the both two channels (L and R) of Fiber-bundle detected tracks other than those of the K^- or K^+. The track of the K^- or K^+ can be identified with the help of the guideline drawn according to the result of the spectrometer data analysis. If there was a proper track, a linear least-squares fit was applied for pixels comprising the track, where each pixel coordinate was weighted by its brightness. After the fit, active pixels far from the fitted line by 0.16 mm or more were excluded as background contributions, and the track was fitted again. The sum of the brightnesses of pixels comprising the track was calculated for each channel and if it was smaller than 3000, the track was rejected.

Finally, the track which penetrated the emulsion stack was rejected. When it

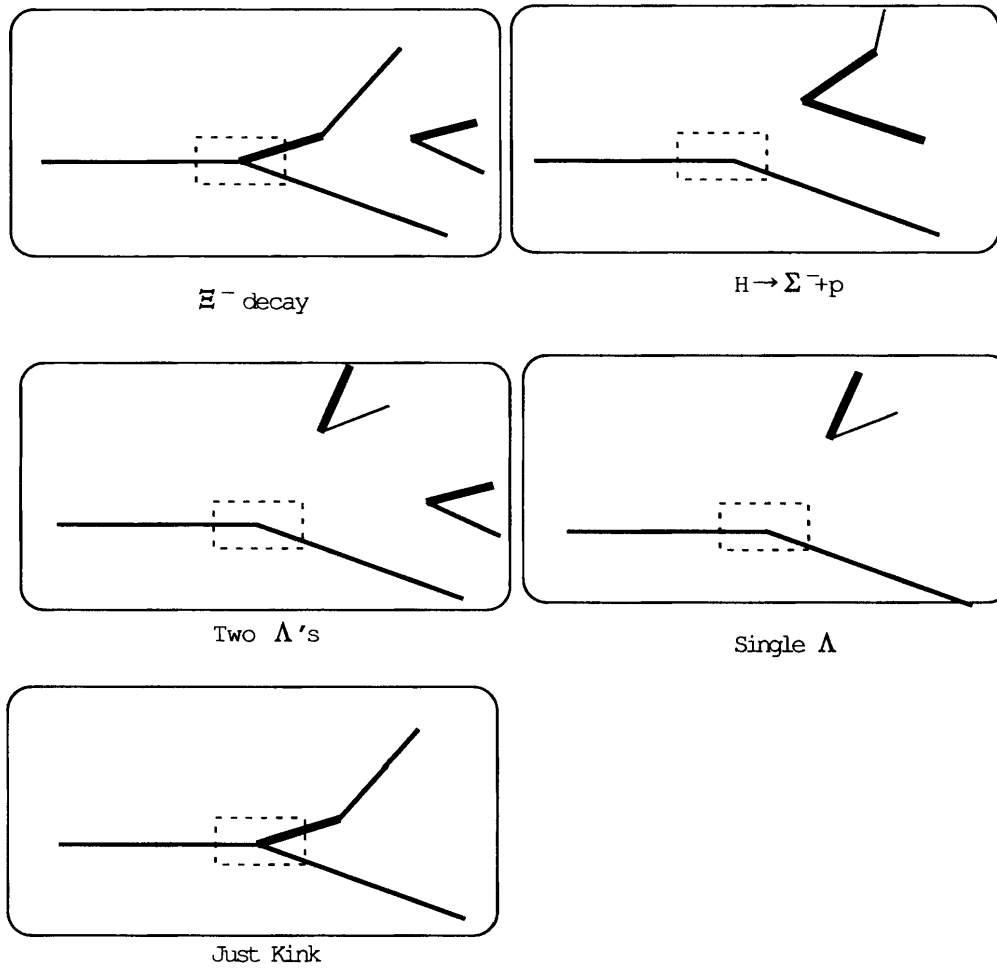

Figure 3.13: Event categorization by its topology. The area surrounded by dotted line might be invisible due to the target or emulsion stack.

is not clear whether it penetrated or not, the track was not rejected.

The selected tracks are the candidates for the tracks of the Ξ^- hyperons which stopped in the emulsion.. Some of the events have two or more tracks other than those of the K^- and K^+. In such a case, the correspondence between tracks in the two channels (L and R) was resolved using the brightness information when the brightnesses of tracks were very much different, otherwise the stereo ambiguity remained and all the combination of tracks in two channels were considered for the later analysis. Table 3.1 summarizes the result of the event selection obtained with the 8% image data analysis of the total data. Spectra of the K^+ momentum, (K^-, K^+) vertex position in the beam direction and missing mass and missing momentum of the $p(K^-, K^+)X$ reaction are shown in Fig.3.14 for the events selected by the image data analysis. The events with a momentum higher than 1.2 GeV/c were reduced significantly. The evens with a missing mass smaller than 1.2 GeV/c^2 and a missing momentum smaller than 0.4 GeV/c were also reduced. This means that the events misidentified as the (K^-, K^+) reaction were reduced significantly. As discussed in Sec.3.1.2, the probability of misidentification of a Σ^- as a Ξ^- is less than 0.1 % in the momentum region smaller than 1.3 GeV/c.

According to the fit result for the track in Fiber-bundle, the position and angle of the track at the surface of the emulsion stack was calculated. The relative position between the Fiber-bundle and the emulsion mover coordinate for each stack was obtained from the X-ray beam described in Sec.2.6, whose position had been detected simultaneously by both Fiber-bundle and the thin-type emulsion.

Table 3.1: Result of the event selection using the image data from the SciFi-detectors.

(K^-, K^+) reaction events	9129
Survived the Fiber-bundle's brightness cut	48%
Among those survived the Fiber-bundle's brightness cut	
Reaction upstream of D-block	65%
Events with track candidates	1221 events
Track candidates	1569 tracks

Categorization of event topology	
Among those survived the Fiber-bundle's brightness cut	
Ξ^- decay	3%
$H \to \Sigma^- p$	0.2%
two Λ's	0.2%
single Λ	7%
Just Kink	6%
other	84%

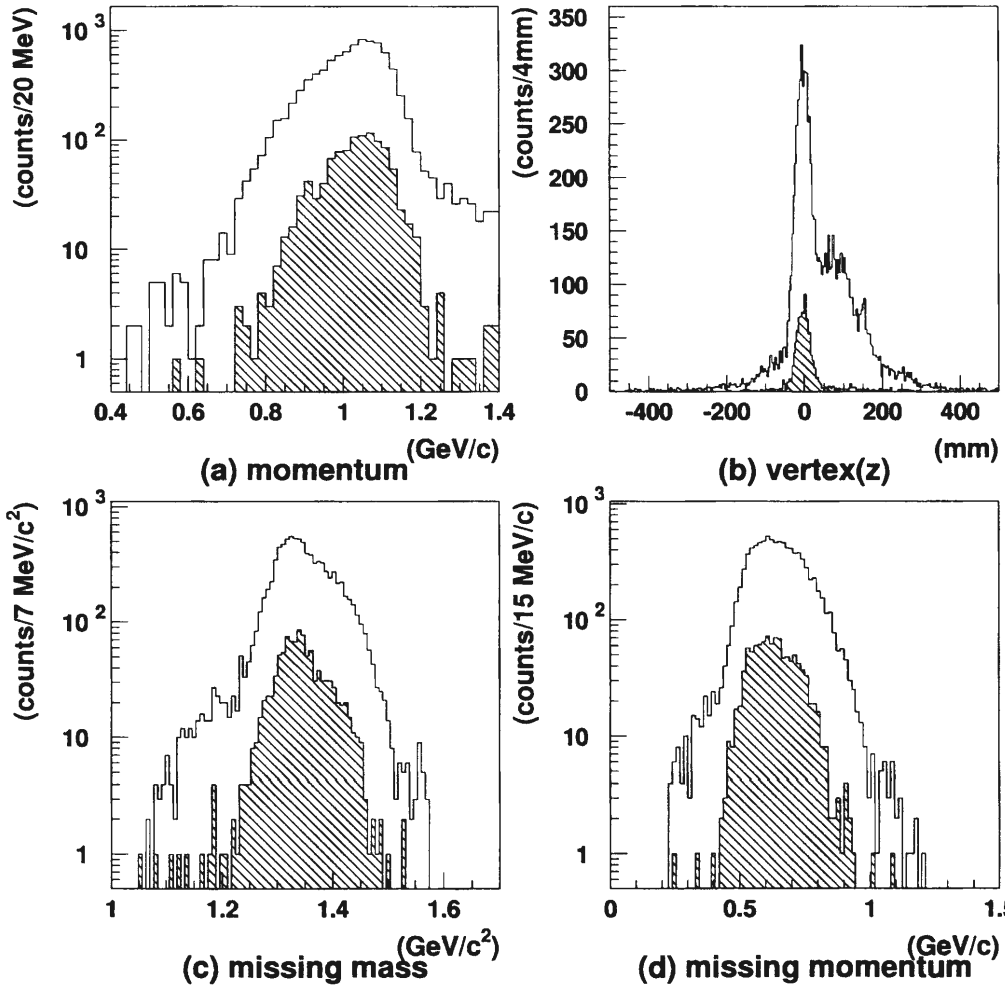

Figure 3.14: Spectra before (white area) and after (hatched area) the event selection by the image data analysis. (a) K^+ momentum. (b) Vertex position in the beam direction. It can be seen that the events in which the reaction occurred in SciFi-D-block were rejected clearly. (c) Missing mass of the $p(K^-, K^+)X$ reaction. (d) Missing momentum of the $p(K^-, K^+)X$ reaction.

Chapter 4

Emulsion scanning

For the events selected by the procedure described in the previous chapter, tracks of Ξ^- candidates were searched for in the most upstream thin-type emulsion plates (#1) in the area of $900 \times 900 \mu m^2$ around the position predicted by Fiber-bundle. Among about 10,000 tracks in this area, tracks having the predicted angle must be searched for. Total number of the events to be analyzed in the emulsion is about 2×10^4. If they were scanned by human eyes, it would take very long time and would be difficult to maintain the efficiency. We have, therefore, developed an automatic track scanning system.

4.1 Automatic track scanning system

4.1.1 Hardware configuration

The hardware configuration of the microscope system is shown schematically in Fig.4.1. Adopted as the microscope stage was NIKON L-mic NK35-2 which can move within a 350 mm $\times$ 350 mm area in horizontal directions. For the scanning, an objective lens having the magnification of 50 (TIYODA) is mainly used. A personal computer acquires the pictures from a CCD camera (HAMAMATSU C3077) by a video board (HITACHI IP5000), which has a digitization depth of 8 bit. The video board has abilities of image processing such as threshold subtraction. The stage is moved in the vertical (focusing) and horizontal directions by stepping motors drived by motor drivers, which are controlled via a motor control board on the PC. The position is measured by linear encoders, the signals of which are read by a parallel I/O board on the PC. The PC controls whole the system.

Figure 4.2 shows a picture of the system.

4.1.2 Automatic track finding

Tracks having a definite angle predicted by Fiber-bundle were searched for in the thin-type emulsion plates automatically. The basic idea was proposed

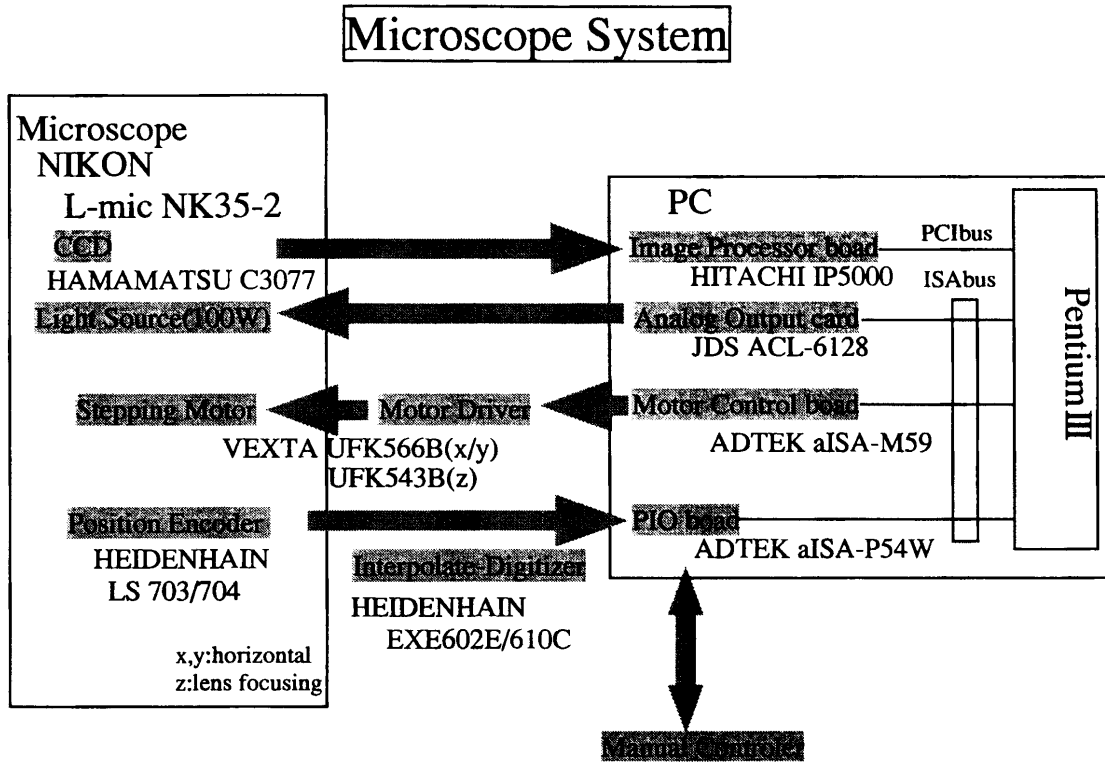

Figure 4.1: Hardware configuration of the microscope system

by Nagoya group[52], which is illustrated in Fig.4.3. The focusing depth of the microscope is about 3 μm. Thus, a picture obtained via a microscope is a tomographic image of about 3 μm thickness. Raising or lowering the focal plane of the microscope's objective lens through whole emulsion depth, tomographic images at various depth of the emulsion can be obtained. Offset values for the position $(\Delta x, \Delta y)$ are calculated for each tomographic image in proportion to the specified track angle and it's depth in the emulsion. After shifting images with these offset values to keep the image of the track at the same position, they are summed up to one superimposed image. Only tracks having a same angle as the specified one makes a sharp peak in the superimposed image. The track having a specified angle can be found by finding such peaks.

The present scanning system has been developed independently from Nagoya group in order to meet the requirement of our experiment. Around the position predicted by Fiber-bundle, tracks are searched for by executing following procedures.

Brightness adjustment

Transparency of the emulsion is not uniform over the plate. In order to obtain constant optical condition, "brightness" is adjusted to a certain value by varying the voltage of the light source power supply at each position of the microscope stage. Since the mean brightness of pixels depends on the track density and

Figure 4.2: Microscope system

contrast of the image, the "brightness" was defined as a median of the brightness of pixels. Due to the rather slow response of the light source, it would take a few seconds if it was adjusted by trying at several voltages. It was found that the brightness and the voltage obey following relation approximately,

$$(\text{brightness}) = a \times \log(\text{voltage}) + b, \tag{4.1}$$

where b is a constant for the plate and a changes at different positions. Brightness is measured each time the microscope stage is moved. If the measured value is different from the prescribed one beyond the prescribed limit, the voltage is set to the value calculated from the above relation with the measured brightness value and the voltage at that time, and brightness is measured again. This procedure is repeated until the brightness becomes the value within the prescribed region.

Recognition of the gel position

As denoted in Sec.2.6, the emulsion plate was made by coating emulsion gel on both sides of a transparent plastic film base. Although the plates were fabricated very carefully, thickness of the gel or base varies by several tens of micro meter in a plate. Therefore, the vertical (focusing) position of the surfaces of the gel is

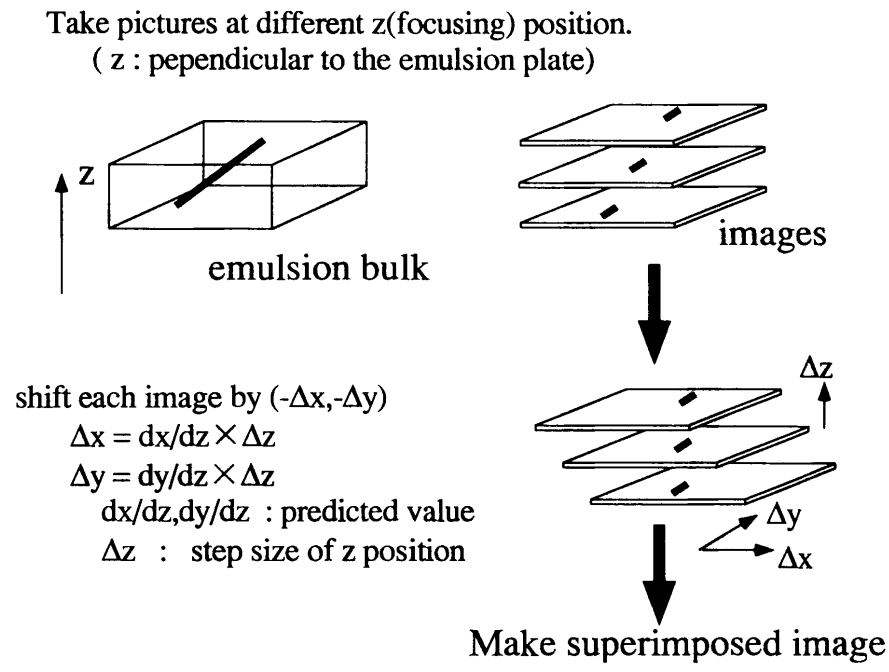

Figure 4.3: Concept of the automatic track finding method.

measured at each position of the stage. It is measured by varying the focusing position and judging whether the current focal plane is inside the gel or not. Because the contrast is not uniform even in one picture, simple counting of the number of pixels above some threshold dose not work to judge the focal plane position. Instead, Laplacian filter is operated to the image at that place and the number of pixels whose Laplacian coefficient is larger than 45 is counted. If the number exceeds some threshold value, it is judged that the gel is in focus. It was found that such a number inside the gel is at least four times as large as that outside the gel even for the thick-type emulsion whose contrast is much worse than that of the thin-type one.

Measurement of the nearest grid mark position

As denoted in Sec.2.6, 60 μm^{ϕ} marks had been printed at every grid points of 10 mm pitch on the plates after the beam exposure for the purpose of the correction of the distortion of the plates. Although the correction parameter is determined prior to the scanning as described in Sec.4.2.1, plates expands and contracts due to the change of the temperature during the scanning. Therefore, each time after the stage is moved a large distance ($\geq$ 10 mm), the position is corrected by measuring the position of the nearest grid mark. The mark is identified and it's position is measured by a following algorithm utilizing the fact that the diameter of a mark is smaller than the size of one picture.

1. The stage is moved to the position where the mark is expected to be found using the correction parameter determined prior to the scanning.

2. A picture was taken at that position.

3. The number of hit pixels in the picture is counted (n_{total}). (A pixel whose brightness is lower than 60 is judged as "hit".)

4. If n_{total} is larger than 10,000, it is judged that the part or whole of the mark exists in the frame. Otherwise, the mark is searched at the next frame. The position of the next frame is determined so that the search is put forward in a spiral centered at the initial position.

5. For each of four sides of the picture, number of hit pixels out of 10 rows/columns on that side is counted ($n_{\text{top}}, n_{\text{bottom}}, n_{\text{left}}, n_{\text{right}}$).

6. If both of n_{top} and n_{bottom} are larger than 1,000 or both of n_{right} and n_{left} are larger than 1,000, it is judged that big stains exists in the frame and the mark is searched at the next frame.

7. The center position of the hit pixels weighted by their brightness is calculated.

8. If at least one of $n_{\text{top}}, n_{\text{bottom}}, n_{\text{left}}, n_{\text{right}}$ is larger than 1,000, the stage is moved to the center position and procedures from 2 are repeated.

9. If n_{total} is smaller than 50,000, it is judged that small stains exists in the frame and the mark is searched at the next frame.

10. It is judged that the entire mark exists in the picture. The center position is recognized as the position of the mark. The search completes.

Acquisition of pictures

As described in the beginning of this chapter, images are taken at various depths in the gel. To shorten the time for this procedure, the images are taken while moving the microscope's objective lens continuously. The speed of the movement is determined depending on the specified angle so that a track moves a certain distance ($\sim$ 20μm) in perpendicular to the focusing direction while eight CCD frames are acquired ($\sim$ 240 ms). Because the image accumulation timings are different for the two fields in one frame, images at sixteen focusing positions are obtained. For each pixel of the images, the brightness is reversed so that grain spots have higher brightnesses, that is, a positive image is made from a negative one. Then, the brightness is subtracted by a certain threshold value. Pixels having lower brightnesses than the threshold are set to have a zero brightness. This reversal and threshold subtraction procedure is done on the video board in a pipe line mode, so that one frame is processed in one CCD cycle ($\sim$30 ms). Sometimes, the surface of the emulsion is dirty and big stains spread out in the image. Normal grains made by a passage of a charge particle have a size of several CCD pixels. Therefore, a bright spot having a size greater than

8×10 pixels is removed from the image as a dust. The obtained field images are called as "original layer images" here after.

Track finding

In the actual scanning of thin-type emulsion plates, tracks had to be searched for in the angular region ($\tan\theta$) of ± 0.1 around a specified value. The angular region which can be searched by the one procedure depends on the grain size, CCD pixel size, focusing depth and scanning depth. The scanning depth in one procedure is limited the size of one picture. With our emulsion and CCD camera, the angular region to be searched in one procedure is about ± 0.04. In order to search for tracks in the angular region of ± 0.1 quickly, a following method was adopted.

1. Monochromatic (0 or 1) images with worse resolution are made from the original layer images by summing every 6(H)×3(V) pixels into one pixel. (Already, the vertical resolution is twice worse for a field image.) When at least one out of 6(H)×3(V) pixels has non-zero brightness, the corresponding pixel on the coarse layer image is set to one. These images are called as "coarse layer images".

2. A superimposed image is made with the first four coarse layer images after shifting each image with the offset value calculated from the predicted angle. On that image, pixels having at least two hit layers are selected as candidates for the track.

3. The angular region of ± 0.1 around the predicted value is divided into 5×5 regions. For each angular region, new offset values are calculated using the center value of that region. A superimposed image is made with these offset values by summing the image obtained in the procedure "2" and the remaining 12 coarse layer images. If the pixel selected by the above procedure has a value larger than some threshold on this new superimposed image, then it is selected as a candidate for the track. The threshold is set depending on the angle. Typical value is 12 layers.

4. Among the selected pixels in the procedure 3, the adjacent pixels are clusterized.

5. For each of the cluster, the corresponding pixels on the original layer images are selected. If the brightness sum of these pixels exceeds some threshold value, the cluster is selected as a candidate. If the sum is larger than a certain value, the cluster is rejected as a background due to stains in the emulsion.

6. For each of the original layer images, the hit pixels around the cluster center are selected and the center position is calculated as the median of the position of pixels weighted by their brightnesses.

7. The position and angle of the track are obtained by applying a linear least-squares fit for the track center positions against the emulsion depth both in two (X and Y) directions. If the χ-square is larger than some threshold, it is rejected as a misidentification.

Typically, it takes about 0.7 ms to search for tracks at one position. For one prediction made by Fiber-bundle, about 3.5 minutes is necessary to scan a $900 \times 900 \mu m^2$ area in the thin-type plates.

4.2 Calibration

4.2.1 Correction of distortion

The emulsion plates were distorted during development process. Especially the thick type plates have very large distortion. For the purpose of the correction of this distortion, 60 μm^{ϕ} marks had been printed at every grid points of 10 mm pitch on the plates after the beam exposure, as denoted in Sec.2.6. Figure 4.4 shows an example of the distortion of a thick-type plate measured using the grid marks, where the displacement from the original position was magnified by 100 times. The distortion was corrected by the bilinear interpolation, the parameter of which was determined by measuring the positions of marks on every grid points of 20 mm pitch. In order to evaluate the correction, we measured the positions of other grid marks on every grid points of 20 mm pitch which were not used to determine the correction parameters. After the correction, the displacement from the original positions was reduced to less than 40 μm. For each of the plates, the correction parameters are measured in prior to the scanning. However, as denoted in Sec.4.1.2, the position of grid marks are measured also during the scanning because plates expands and contracts due to the change of the temperature.

4.2.2 Relative position between plates

The relative position between the most upstream plate (#1) and the next plate (#2) was determined with the X-ray marks at the four corners of the plates. The X-ray marks are measurable only on the plate #1 and #2. For other plates, the relative position was determined by connecting tracks of charged particles in two successive plates. The size of one image viewed with the 50x objective lens is 124×110 μm^2. Therefore, the relative position between plates has to be determined within the accuracy of ± 50 μm. This accuracy was achieved by a following method. Firstly, tracks are searched for in the angular region around 0.3 ($\tan\theta$) in the upstream plate, manually. Three tracks are selected at every four corners of the plate. Then the tracks are searched for in the just downstream plate automatically. By checking the position relation between these three tracks, the real tracks are selected among the several candidates at each corner. From the displacements at four corners, the relative position parameters are determined.

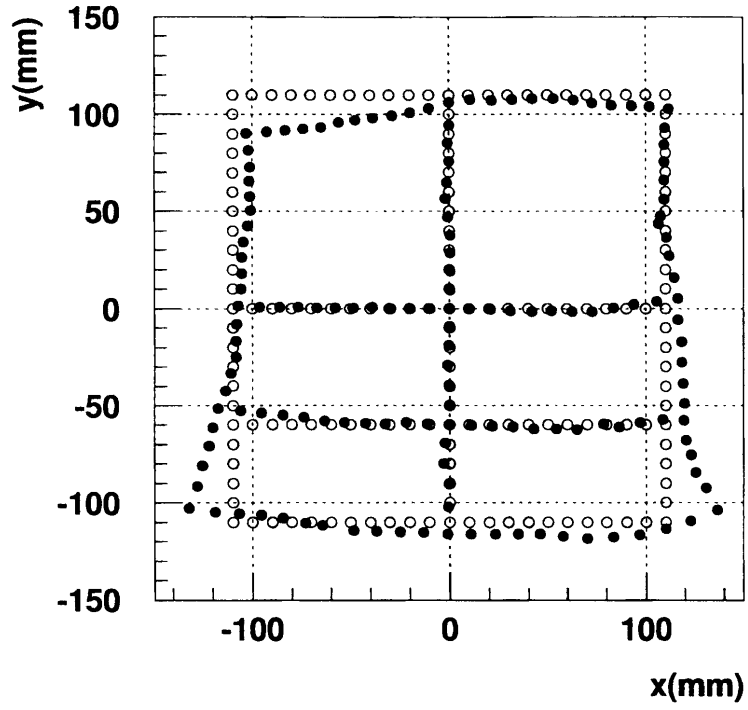

Figure 4.4: Example of the distortion of a thick type emulsion plate. The white circles represent the original position of the grid marks. The black circles represent the positions of grid marks after the development. The displacement from the original position was magnified by 100 times so that it can be seen clearly.

4.3 Automatic scanning on the plate#1 and #2

The search condition ($900 \times 900\ \mu m^2$ area around the predicted position and $-0.1 < \Delta \tan\theta < 0.1$) for the thin type plate (#1) was determined by connecting sample tracks. The detail about the connection of sample tracks are described in Appendix A. The $900 \times 900\ \mu m^2$ area around the predicted position in the plate #1 is divided into regions of about one picture size ($\sim 110 \times 90 \mu m^2$). The size of the region is changed slightly depending on a predicted angle. At each region, tracks having the predicted angle are searched for in the upstream side gel by the automatic scanning system. Once a track is found in the region, the system tries to find the corresponding track in the downstream side gel. If it has found the track, it is accepted as a track candidate. For the track candidates found in the plate#1, corresponding tracks are searched for at the surface of the next plate (#2) by the automatic scanning system. The searched region is $200 \times 200 \mu m^2$ around the expected position and $\pm 0.06(\tan\theta)$ around the angle measured in the plate #1. When the candidate has a corresponding track, it is accepted as a track candidate. At this stage, there still remains misidentified tracks (11%) mainly due to stains in the emulsion. Therefore, the selected track candidate in the plate #1 is checked by human eyes to judge if it is really a track.

Multiple track candidates are found for each prediction by Fiber-Bundle. Figure 4.5 shows the multiplicity of track candidates for various prediction angles, which was obtained from the result of scanning on 6 emulsion stacks.

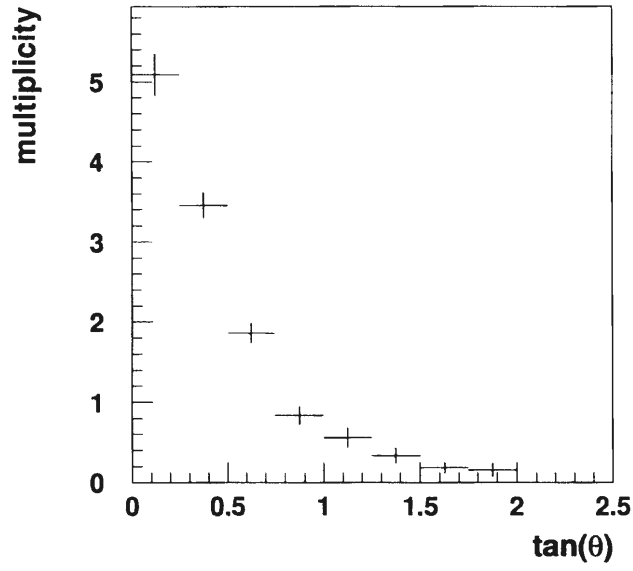

Figure 4.5: Multiplicity of track candidates for various prediction angles. The histogram is obtained from the result of scanning on 6 emulsion stacks.

4.4 Semi-automatic track scanning

The events selected by the automatic scanning on the plate#1 and #2 were scanned in the remaining plates by the automatic scanning system supported by the human eyes check. The track of a heavily ionizing particle such as the Ξ^-'s in our experiment is deflected easily by the multiple scattering. Therefore, the finding efficiency of tracks by the automatic scanning system is not sufficiently high. For example, even if the efficiency is as high as 95% for one plate, the total efficiency becomes only 57% for a track of a particle which had reached the last plate. The track is searched for by the automatic scanning system at four or six depths of the thick type emulsion from upstream side, and every time the scanning result is checked by human eyes. For tracks with $\tan\theta < 0.4$, they are searched for at four depths, and other tracks are searched for at six depths. The searched region is $100 \times 100\mu m^2$ around the expected position and $\pm 0.06(\tan\theta)$ around the angle measured at the previous search. It was found that the finding efficiency at each depth is 90% on the average. Figure 4.6 shows the angular distribution for the measured tracks and angular dependence of the inefficiency of the automatic scanning system.

When the track have reached a vertex, it is categorized into following types according to it's topology.

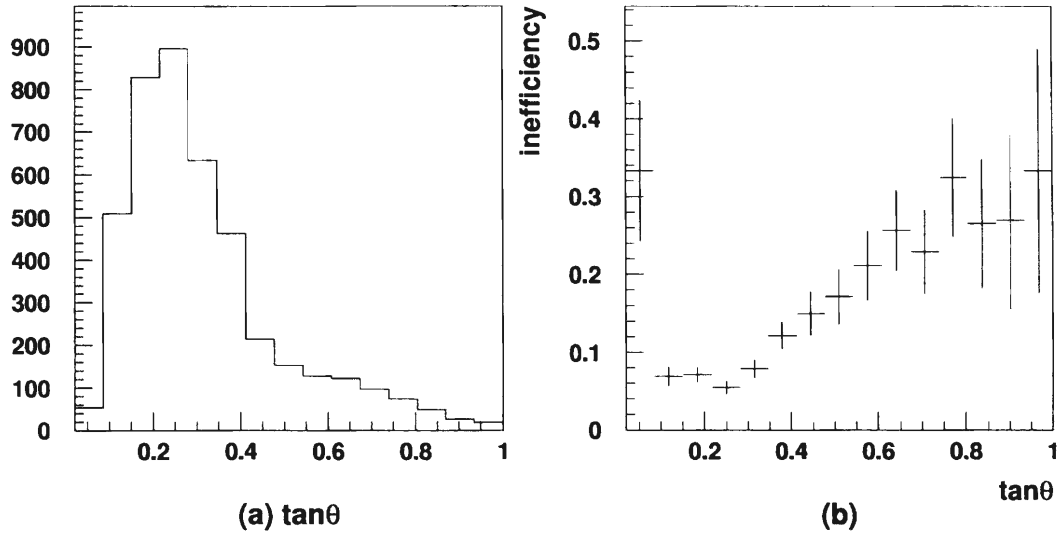

Figure 4.6: (a)Anguler distribution of the measured tracks. (b) Angular dependence of the finding inefficiency of the automatic scanning system.

- σ-stop : At least one evaporation track from the stopping point.
- decay : Decaying into a gray track (π^-) (and an invisible Λ).
- ρ-stop : No evaporation track from the stopping point.
- SI : Reaction without a beam track.
- BI : Reaction with a beam track. The track of the beam particle can be identified as a track which is parallel to the focusing direction.
- other

The σ-stop and ρ-stop events are the candidates for Ξ^- stopping event. However, for the ρ-stop events, it is impossible to distinguish Ξ^- stopping from proton stopping unless an Auger electron is emitted from the stopping point. Whether the particle has stopped or not is judged by the thickness and deflection of the track. When the vertex type is not clearly determined, it is categorized into two or more types.

4.5 Result of the scanning

Until now, 6% of the total emulsion has been scanned. The result of the categorization of the found vertices is summarized in Table 4.1. In the table, the number of vertices categorized uniquely to "σ-stop" or "decay" is listed as "unique σ-stop" or "unique decay". Main part of the events categorized to both "σ-stop" and "SI" is composed of the events in which the traced track has a topology of a

Table 4.1: Result of the categorization of the vertices found in the emulsion.

event	942
predicted track	1183
tracks found in emulsion	2088
σ-stop	87
decay	38
ρ-stop	774
SI	148
BI	195
other	187
unique σ-stop	42
unique decay	30
Hyper-Fragment like	7
Hyper Fragment	6

scattering unique before stopping. The number of the Ξ^--origin σ-stop events is close to "unique σ-stop". although precise evaluation of the vertices is necessary to determine the accurate number. The expected number of Ξ^- stopping events for the scanned emulsion is about 60 from a Monte Carlo simulation based on the E176 result. According to the result of E176[53], 67% of the Ξ^- stopping has a topology of σ-stop. Therefore, the expected number for the Ξ^--origin σ-stop events is 40. This is consistent with the number of the obtained "unique σ-stop" events. Figure 4.7 shows spectra of the outgoing K^+ momentum and missing momentum assuming the $p(K^-, K^+)$ reaction for the "unique σ-stop" events. As expected from the kinematics, the σ-stop events have rather high $K+$ momentum and low missing momentum.

The "Hyper Fragment-like" in Table.4.1 is the event in which two or more vertices seems to be included, but with the limited resolution of the microscope, the separation of the vertices is not clear. For "Hyper Fragment", the two or more vertices are separated clearly. In the E176 experiment, 11 "Hyper Fragment" events were observed among the 78 Ξ^- stopping events[53]. The number of presently obtained "Hyper Fragment" is consistent with the E176 result. Among the six "Hyper Fragment" events, one twin single-Λ hypernuclei event and one double-Λ hypernucleus have been found. These events are described in detail in Chapter 6 and Chapter 7.

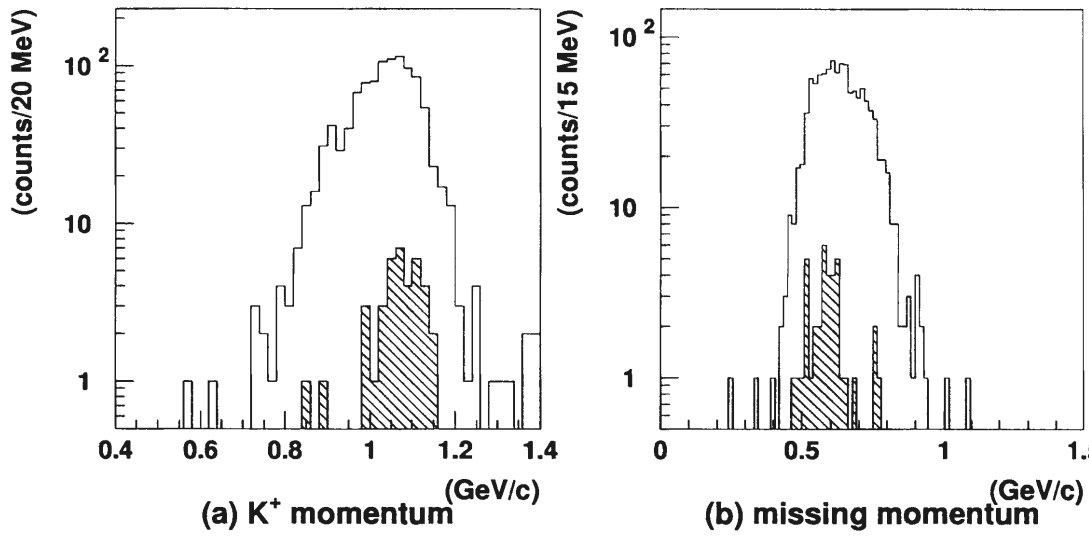

Figure 4.7: Spectra of (a) outgoing K^+ momentum and (b) missing momentum assuming the $p(K^-, K^+)$ reaction. White areas represent the spectra for the events remained after the analysis of the image data from the scifi-detectors. Hatched areas represent those for the "unique σ-stop" events.

Chapter 5

Range and energy measurement with emulsion

5.1 Range-energy calibration

Kinetic energy of a particle stopped in the emulsion was determined from it's range by the range-energy calculation package $SRIM2000$[54]. $SRIM2000$ calculate ranges at various energies, given the composition and density of the material. Although the density of the emulsion gel can be determined from the volume size and weight measured before and after the beam exposure, the accuracy is not sufficient. Therefore, the calibration for the range-energy relation in the emulsion was made using the decay-chain of ^{228}Th which is naturally contaminated in the emulsion gel. The ^{228}Th has following two decay-chains,

$$
\begin{array}{lll}
^{228}\mathrm{Th}(1.91y) \rightarrow & ^{224}\mathrm{Ra}(3.66d) & +\alpha(5.423\mathrm{MeV}) \\
& \downarrow & \\
& ^{220}\mathrm{Rn}(55.6s) & +\alpha(5.7\mathrm{MeV}) \\
& \downarrow & \\
& ^{216}\mathrm{Po}(0.15s) & +\alpha(6.3\mathrm{MeV}) \\
& \downarrow & \\
& ^{212}\mathrm{Pb}(10.64h) & +\alpha(6.3\mathrm{MeV}) \\
& \downarrow & \\
& ^{212}\mathrm{Bi}(60.6m) & +\beta^- \\
& \downarrow & \\
& ^{212}\mathrm{Po}(0.3\mu s) & +\beta^- \\
& \downarrow & \\
& ^{208}\mathrm{Pb} & +\alpha(8.785\mathrm{MeV})
\end{array}
$$

$$
\begin{array}{lll}
^{228}\mathrm{Th}(1.91y) \rightarrow & ^{224}\mathrm{Ra}(3.66d) & +\alpha(5.423\mathrm{MeV}) \\
& \downarrow & \\
& ^{220}\mathrm{Rn}(55.6s) & +\alpha(5.7\mathrm{MeV}) \\
& \downarrow & \\
& ^{216}\mathrm{Po}(0.15s) & +\alpha(6.3\mathrm{MeV}) \\
& \downarrow & \\
& ^{212}\mathrm{Pb}(10.64h) & +\alpha(6.3\mathrm{MeV}) \\
& \downarrow & \\
& ^{212}\mathrm{Bi}(60.6m) & +\beta^- \\
& \downarrow & \\
& ^{208}\mathrm{Tl}(3.053m) & +\alpha(6.1\mathrm{MeV}) \\
& \downarrow & \\
& ^{208}\mathrm{Pb} & +\beta^-
\end{array}
$$

These decay-chains are easily distinguished in the emulsion from it's topology. They have five tracks with the ranges around 40μm. Among α-particles emitted from the ^{228}Th's decay-chains, only that from the ^{212}Po's decay has the kinetic energy larger than 8 MeV and it's range is the longest among five tracks. On the other hand, because the lifetime of ^{224}Ra is much longer than others, the emission point of α particle from the ^{228}Th's decay is separated from others. The track of α particles from the decays of ^{212}Po and ^{228}Th were used for the calibration. The ^{228}Th's decay-chains were searched for in the downstream-side gel of mod#13-plate#5 in which the twin-hypernuclei event was found and the upstream-side gel of mod#16-plate#6 in which the double-Λ hypernucleus was found. Figure 5.1 shows a picture of one of the Th's decay-chains. For each of the decay-chains, the length of the track for α from the decay of ^{212}Po or ^{228}Th was measured in the x, y and z direction, where z is the focusing direction of the microscope. The range of the track, R, is expressed as,

$$R = \sqrt{\Delta x^2 + \Delta y^2 + \Delta z^2 \times S^2} \tag{5.1}$$

with Δx, Δy and Δz as the lengths in the x, y and z direction respectively. The S is the shrinkage factor for the emulsion gel, defined by the ratio of the original thickness of the plate to the thickness at the measurement. Typical value of S is 2.0.

Figures 5.2(a) and 5.3(a) show the scatter plots for the measured Δz^2 versus $(\Delta x^2 + \Delta y^2)$ in mod#13-plate#5. The mean range of 48.4μm for the α from ^{212}Po and 23.6μm for that from ^{228}Th were obtained by the linear least squares fit to the plots. With $SRIM2000$, the density of the emulsion gel which gives

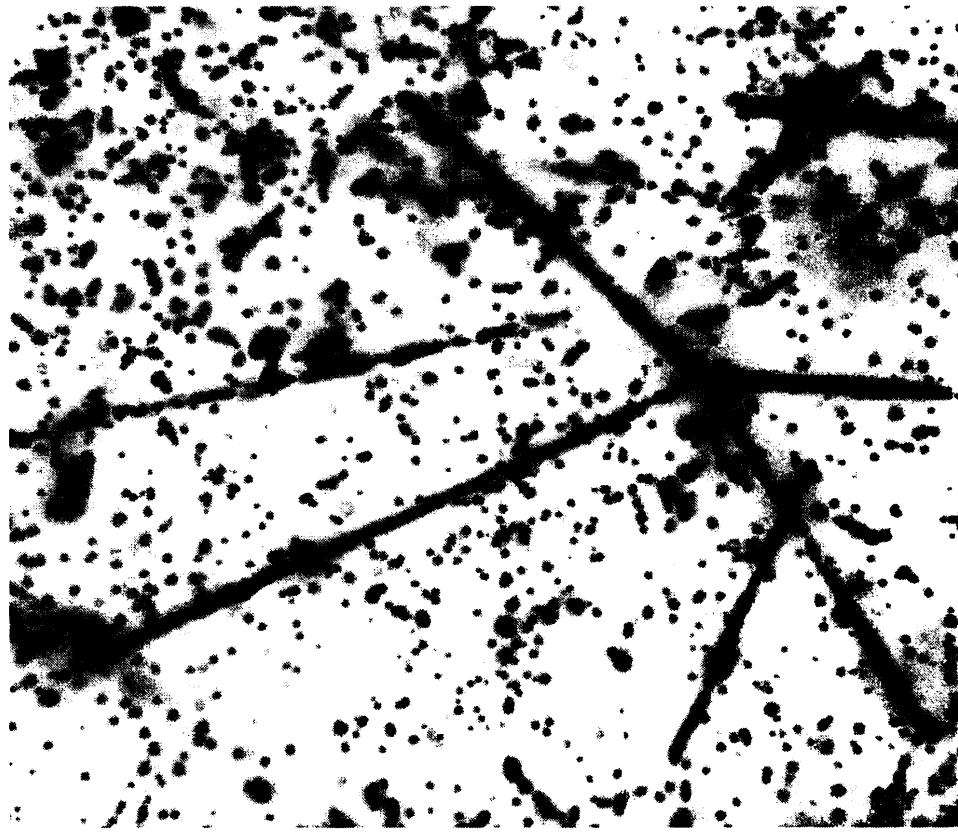

Figure 5.1: Photographic image of a ^{228}Th's decay chain. One can see four tracks emitted from one point and one isolated track.

the range of 48.4μm for the 8.785 MeV α particle or the range of 23.6μm for the 5.423 MeV α particle are 3.548 g/cm^3 or 3.543 g/cm^3. The values are in good agreement, justifying the validity of $SRIM2000$.

Plotted in Figs.5.2(b) and 5.3 are distributions for the ranges calculated using Eq.5.1 with the shrinkage factor obtained by the linear least squares fit. Only the data indicated by the black circles in Fig.5.2(a) were used for Fig.5.2(b). From these distributions, the error for the mean ranges were estimated. They are 0.26 μm for the ^{212}Po decay and 0.15 μm for the ^{228}Th decay. It is, therefore, concluded that the accuracy of the obtained range-energy relation is 0.6%. The density deduced from the measurement on the weight and volume of the emulsion plate was 3.60$\pm$0.07 g/cm^3, which is consistent within the error with the density derived from the range-energy relation.

In the same way, for mod#16-plate#7, the mean ranges of 47.7 μm for the 8.785 MeV α particle and 23.3 μm for the 5.423 MeV α particle were obtained, giving a emulsion density of 3.60$\pm$0.02 g/cm^3.

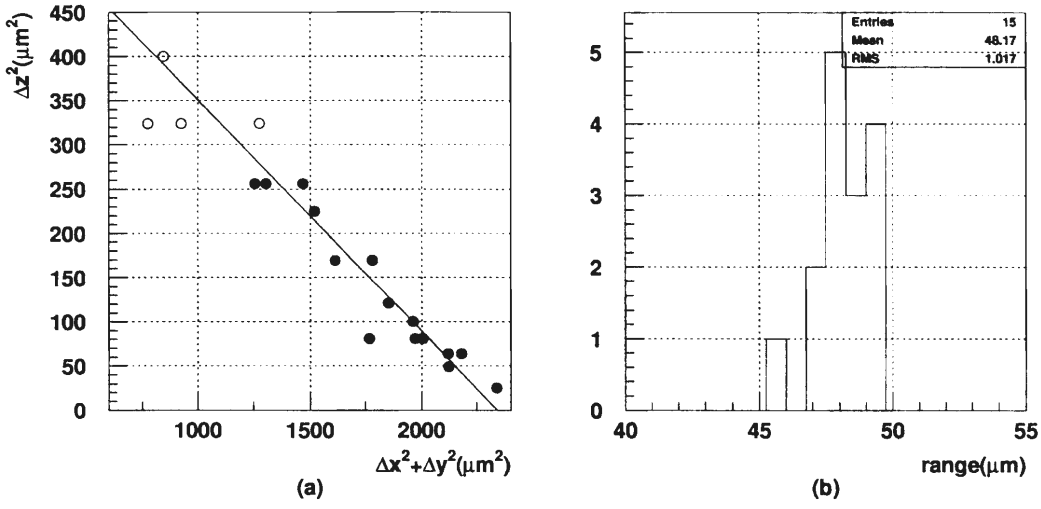

Figure 5.2: Result of the range measurement of α particles from the ^{212}Po decays. (a)Scatter plot for the measured Δz^2 versus $(\Delta x^2 + \Delta y^2)$. Here Δx, Δy and Δz are the length of the track in the x, y and z direction, respectively. (b)Distribution for the ranges calculated with the shrinkage factor obtained from (a). Only the data indicated by the black circles in (a) were used.

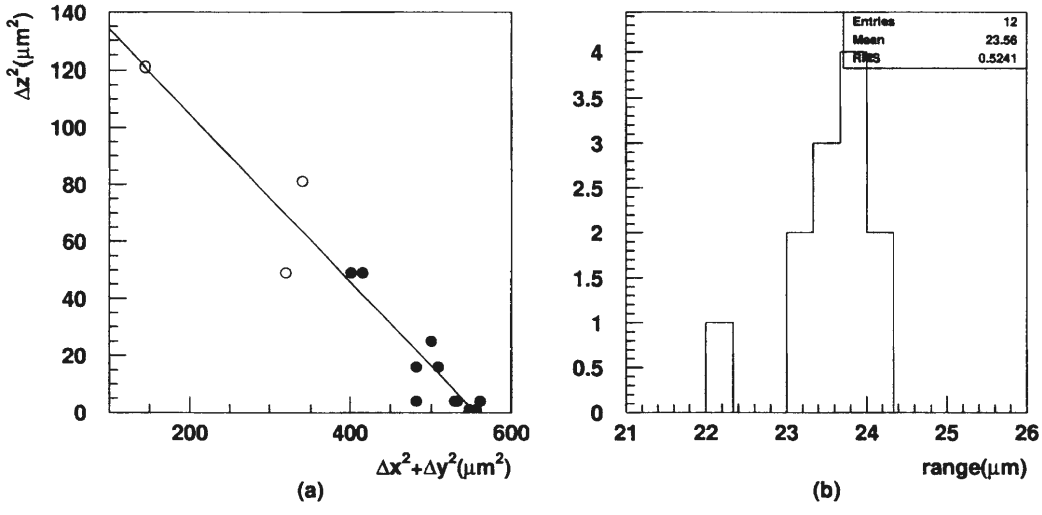

Figure 5.3: Result of the measurement of α particles from the ^{228}Th decays. The definition of figures is same as those of Fig.5.2.

5.2 Error of the measured energy

The error of the kinetic energy comes from the errors in the range measurement, the range-energy relation and range straggling. The error of the range-energy relation is 0.6% as denoted in Sec.5.1.

5.2.1 Range measurement

The length of a track is measured by pointing the track's edges on a computer display with a mouse device. By pointing a same grain several tens of time, the r.m.s error of the measurement of grain position was estimated to be 0.25μm in the direction parallel to the plate and 0.26 μm in the focusing direction. They are the origin of the error in the measurement of a track length. The position of a track in the direction perpendicular to the track can be determined more precisely by extrapolating the track. To obtain the range, the shrinkage factor must be multiplied to the length in the focusing direction. The shrinkage factor was calculated from the ratio of the thicknesses of the plate at the exposure time and at the measurement. The r.m.s error of the thickness measurement was 17 μm, giving the error of 1.7% for the shrinkage factor.

5.2.2 Range straggling

As the range straggling of proton, values from a past calculation was used[55]. For other particles, it was calculated from the value for proton using the relation[55],

$$\Delta R(T) = \Delta R_p \left(T \cdot \frac{M_p}{M} \right) \times \sqrt{\frac{M}{M_p}} \times \left(\frac{Z_p}{Z} \right)^2 \tag{5.2}$$

Here $\Delta R(T)$ is the range straggling of a particle having a mass M, a charge Z and a kinetic energy T. Those with a subscript p are the values for proton. The r.m.s error of kinetic energy due to the range straggling is less than 1.5% for proton with a momentum from 1 to 1000 MeV.

For the 8.79 MeV α particle from ^{215}Po's decay and 5.42 MeV α particle from ^{228}Th's decay, range straggling is calculated to be 0.63 μm and 0.32 μm, respectively. These are consistent with the widths of the measured distributions for the range in Figs.5.2 and 5.3 using a value of $0.25 \times \sqrt{2}$ μm for the measurement error.

Chapter 6

Twin Λ-hypernuclei event

We have found one "twin-hypernuclei" event involving the emission of two single-Λ hypernuclei and a nuclear fragment from a Ξ^- hyperon stopping point. In this chapter, details about the event and its analysis are described.

6.1 Description of the event

A Ξ^- hyperon was produced in the diamond target in conjunction with a K^+ meson of momentum 1.10 GeV/c. The reconstructed mass of the K^+ meson is 0.483 GeV/c. The Ξ^- hyperon left the diamond target and went through the fiber-bundle detector into the emulsion stack. Eight tracks were found in the most upstream emulsion plate and traced. Among them, one track shows the topology of twin single-Λ hypernuclei emission at the capture point after traversing about 5 mm in the emulsion. A large angle deflection near the capture point was observed for this track. Figure 6.1 shows the reconstructed image from SciFi-detectors. No track except for that of the outgoing K^+'s was observed in the image, meaning that no charged particle left the emulsion and went into them in this event.

Figure 6.2 shows a picture and a schematic drawing of the event. It was obtained by summing up images taken at various focusing depths of the microscope. To obtain a better position resolution a small area (15 mm$\times$15 mm) of the emulsion plate, centered on the event, was cut and swollen by water and sugar mixture to the original thickness before development. It was sliced to a tiny piece of 0.5 mm width to view from an orthogonal direction. The Ξ^- was captured by a nucleus at point A. Three charged particles (track #1, #2, #3) were emitted from point A. Track#1 shows the topology of a decay into three charged particles at point B. Track#2 also shows a topology of a decay into two charged particles at point C. Table 6.1 summarizes the ranges and the emission angles of these tracks.

The ranges were measured prior to swelling the emulsion. The effect on the measurement of the angles by any distortion introduced by swelling was checked and found to be negligible within the quoted errors. A particle (track #4) emitted from point B traveled 12.514 mm before stopping. It is identified as a π^- meson

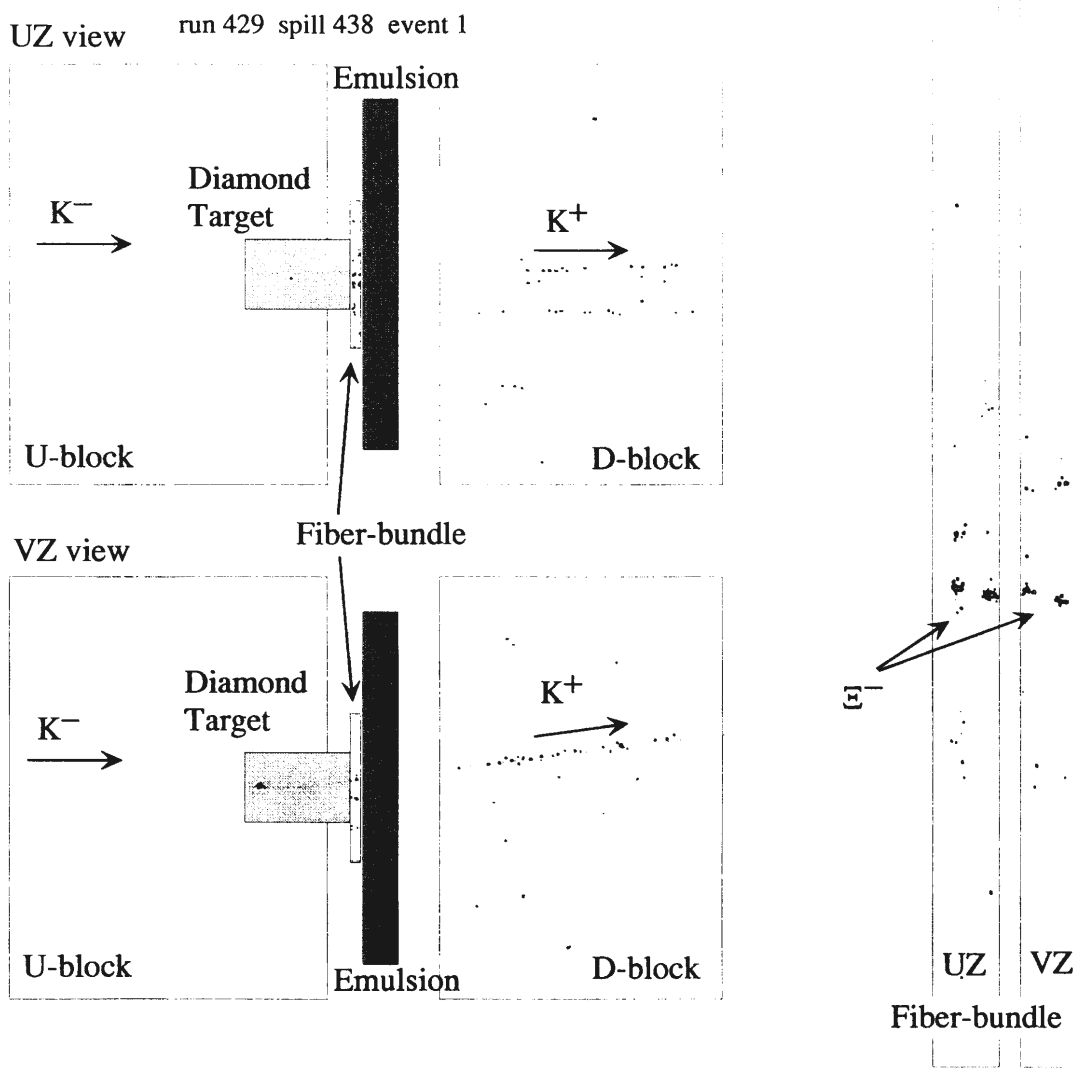

Figure 6.1: Reconstructed image obtained with the SciFi-detectors. The two figures in the right side are magnified images from Fiber-bundle. The dotted lines represent tracks of the incident K^- and outgoing K^+ obtained with the spectrometer data analysis.

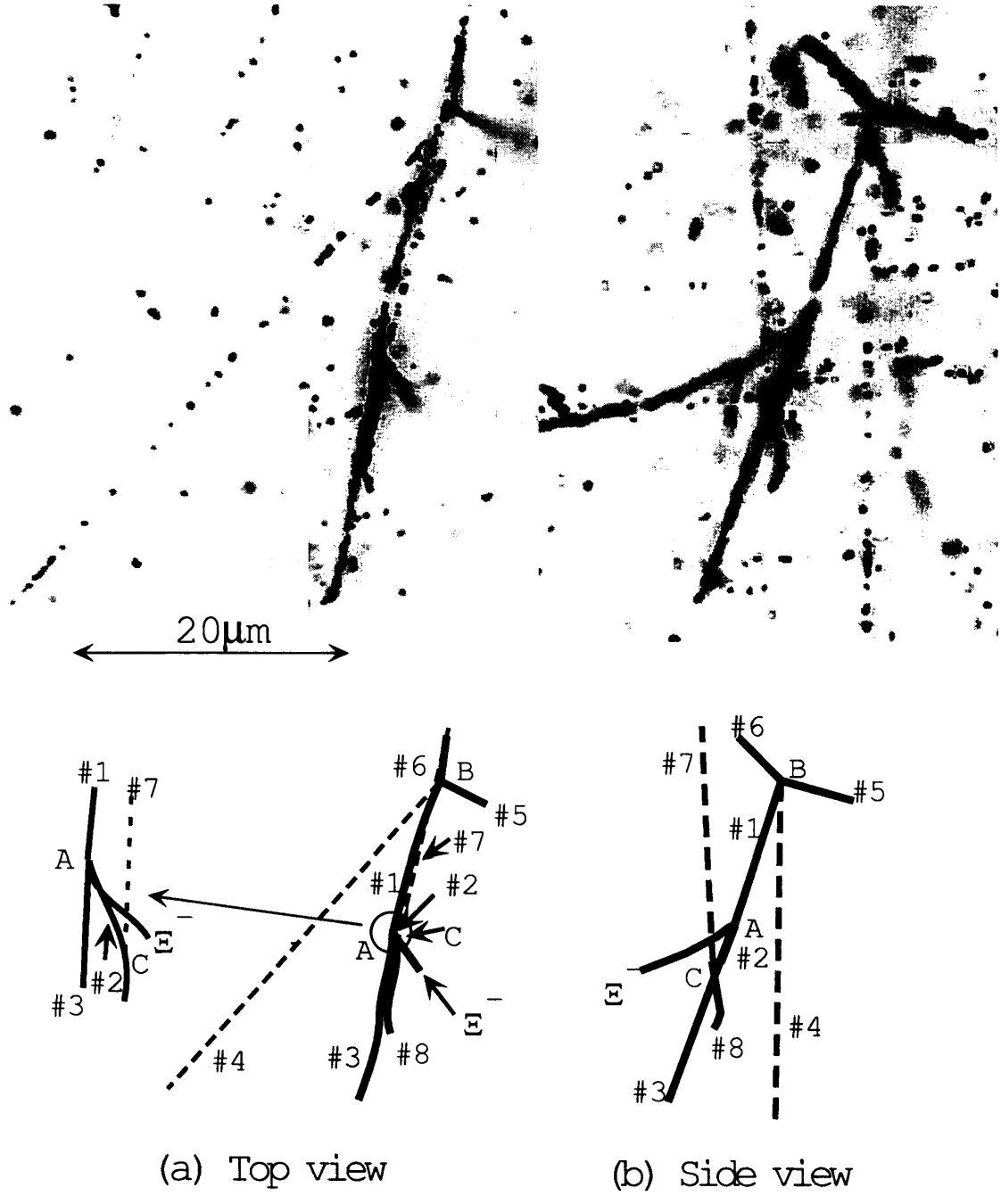

Figure 6.2: Picture and schematic drawing of the event viewed from the vertical(a) and the horizontal(b) direction. In (b), gray tracks consisting of separated grains are represented by dashed lines.

Table 6.1: Ranges and emission angles of the tracks. Angles are expressed by a zenith angle (θ) and an azimuthal angle (ϕ) in respect to the angle perpendicular to the plate. For track#4 and #7, the ranges in an acrylic base were converted to those in the emulsion.

	Track #	range (μm)	θ (degree)	ϕ (degree)	
point A	#1	19.1 ± 0.4	113 ± 7	262 ± 7	hypernucleus
	#2	5.2 ± 0.5	66 ± 7	97 ± 8	hypernucleus
	#3	23.0 ± 0.4	66 ± 3	78 ± 2	
point B	#4	12517	87.14 ± 1.2	48.19 ± 1.2	π^-(26.5 MeV)
	#5	286 ± 4	150.0 ± 1.0	153.1 ± 1.2	
	#6	7.7 ± 0.6	40 ± 4	265 ± 4	
point C	#7	≥ 14884	88 ± 1.5	257.1 ± 0.7	$p(\geq 64$ MeV)
	#8	8.8 ± 0.4	77 ± 5	81 ± 3	

from a measurement of its ionization and the observation of a track of a charged particle emitted from its stopping point. A particle (track #7) emitted from point C traversed more than 14mm and was lost at the acrylic base of the emulsion plate. The grain density of this track near point C is 1.51±0.06 times larger than that of track #4 near point B. From the ionization and the lower limit of the range, the particle of track #7 was identified as a proton.

6.2 Reconstruction of the event

As denoted in Sec.5.1, once the particle species has been assigned to a track, the kinetic energy can be calculated by means of a range-energy relation. A package "SRIM2000"[54] was used to calculate a kinetic energy from a range.

The event is interpreted as containing two single-Λ hypernuclei originating from the reaction $\Xi^- + p \rightarrow \Lambda + \Lambda$ after the Ξ^- absorption. Track #1 is a single-Λ hypernucleus which decayed mesonically at point B. Since the Q-value of the reaction is 28.2 MeV, only light hypernuclei are capable of traversing the length of track #1(19.1μm) from this energy release. Hence mesonic decay modes with three charged particles were examined for all known hypernuclei whose masses are lighter than ${}^{18}_{\Lambda}$O. For each decay modes, the total kinetic energy was calculated by assigning the particle species to each track. Listed in table 6.2 are mesonic decay modes whose Q-value is large enough to account for the sum of the kinetic energies of charged decay products (E_{visi}). For the decay modes with no neutron, the momentum sum of three charged particles (p_{sum}) must be zero within the error. For the modes with a neutron, the kinetic energy of the neutron was calculated using momentum balance for the charged particles. The total kinetic energy of charged particles and a neutron (E_{total}) was compared with the Q-value. Only ${}^{5}_{\Lambda}$He and ${}^{6}_{\Lambda}$He were found to be acceptable for track #1 candidates. The particle of track #2 decayed in a non-mesonic mode and its species cannot be

Table 6.2: Decay modes for track #1 whose Q-value is large enough compared to the visible energy(E_{visi}). Here E_{visi} and p_{sum} are the sum of the kinetic energy and momenta of three charged particles, respectively. E_{total} is the total kinetic energy of decay particles.

Decay mode	Q (MeV)	E_{visi} (MeV)	p_{sum} (MeV/c)	E_{total}	
${}^{3}_{\Lambda}\mathrm{H} \to \pi^- + p + p + n$	35.49	33.8±0.5	95.6±2.2	38.6±0.7	rejected
${}^{3}_{\Lambda}\mathrm{H} \to \pi^- + p + d$	37.71	33.9±0.5	76.7±2.7	33.9±0.5	rejected
${}^{3}_{\Lambda}\mathrm{H} \to \pi^- + d + p$	37.71	35.8±0.5	152.8±2.5	35.8±0.5	rejected
${}^{4}_{\Lambda}\mathrm{H} \to \pi^- + p + t$	35.80	34.0±0.5	67.8±3.2	34.0±0.5	rejected
${}^{4}_{\Lambda}\mathrm{He} \to \pi^- + p + {}^{3}\mathrm{He}$	35.45	35.3±0.5	23.0±5.0	35.3±0.5	rejected
${}^{5}_{\Lambda}\mathrm{He} \to \pi^- + p + {}^{4}\mathrm{He}$	34.72	35.4±0.5	13.0±8.7	35.4±0.5	acceptable
${}^{6}_{\Lambda}\mathrm{He} \to \pi^- + p + {}^{4}\mathrm{He} + n$	34.56	35.4±0.5	13.0±8.7	35.5 ±0.6	acceptable
${}^{6}_{\Lambda}\mathrm{He} \to \pi^- + d + {}^{4}\mathrm{He}$	36.78	37.5±0.5	63.1±6.0	37.5±0.5	rejected
${}^{8}_{\Lambda}\mathrm{He} \to \pi^- + t + {}^{4}\mathrm{He} + n$	38.64	39.0±0.5	120.9±6.0	46.7±1.3	rejected

assigned from its decay topology.

We assert that the Ξ^- hyperon was absorbed by a light nucleus (^{12}C (, ^{13}C), ^{14}N or ^{16}O) in the emulsion for the following reasons. The kinetic energy of the track #1 particle is 5.0 MeV or 5.2 MeV in the case of ${}^{5}_{\Lambda}$He or ${}^{6}_{\Lambda}$He, respectively. With these values they are very unlikely to escape through the Coulomb barrier of a Ag or Br nucleus. This is true even if the hypernucleus of track#1 is lighter than ${}^{5}_{\Lambda}$He. Furthermore the absence of Auger electrons also supports this.

Table 6.3 summarizes the decay modes from $\Xi^- + {}^{12}\mathrm{C}/{}^{13}\mathrm{C}/{}^{14}\mathrm{N}/{}^{16}\mathrm{O}$ to two hypernuclei and a non-strange nucleus. For each of these modes, the total kinetic energy of three nuclei was calculated from the measured ranges and was compared with the Q-value. Only two decay modes,

$$\Xi^- + {}^{14}\mathrm{N} \rightarrow {}^{5}_{\Lambda}\mathrm{He} + {}^{5}_{\Lambda}\mathrm{He} + {}^{4}\mathrm{He} + n,$$
$$\Xi^- + {}^{14}\mathrm{N} \rightarrow {}^{5}_{\Lambda}\mathrm{He} + {}^{6}_{\Lambda}\mathrm{He} + {}^{4}\mathrm{He},$$

have Q-values either larger than or equal within errors (three standard deviations) to the calculated total kinetic energy. Again, only ${}^{5}_{\Lambda}$He or ${}^{6}_{\Lambda}$He is acceptable as the hypernucleus for track #1. It should be noted that neither ${}^{5}_{\Lambda}$He nor ${}^{6}_{\Lambda}$He has any excited states which can decay via gamma emission. Therefore, there is no uncertainty arising from excited states. For each of these three modes, the total momentum of the three nuclei was calculated. The results are summarized in table 6.4. For the modes $\Xi^- + {}^{14}\mathrm{N} \to {}^{5}_{\Lambda}\mathrm{He}(\#1) + {}^{6}_{\Lambda}\mathrm{He}(\#2) + {}^{4}\mathrm{He}(\#3)$ and $\Xi^- + {}^{14}\mathrm{N} \to {}^{6}_{\Lambda}\mathrm{He}(\#1) + {}^{5}_{\Lambda}\mathrm{He}(\#2) + {}^{4}\mathrm{He}(\#3)$, the sum of the momenta of the three nuclei deviates from zero by 10 and 6 standard deviations respectively.

We conclude, therefore, that this event can be assigned as

$$\Xi^- + {}^{14}\mathrm{N} \rightarrow {}^{5}_{\Lambda}\mathrm{He}(\#1) + {}^{5}_{\Lambda}\mathrm{He}(\#2) + {}^{4}\mathrm{He}(\#3) + n.$$

The binding energy of the Ξ^- is then calculated to be -2.6 ± 1.2 MeV. Here the quoted error is one standard deviation. The negative binding energy would correspond to an unbound state, however within the error bar it is certainly

Table 6.3: Decay modes for Ξ^-+^{12}C/^{13}C/^{14}N/^{16}O in which two hypernuclei and a nucleus are emitted. Minimal total kinetic energy is obtained as 3.5 MeV assuming the decay particles as ${}^{4}_{\Lambda}$H (#1), ${}^{4}_{\Lambda}$H (#2) and p(#3). For each of the modes whose Q-value exceeds 3.5 MeV, minimal total kinetic energy of the mode is calculated as the sum of the kinetic energy of three charged particles assuming the track #1 particle as the lighter Λ-hypernucleus of the mode. The value is quoted on the 4th column. Comment "rejected" on the 5th column means that the minimal total kinetic energy of the mode exceeds the Q-value.

Target nucleus	Decay mode	Q (MeV)	E_{min} (MeV)	
^{12}C	${}^{4}_{\Lambda}$H+${}^{5}_{\Lambda}$He+^{4}He	6.30	8.79±0.20	rejected
	${}^{5}_{\Lambda}$He+${}^{5}_{\Lambda}$He+$d+n$	1.12		rejected
	${}^{5}_{\Lambda}$He+${}^{5}_{\Lambda}$He+t	7.38	8.53±0.20	rejected
	${}^{5}_{\Lambda}$He+${}^{6}_{\Lambda}$He+d	1.28		rejected
^{13}C	${}^{4}_{\Lambda}$H+${}^{5}_{\Lambda}$He+^{4}He+n	1.35		rejected
	${}^{4}_{\Lambda}$H+${}^{6}_{\Lambda}$He+^{4}He	1.51		rejected
	${}^{5}_{\Lambda}$He+${}^{5}_{\Lambda}$He+$t+n$	2.43		rejected
	${}^{5}_{\Lambda}$He+${}^{6}_{\Lambda}$He+t	2.59		rejected
^{14}N	${}^{3}_{\Lambda}$H+${}^{8}_{\Lambda}$Li+^{4}He	0.27		rejected
	${}^{4}_{\Lambda}$H+${}^{10}_{\Lambda}$Be+p	1.37		rejected
	${}^{5}_{\Lambda}$He+${}^{5}_{\Lambda}$He+^{4}He+n	14.69	8.53±0.20	
	${}^{5}_{\Lambda}$He+${}^{6}_{\Lambda}$He+^{4}He	14.86	11.83±0.23	
	${}^{5}_{\Lambda}$He+${}^{7}_{\Lambda}$Li+t	1.04		rejected
	${}^{5}_{\Lambda}$He+${}^{8}_{\Lambda}$Li+$p+n$	1.03		rejected
	${}^{5}_{\Lambda}$He+${}^{8}_{\Lambda}$Li+d	3.26		rejected
	${}^{5}_{\Lambda}$He+${}^{9}_{\Lambda}$Li+p	4.76	8.62±0.31	rejected
	${}^{6}_{\Lambda}$He+${}^{8}_{\Lambda}$Li+p	1.19		rejected
^{16}O	${}^{4}_{\Lambda}$H+${}^{9}_{\Lambda}$Be+^{4}He	2.64		rejected
	${}^{5}_{\Lambda}$He+${}^{5}_{\Lambda}$He+^{7}Li	2.69		rejected
	${}^{5}_{\Lambda}$He+${}^{8}_{\Lambda}$Li+^{4}He	6.37	12.65±0.33	rejected
	${}^{5}_{\Lambda}$He+${}^{9}_{\Lambda}$Be+t	3.72		rejected
	${}^{5}_{\Lambda}$He+${}^{10}_{\Lambda}$Be+d	3.72		rejected

Table 6.4: Decay modes to two hypernuclei (track #1 and #2) and one nucleus (track #3) whose Q-value is larger than or equal to the visible energy (E_{visi}). Here E_{visi} and p_{sum} are the sum of the kinetic energy and momenta of three nuclei, respectively. E_{total} is the total kinetic energy of decay particles.

Target nucleus	track #1	#2	#3	# of neutrons	Q (MeV)	E_{visi} (MeV)	p_{sum} (MeV/c)	E_{total} (MeV)
^{12}C	${}^{5}_{\Lambda}$He	${}^{5}_{\Lambda}$He	t	0	7.38	7.84±0.25	30±33	7.84±0.25
^{14}N	${}^{5}_{\Lambda}$He	${}^{5}_{\Lambda}$He	^{4}He	1	14.70	11.89±0.21	101±9.8	17.3±1.2
^{14}N	${}^{5}_{\Lambda}$He	${}^{6}_{\Lambda}$He	^{4}He	0	14.86	11.85±0.21	111±11	11.85±0.21
^{14}N	${}^{6}_{\Lambda}$He	${}^{5}_{\Lambda}$He	^{4}He	0	14.86	12.08±0.21	76±12	12.08±0.21

consistent with a capture from an atomic, i.e. bound level. The species of the Ξ^--atom and the fragmentation products are uniquely identified for the first time for twin-hypernuclei events.

Chapter 7

Double-Λ hypernucleus event

Sequential weak decay of a double-Λ hypernucleus was found at the stopping point of a Ξ^- hyperon. In this chapter, details about the event and its analysis are described. The result is compared with past experimental results and theoretical calculations.

7.1 Description of the event

A Ξ^- hyperon was produced in the diamond target in conjunction with a K^+ meson of momentum 1.14 GeV/c. The reconstructed mass of the K^+ meson is 0.501 GeV/c^2. The Ξ^- hyperon left the diamond target and went through the fiber-bundle detector into the emulsion stack. Two tracks were found in the most upstream emulsion plate and traced. Among them, one track shows the topology of a production and sequential weak decay of a double-Λ hypernucleus after traversing about 7 mm in the emulsion. A large angle deflection near the capture point was observed for this track. Figure 7.1 shows the reconstructed image from SciFi-detectors. No track except for the outgoing K^+ was observed in the image, meaning that no charged particle left the emulsion and went into them in this event.

Figure 7.2 shows a picture and a schematic drawing of the event. It was obtained by summing up images taken at various focusing depths of the microscope. Figure 7.3 shows photographs of the event at various focusing position.

To obtain a better position resolution, a small area of the emulsion plate, centered on the event, was cut and swollen to the original thickness before development, and was sliced to a tiny piece of 0.5 mm width in the same manner as the twin-hypernuclei event. The Ξ^- was captured by a nucleus at point A. Two charged particles (track #1, #2) were emitted from point A. The two tracks are collinear within the measurement error. Track#2 shows the topology of a decay into one charged particle(track #3) (and neutral particles) at point B. Track #3 shows the topology of a decay into two or three charged particles (#4,#5,(#6)) at point C. Because the width of the first half of track #5 is rather thick, there may exist one more track parallel to track #5. This possible track was assigned

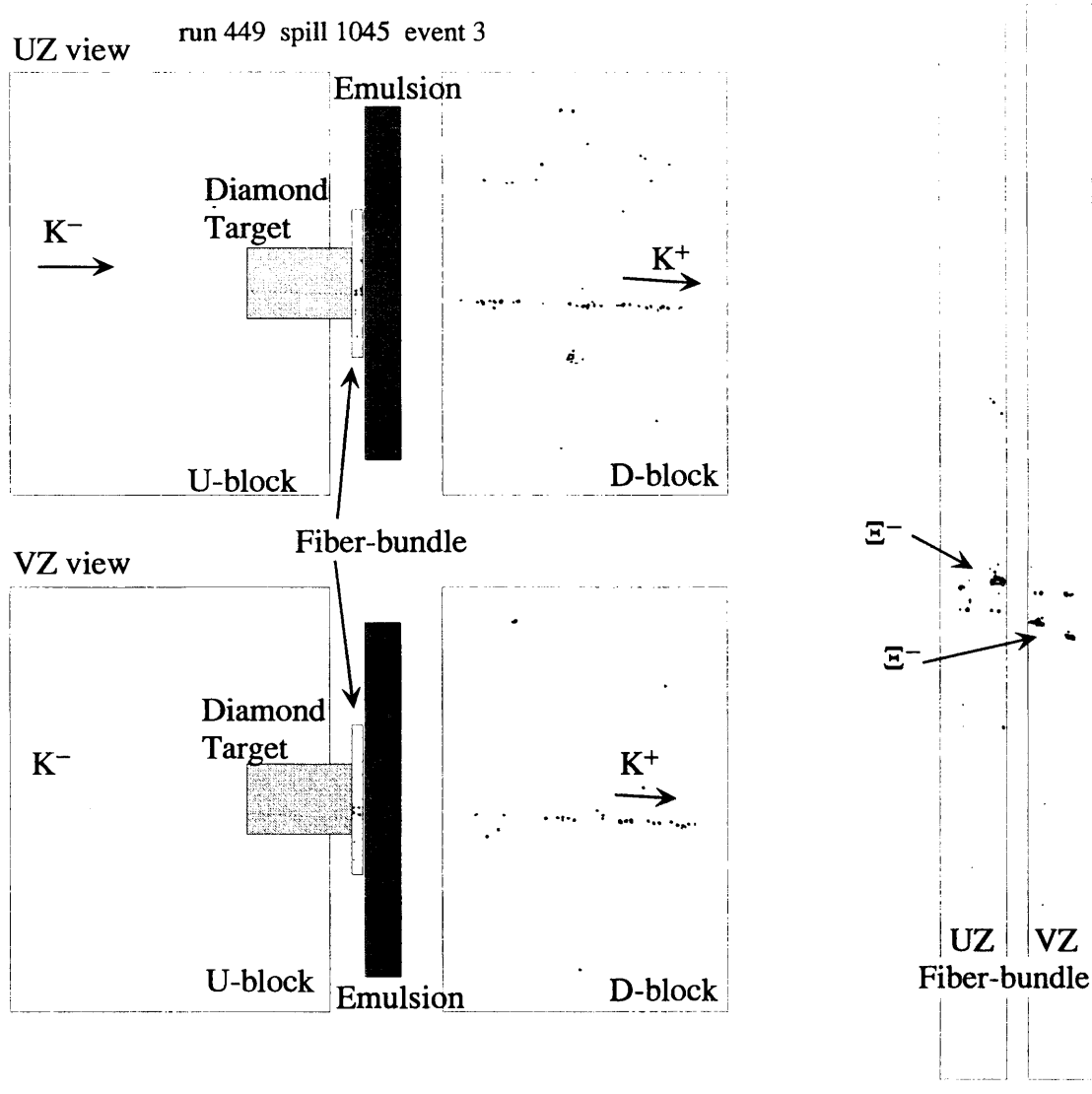

Figure 7.1: Reconstructed image obtained with the SciFi-detectors. The two figures in the right side are magnified images from Fiber-bundle. The dotted lines represent tracks of the incident K^- and outgoing K^+ obtained with the spectrometer data analysis.

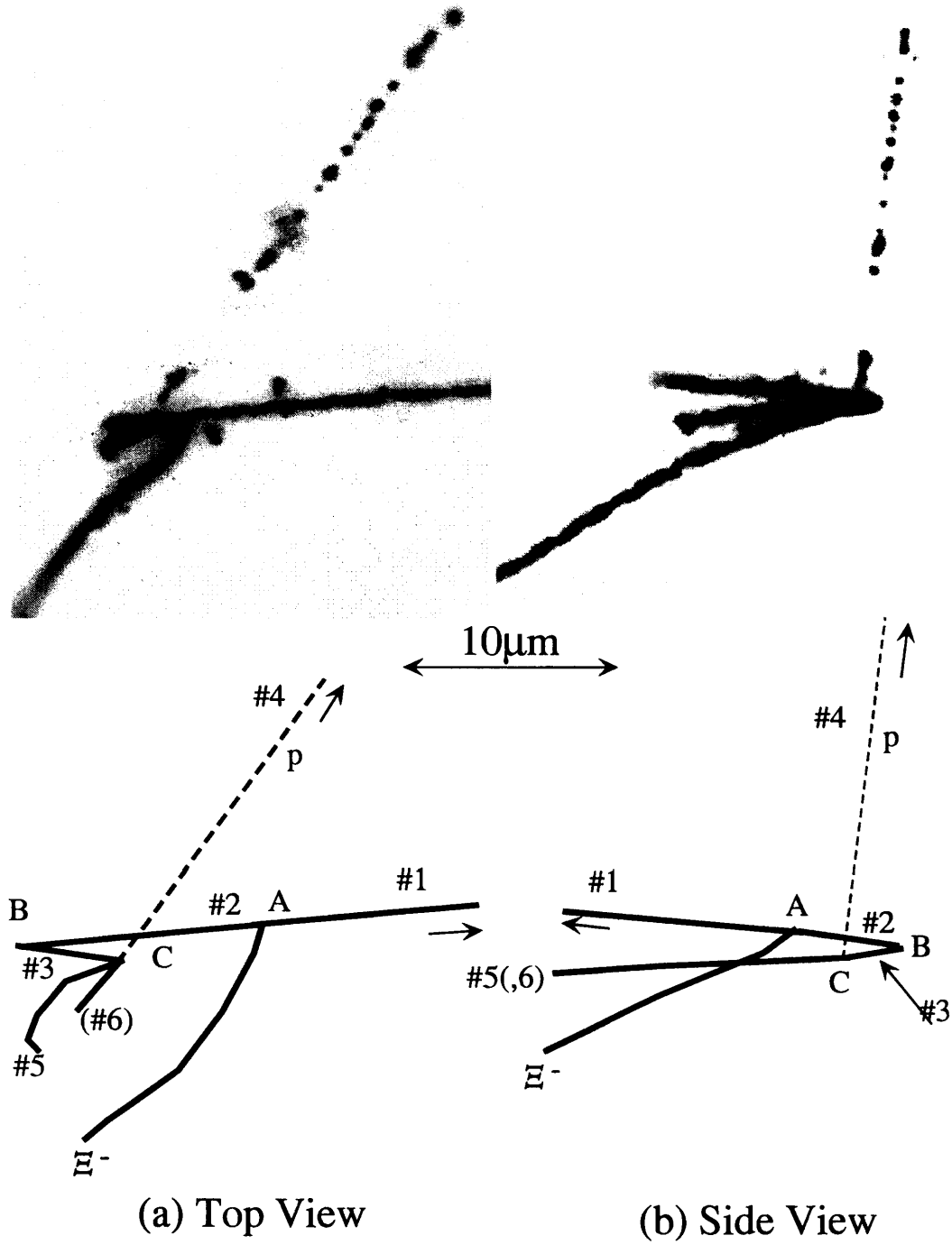

Figure 7.2: Picture and schematic drawing of the event viewed from the vertical(a) and the horizontal(b) direction.

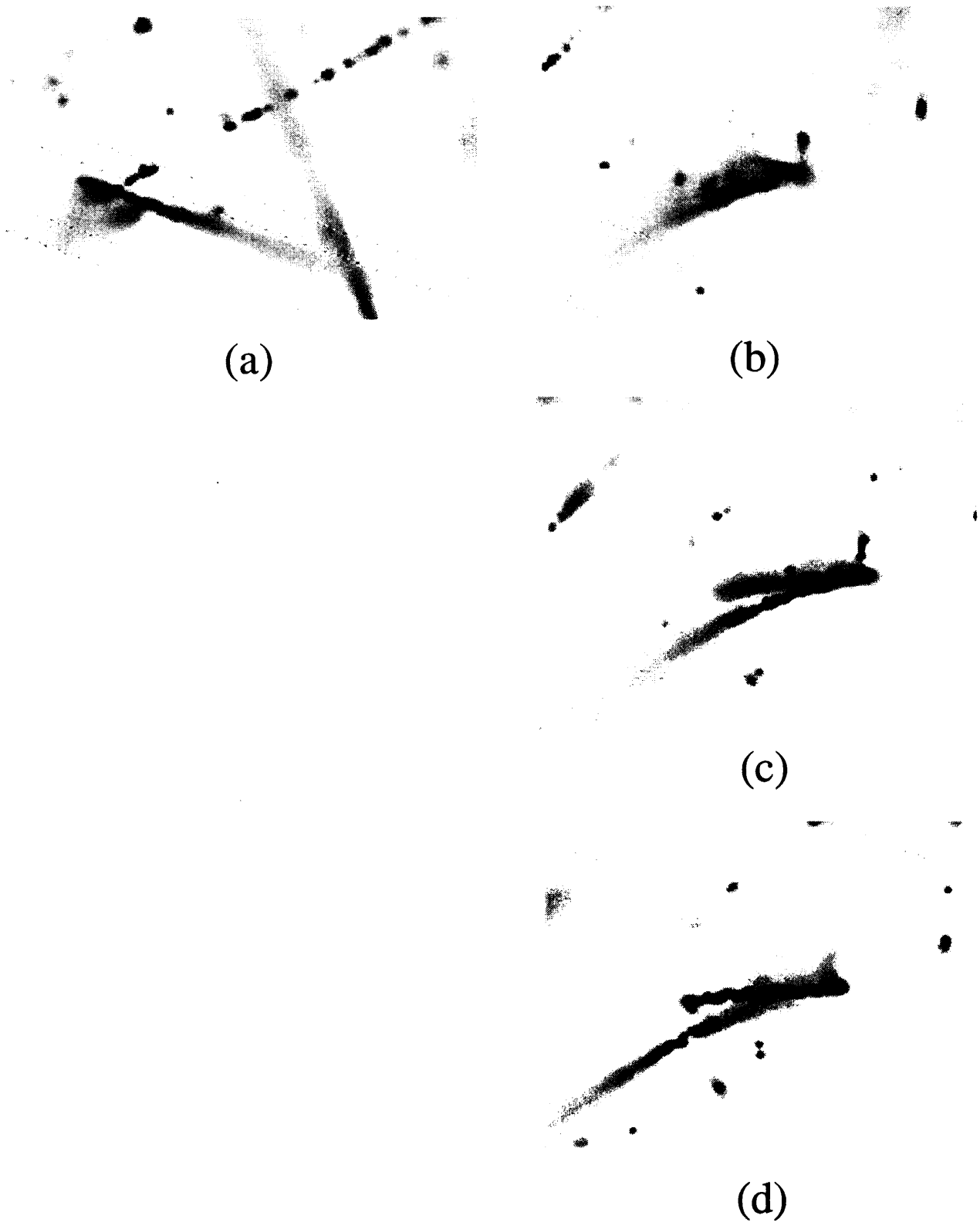

Figure 7.3: Photographs of the event viewed from the vertical direction ((a)) and a horizontal direction ((b),(c) and (d)). (a) The Ξ^- capture point and the track of the double-Λ hypernucleus are in focus. (b) The Ξ^- capture point is in focus. (c) The track of the double-Λ hypernucleus is in focus. (d) The track of the daughter single-Λ hypernucleus and it's decay product (#5) are in focus.

Table 7.1: Ranges and emission angles of the tracks. Angles are expressed by a zenith angle (θ) and an azimuthal angle (ϕ) in respect to the angle perpendicular to the plate. For track#4, the range in an acrylic base was converted to that in the emulsion. Track #6 is a possible track whose existence was not well identified.

	Track #	range (μm)	θ (degree)	ϕ (degree)	
point A	#1	287.0 ± 1.9	57.7 ± 1.1	159.38 ± 0.48	
	#2	$4.2^{+0.25}_{-0.07}$	124.5 ± 5.1	343.2 ± 3.5	double-Λ hyp.
point B	#3	$3.7^{+0.3}_{-0.1}$	32.6 ± 7.8	145 ± 10	
point C	#4	23575	94.17 ± 0.40	209.83 ± 0.25	$p(> 84$ MeV)
	#5	11.3 ± 0.7	9.4 ± 3.4	341 ± 20	
	(#6	8.4 ± 0.7	7.2 ± 2.5	21 ± 19)	

as #6. Table 7.1 summarizes the ranges and the emission angles of these tracks. The ranges were measured prior to swelling the emulsion. The effect on the measurement of the angles by any distortion introduced by swelling was checked and found to be negligible within the quoted errors. Because the range of track #2 is very important, it was measured several times by three people and the most probable value and an upper-limit and lower-limit was determined. The quoted r.m.s error was determined from the upper- and lower-limit. The reason why the error in the (+) direction is larger than that in the (-) direction is because the Ξ^- particle seems to have turned to the (+) direction before stopping and the stopping point has larger uncertainty in the (+) direction. A particle (track #4) emitted from point C traveled 23575 μm before stopping. It is identified as a proton from a measurement of its ionization and the range.

7.2 Reconstruction of the event

Again, once the particle species has been assigned to a track, the kinetic energy can be calculated by means of a range-energy relation using the package *SRIM*2000.

A possible interpretation of the event other than the production and sequential decay of a double-Λ hypernucleus is a production and scattering of a single-Λ hypernucleus on an Ag or Br nucleus. Due to the Coulomb barrier, only the Rutherford scattering was possible. However, the probability to occur a backward-scattering in 5 μm in emulsion was calculated to be less than 1×10^{-4}, which is negligible considering the production rate of single-Λ hypernuclei and double-Λ hypernuclei. Therefore the event is interpreted as containing a double-Λ hypernucleus originating from the reaction $\Xi^- + p \rightarrow \Lambda + \Lambda$ after the Ξ^- absorption. We assert that the Ξ^- hyperon was absorbed by a light nucleus (^{12}C, ^{14}N or ^{16}O) in the emulsion because a track of a short range of 4.2 μm exists. The energy of this particle is insufficient to surmount the Coulomb barrier of the heavy emulsion nuclei (Ag, Br). The absence of Auger electrons also supports

this.

Because track#1 and track#2 is collinear within the error, we first consider the case of a two-body decay from the Ξ^- capture. By assuming the nuclide of the target nucleus (^{12}C, ^{14}N or ^{16}O) and that of track #1 particle ($p, d, t, ^3$He, ^{4}He, etc), the nuclide of the double-Λ hypernucleus is determined uniquely for each assumption. From the energy conservation, there is a relation,

$$M_{\Xi^-} + M_{target} - B_{\Xi^-} = M_1 + M_2 + T_1 + T_2, \tag{7.1}$$

where $M_{\Xi^-}, M_{target}, M_1, M_2$ are masses of the Ξ^- hyperon, target nucleus and the track#1 and track#2 particles, respectively. The B_{Ξ^-} is a binding energy of the Ξ^- hyperon when the capture and fragmentation occurred. The T_1 and T_2 are the kinetic energies for the track#1 and track#2 particles, respectively. From the momentum conservation, the momentum of track#2 particle is same as that of the track#1 particle. Hence,

$$M_2 + T_2 = \sqrt{M_2^2 + p^2}, \tag{7.2}$$

where p is a momentum of track#1 particle. From Eqs.7.1 and 7.2, the mass of the double-Λ hypernucleus are determined as,

$$M_2 = \sqrt{(M_{\Xi^-} + M_{target} - B_{\Xi^-} - M_1 - T_1)^2 - p^2}. \tag{7.3}$$

The kinetic energy T_2 is determined from M_2 using Eq.7.1. Actually, T_2 is almost independent of B_{Ξ^-} if B_{Ξ^-} is very small compared to M_2, which is true even if the Ξ^- was absorbed from the Ξ^--nuclear state. The double-Λ hypernucleus might be produced in an excited state and emit a γ-ray immediately after the production. In that case, only the mass of the ground state double-Λ hypernucleus differs from M_2 obtained with Eq.7.3, but the kinetic energy is almost same as T_2 because the γ can carry out only a small momentum.

Possible two-body reactions following the Ξ^- capture at rest to form a double-Λ hypernucleus and one charged particle having a range of track#1 are listed in Table 7.2. The mass of the possible double-Λ hypernucleus was calculated assuming that the double-Λ hypernucleus was produced in the ground state and that $B_{\Xi^-} = 0$. The binding energy ($B_{\Lambda\Lambda}$) and interaction energy ($\Delta B_{\Lambda\Lambda}$) of $\Lambda\Lambda$ defined as Eq.1.6 are calculated from the mass. From the comparison of the range of the double-Λ hypernucleus calculated from the kinetic energy obtained with Eq.7.3 with that measured in the emulsion, some of the reactions in Table 7.2 can be rejected. However the range-energy relation for multiply-charged particles at very low energy is not well known. Ziegler *et al.* estimated that the accuracy of the calculation by *SRIM*2000 for the ion ranges in silicon is 9%[56]. Heckman *et al.* measured the range-energy relation for C, N, O, Ne and Ar ions in emulsion [57]. The measured range for 4.0 MeV ^{12}C deviates from the calculation by *SRIM*2000 by 9%. Therefore, the following condition was applied,

$$(r - 3 \times \sigma_r^{(-)}) \times 0.9 < \textit{calculated range} < (r + 3 \times \sigma_r^{(+)}) \times 1.1,$$

Table 7.2: Possible reactions following the Ξ^- capture at rest to form a double-Λ hypernucleus and one charged particle having a range of track#1. The $B_{\Lambda\Lambda}$ and $\Delta B_{\Lambda\Lambda}$ were calculated from the mass of the double-Λ hypernucleus assuming that the double-Λ hypernucleus was produced in the ground state and the binding energy of Ξ^- (B_{Ξ^-}) was zero. The $\Delta B_{\Lambda\Lambda}$ is not quoted if the binding energy of the corresponding single-Λ hypernucleus is not known. The T_2 is the kinetic energy of the double-Λ hypernucleus. The expected range is a calculated range from T_2 using the range-energy relation. The reactions in which the expected range exceeds 10 μm are not listed. The quoted errors for $B_{\Lambda\Lambda}$ do not include the error originated from the uncertainty of the mass of the Ξ^- hyperon (0.13 MeV).

Target	#1	#2	$B_{\Lambda\Lambda}$	$\Delta B_{\Lambda\Lambda}$	T_2 (MeV)	expected range(μm)	
^{12}C	p	$^{12}_{\Lambda\Lambda}$Be	6.19±0.09	-	0.545±0.007	1.57	rejected
	d	$^{11}_{\Lambda\Lambda}$Be	13.89±0.11	−4.33	1.556±0.016	3.00	rejected
	t	$^{10}_{\Lambda\Lambda}$Be	12.21±0.12	−1.21	2.986±0.028	4.59	
^{14}N	p	$^{14}_{\Lambda\Lambda}$B	4.01±0.09	−19.99	0.469±0.006	1.06	rejected
	d	$^{13}_{\Lambda\Lambda}$B	8.11±0.10	−14.63	1.324±0.014	2.12	rejected
	t	$^{12}_{\Lambda\Lambda}$B	15.97±0.12	−4.51	2.503±0.024	3.19	rejected
	^{3}He	$^{12}_{\Lambda\Lambda}$Be	33.32±0.25	-	5.815±0.050	8.15	rejected
^{16}O	p	$^{16}_{\Lambda\Lambda}$C	1.21±0.09	-	0.412±0.005	0.85	rejected
	d	$^{15}_{\Lambda\Lambda}$C	10.00±0.10	−14.34	1.152±0.012	1.71	rejected
	t	$^{14}_{\Lambda\Lambda}$C	11.17±0.12	−12.21	2.157±0.020	2.48	rejected
	^{3}He	$^{14}_{\Lambda\Lambda}$B	40.87±0.25	-	5.009±0.043	5.64	rejected
	^{4}He	$^{13}_{\Lambda\Lambda}$B	29.53±0.29	6.79	7.999±0.066	8.23	rejected

where r is the measured range of the double-Λ hypernucleus and $\sigma_r^{(+)}$ and $\sigma_r^{(-)}$ are its errors including the effect of range straggling ($\sim$ 0.05 μm). Only one double-Λ hypernucleus, $^{10}_{\Lambda\Lambda}$Be was found to be acceptable.

The r.m.s error for $B_{\Lambda\Lambda}$ and $\Delta B_{\Lambda\Lambda}$ due to the error in the measurement (0.12 MeV) and the uncertainties of the mass of the Ξ^- hyperon (0.13 MeV) and $^9_\Lambda$Be nucleus (!!! MeV) was calculated to be 0.18 MeV. As for the binding energy of the Ξ^- hyperon (B_{Ξ^-}), Batty *et al.* calculated nuclear absorption rate of Ξ^- for various atomic states[58]. According to their results, the most likely capture in ^{12}C occurs from the atomic $3D$ state whose binding energy is 0.126 MeV. The capture probabilities from the neighboring states ($2P$ at 0.28 MeV and $4F$ at 0.07 MeV) are about one order of magnitude smaller than that from the $3D$ state. We, therefore, set a value of $0.1^{+0.1}_{-0.05}$ MeV for B_{Ξ^-}.

The ^{8}Be nucleus has an excited state at 3.04 MeV. Since the corresponding levels of the $^9_\Lambda$Be's doublet states (3.03 MeV and 3.06 MeV[59]) are almost unchanged from that of the core nucleus, the corresponding level of the $^{10}_{\Lambda\Lambda}$Be nucleus is also expected to be close to 3.04 MeV. If the $^{10}_{\Lambda\Lambda}$Be nucleus was produced in the excited state at 3.0 MeV, then the binding energy and interaction energy of ΛΛ are increased by 3.0 MeV from the value quoted in Table 7.2. Higher states

Table 7.3: Possible reactions following the Ξ^- capture at rest to form a double-Λ hypernucleus, one charged particle and a neutron. The $\Delta B_{\Lambda\Lambda}$) were calculated from the mass of the double-Λ hypernucleus. Only the interpretations which give a $\Delta B_{\Lambda\Lambda}$ smaller than 20 MeV are listed. The "meas.error" and "sys.error" represent the error due to the measurement and the error due to the uncertainty (10%) of the range-energy measurement at very low energy, respectively.

Target	#1	#2	$\Delta B_{\Lambda\Lambda}$ (MeV)	meas.error	sys.error
^{12}C	p	$^{11}_{\Lambda\Lambda}$Be	4.52	$^{+1.50}_{-0.47}$	$^{+2.48}_{-2.36}$
	d	$^{10}_{\Lambda\Lambda}$Be	4.39	$^{+0.78}_{-0.23}$	$^{+1.18}_{-0.98}$
	t	$^{9}_{\Lambda\Lambda}$Be	17.56	$^{+0.48}_{-0.10}$	$^{+0.16}_{-0.08}$
^{14}N	p	$^{13}_{\Lambda\Lambda}$B	5.53	$^{+2.64}_{-0.83}$	$^{+4.30}_{-4.08}$
	d	$^{12}_{\Lambda\Lambda}$B	7.54	$^{+1.66}_{-0.50}$	$^{+2.69}_{-2.46}$
	t	$^{11}_{\Lambda\Lambda}$B	8.84	$^{+0.99}_{-0.27}$	$^{+1.34}_{-1.07}$
^{16}O	p	$^{15}_{\Lambda\Lambda}$C	19.94	$^{+3.94}_{-1.28}$	$^{+6.52}_{-6.36}$
	d	$^{14}_{\Lambda\Lambda}$C	9.48	$^{+2.88}_{-0.90}$	$^{+4.71}_{-4.31}$
	t	$^{13}_{\Lambda\Lambda}$C	16.11	$^{+1.95}_{-0.59}$	$^{+3.04}_{-2.66}$

of the $^{10}_{\Lambda\Lambda}$Be nucleus are unstable against particle decay.

We conclude that if a two-body decay from the Ξ^- capture is assumed, the event is uniquely identified as,

$$\Xi^- + ^{12}\mathrm{C} \rightarrow ^{10}_{\Lambda\Lambda}\mathrm{Be} + t.$$

The binding energy and interaction energy of $\Lambda\Lambda$ are 12.31±0.21 MeV and −1.11± 0.21 MeV, respectively if it was produced in the ground state. If it was produced in the excited state at 3.0 MeV, then the binding energy and interaction energy are 15.35±0.21 MeV and 1.93±0.21 MeV, respectively.

If the fragmentation from the Ξ^- absorption was three-body including a neutron emission, the momentum of the neutron can be calculated for each assignment of the reaction from the the sum of the momenta of the residual nucleus (track #1) and the double-Λ hypernucleus (track #2), both of which were calculated using the range-energy relation. The mass of the double-Λ hypernucleus was determined so that the Q-value of the fragmentation reaction becomes equal to the kinetic energy of the three fragmentation products. Possible interpretations are listed in Table 7.3 with the calculated $\Delta B_{\Lambda\Lambda}$ values assuming that the double-Λ hypernucleus was produced in the ground state and that B_{Ξ^-} is zero. Only the interpretations which give a $\Delta B_{\Lambda\Lambda}$ smaller than 20 MeV are listed. The main origin of the error for $\Delta B_{\Lambda\Lambda}$ is the uncertainty of the range-energy relation. The uncertainty due to B_{Ξ^-} is small compared to other errors. Taking 10% as the maximum deviation from the calculation by $SRIM2000$, the lowest value of $\Delta B_{\Lambda\Lambda}$ in the three-body fragmentation case was obtained as $1.45^{+2.2}_{-0.59}$ MeV for the reaction $\Xi^- + ^{14}\mathrm{N} \rightarrow ^{13}_{\Lambda\Lambda}\mathrm{B} + p + n$. This lower limit is not changed even if the

double-Λ hypernucleus was produced in an excited state or the number of emitted neutrons is larger than one.

In this event, the directions of track #1 and #2 are collinear within the measurement error (5°). Based on a simple phase-space analysis, the probabilities of this topology to occur for the three-body reaction $\Xi^-+{}^{12}\mathrm{C}\rightarrow{}^{11}_{\Lambda\Lambda}\mathrm{Be}+p+n$ and $\Xi^-+{}^{12}\mathrm{C}\rightarrow{}^{10}_{\Lambda\Lambda}\mathrm{Be}+d+n$ were estimated to be about 4% and 6%, respectively, which are not negligible but very small.

7.3 Comparison with past experimental results

As denoted in Chapter 1, three candidates for double-Λ hypernuclei were reported till now[13, 14][15][16]. In the analyses of these events, the mass of the double-Λ hypernucleus was determined from it's decay topology, assuming that the daughter single-Λ hypernucleus was in the ground state. The mass value is increased if the daughter single-Λ hypernucleus was produced in an excited state. The values of $\Delta B_{\Lambda\Lambda}$ obtained from these events are plotted in Fig.7.4 together with the values obtained from the event in this paper. Possible values in the case that the produced daughter single-Λ hypernucleus was in an excited state were also plotted in Fig.7.4 as ${}^{10}_{\Lambda\Lambda}\mathrm{Be}({}^{9}_{\Lambda}\mathrm{Be}^*)$ for the event by Danysz *et al.* and ${}^{13}_{\Lambda\Lambda}\mathrm{B}({}^{13}_{\Lambda}\mathrm{C}^*)$ for the event by E176. The event found in E176 has two interpretations, namely ${}^{13}_{\Lambda\Lambda}\mathrm{B}$ and ${}^{10}_{\Lambda\Lambda}\mathrm{Be}$. In the case of ${}^{10}_{\Lambda\Lambda}\mathrm{Be}$, it was considered that the double-Λ hypernucleus had been produced in two-body fragmentation from the Ξ^- absorption. Therefore, the same analysis can be applied as those in the previous section, i.e. the $\Delta B_{\Lambda\Lambda}$ can be determined from the production topology. The value[1] is plotted as "${}^{10}_{\Lambda\Lambda}\mathrm{Be}$(in this analysis)" in Fig.7.4. It should be noted that the difference of $\Delta B_{\Lambda\Lambda}$ between ${}^{10}_{\Lambda\Lambda}\mathrm{Be}$ and ${}^{13}_{\Lambda\Lambda}\mathrm{B}$ is considered to be smaller than 0.5 MeV (See Table7.4.). The following discussions are not affected if the values of $\Delta B_{\Lambda\Lambda}$ varied by 1.0 MeV depending on the nuclide.

If the double-Λ hypernucleus in the present event was produced in a two-body fragmentation from Ξ^- absorption, which is more likely case, there are two possible values of $\Delta B_{\Lambda\Lambda}$.

case 1) The ${}^{10}_{\Lambda\Lambda}\mathrm{Be}$ nucleus was produced in the ground state.

The $\Delta B_{\Lambda\Lambda}$ is consistent with the value from E176 if their ${}^{13}_{\Lambda\Lambda}\mathrm{B}$ nucleus had decayed to the excited state of ${}^{13}_{\Lambda}\mathrm{C}$ at 4.9 MeV. It is inconsistent both with the one by Danysz *et al.* and the one by Prowse.

case 2) The ${}^{10}_{\Lambda\Lambda}\mathrm{Be}$ nucleus was produced in the excited state at 3.0 MeV.

The $\Delta B_{\Lambda\Lambda}$ is consistent with the value from E176 if their ${}^{13}_{\Lambda\Lambda}\mathrm{B}$ nucleus had decayed to the excited state of ${}^{13}_{\Lambda}\mathrm{C}$ at 4.9 MeV. It is also consistent with

[1]The value and the error are consistent with the sum of the kinetic energy of the double-Λ hypernucleus and the residual nucleus given in Table VIII of Ref.[16].

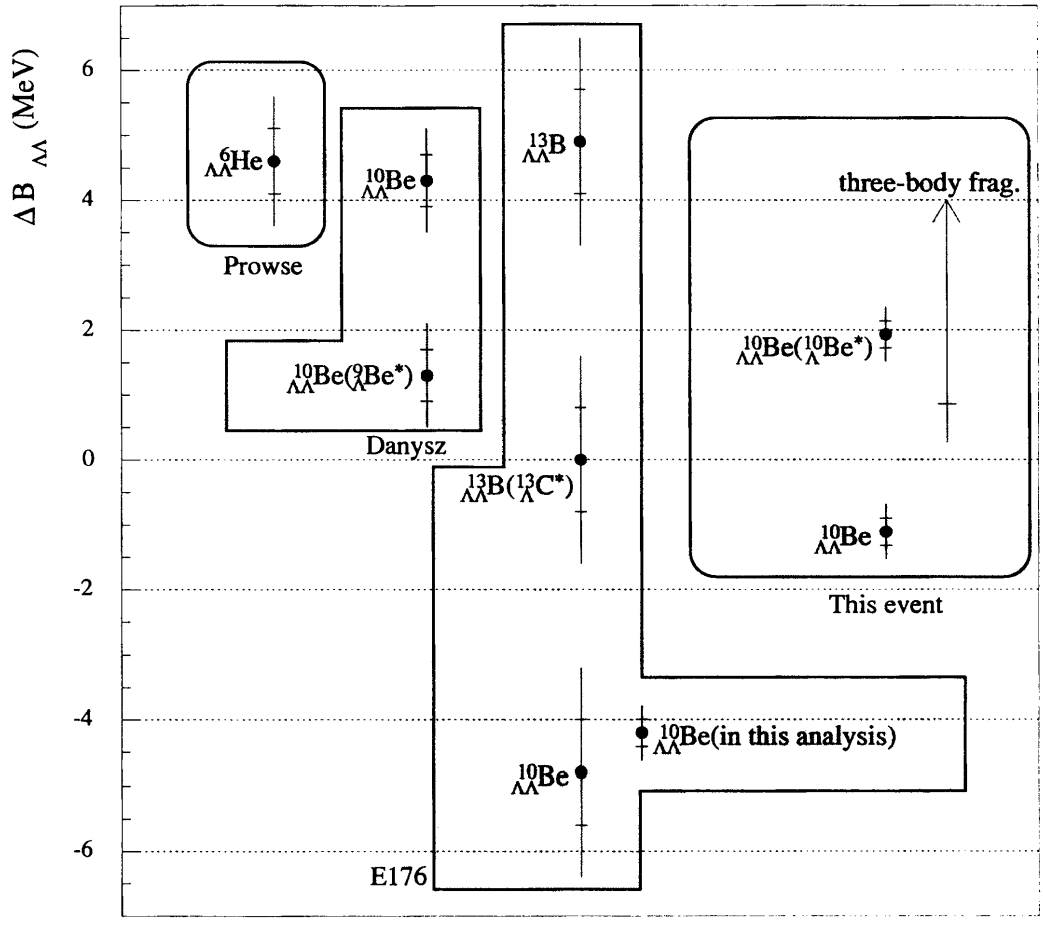

Figure 7.4: Values of $\Delta B_{\Lambda\Lambda}$ obtained from the past three candidates and the present event. The error bars represent the errors in two standard deviations, whereas the small lines on the error bars represent the errors in one standard deviation.

the one by Danysz *et al.* if their ${}^{10}_{\Lambda\Lambda}$Be nucleus had decayed to the excited state of ${}^{9}_{\Lambda}$Be at 3.0 MeV. It is inconsistent with the one by Prowse.

If the double-Λ hypernucleus in the present event was produced accompanied by one or more neutron emissions, which is less likely case, the lower limit of the $\Delta B_{\Lambda\Lambda}$ is consistent with all the values from the past three events except for the ${}^{10}_{\Lambda\Lambda}$Be case of E176. In addition, in the case of the reaction $\Xi^- + {}^{14}\mathrm{N} \rightarrow {}^{13}_{\Lambda\Lambda}\mathrm{B} + p + n$, the value of $\Delta B_{\Lambda\Lambda}$ is consistent if the past two double-Λ hypernucleus (${}^{10}_{\Lambda\Lambda}$Be and ${}^{13}_{\Lambda\Lambda}$B) had decayed to the excited state of the daughter single-Λ hypernucleus.

Combined with the result of E176, the allowed region for $\Delta B_{\Lambda\Lambda}$ are -1.11 ± 0.21 MeV and $+1.93 \pm 0.21$ MeV for ${}^{10}_{\Lambda\Lambda}$Be, and $+4.9 \pm 0.8$ MeV and 0.94 ± 0.47 MeV for ${}^{13}_{\Lambda\Lambda}$B.

7.4 Comparison with theoretical estimates

The binding energy of ΛΛ was calculated in various manner such as few-body approaches using the effective ΛΛ interaction derived from the one-boson-exchange (OBE) models[6][7, 8, 9][10] and the quark-cluster model[11], and relativistic mean field approach[12].

The calculated $\Delta B_{\Lambda\Lambda}$'s are summarized in Table 7.4. The Nijmegen group proposed several types of OBE potentials to describe the baryon-baryon interactions. Model D (NHC-D)[60, 61] and F (NHC-F)[62] are two versions of hard-core OBE potentials. Model NSC[63] is the soft-core OBE potentials and NSC97[64] is their new version. Model F is the latest version of the hard-core OBE potentials and it differs from model D in (i) stronger $SU(3)$ constraints on the hard core radius between various channels, and (ii) inclusion of a scalar-meson nonet. In model D, only the unitary singlet out of the nonet was considered. Instead of the phenomenological hard core, the soft core models, NSC and NSC97, employs Reggeon exchanges, including Pomeron and tensor meson exchanges, which produce short-range repulsive forces. The baryon-baryon-meson vertices are described by coupling constants and Gaussian-type form factors. Out of the several version of the Nijmegen OBE potentials, only model D gives a strong attractive ΛΛ interaction ($\Delta B_{\Lambda\Lambda} \sim 5$ MeV). Other models give rather week interactions.

The $\Delta B_{\Lambda\Lambda}$ was calculated with the core+$(3q)$+$(3q)$ cluster model using the quark-cluster-model (QCM) interactions offered by the Kyoto-Niigata group[65, 66]. In the QCM's, (3q)-(3q) resonating-group-method (RGM) formulation of the spin-flavor $SU(6)$ quark model is employed, and additionally, the effective meson exchange potentials (EMEP) are incorporated to describe the medium and long range forces. In their RGM-F model, EMEP is generated from the scalar-meson nonet exchange in the Nijmegen model-F potential and the tensor component from the π and K mesons. The estimate with RGM-F gives a large overbinding for double-Λ hypernuclei. The EMEP is updated in their FSS model by calculating the spin-flavor factors exactly at the quark level and including

Table 7.4: Theoretical estimates for $\Delta B_{\Lambda\Lambda}$. NHC-D and NHC-F denote the model D and F of the Nijmegen hard-core OBE potential, respectively. NSC denotes the Nijmegen soft-core OBE potential and NSC97 is their new version. RGM-F and FSS are two different versions of Kyoto-Niigata quark cluster model.

few-body cluster calculations			
potential	Ref.	nuclide	$\Delta B_{\Lambda\Lambda}$
NHC-D	[6]	${}^{6}_{\Lambda\Lambda}$He	4.1
	[8]	${}^{10}_{\Lambda\Lambda}$Be	4.26
	[8]	${}^{13}_{\Lambda\Lambda}$B	4.67
NHC-F	[6]	${}^{6}_{\Lambda\Lambda}$He	-6.3
	[8]	${}^{10}_{\Lambda\Lambda}$Be	0.004
	[8]	${}^{13}_{\Lambda\Lambda}$B	-0.08
NSC	[8]	${}^{10}_{\Lambda\Lambda}$Be	1.31
	[8]	${}^{13}_{\Lambda\Lambda}$B	1.47
NSC97	[64]	Much weaker than 4 MeV	
RGM-F	[11]	${}^{10}_{\Lambda\Lambda}$Be	10.6
FSS	[11]	${}^{10}_{\Lambda\Lambda}$Be	2.5
relativistic mean field theory			
model	Ref.	nuclide	$\Delta B_{\Lambda\Lambda}$
$\sigma+\omega$	[12]	${}^{6}_{\Lambda\Lambda}$He	~ 1 MeV
$\sigma+\omega+\sigma^*+\phi$	[12]	${}^{6}_{\Lambda\Lambda}$He	~ 3 MeV

the spin-spin terms originating from all the pseudo-scalar mesons. It gives a somewhat intermediate value for $\Delta B_{\Lambda\Lambda}$.

In the relativistic mean field approach[12], the $\sigma+\omega$ model in which the baryons couple to the mean field of a scalar (σ) and vector (ω, ϕ, ρ) mesons well reproduces spectra of single-Λ hypernuclei. It gives a weakly attractive $\Delta B_{\Lambda\Lambda}$ (~ 1 MeV). They claim that the coupling to an additional scalar (σ^*) and vector (ϕ) fields increase $\Delta B_{\Lambda\Lambda}$ and their $\sigma+\omega+\sigma^*+\phi$ model gives a rather strong attractive $\Delta B_{\Lambda\Lambda}$ (~ 3 MeV).

Chapter 8

Discussion about production rate

Combined with the results of the E176 experiment, two double-Λ hypernuclei and three twin-hypernuclei events have been found from Ξ^- hyperon captures on light emulsion nuclei. The ratio of the detected rate for double-Λ hypernuclei to twin-hypernuclei events is therefore 0.67 with the 90% confidence interval lying from 0.14 to 3.9. Although the number of Ξ^- stopping events has some error due to the contamination of various background such as miss-identification of σ-stop, Σ^--stopping event, etc, double-Λ hypernucleus events and twin-hypernuclei events are almost background free. Therefore, we compare the ratio of their detected rate with theoretical estimates to extract some information.

There are several theoretical calculations estimating the production probability of double-Λ hypernuclei[67][68][69][70] and of twin-hypernuclei events[68][69][70]. These calculations use an attractive $\Lambda\Lambda$ interaction ($\Delta B_{\Lambda\Lambda} = 4 \sim 5$ MeV), except Ref.[68], in which both attractive and repulsive interactions ($\Delta B_{\Lambda\Lambda} = -4.9$ MeV) were considered. The results of these calculations are summarized in table 8.1. The ratio of the production rate of double-Λ hypernuclei to twin-hypernuclei is larger than 5 with an attractive $\Lambda\Lambda$ interaction. This characteristics is naively explained by considering the phase space available for each channel. Figure 8.1 shows the energy levels of various fragmentation channels from a Ξ^-+^{12}C system. In the case of $\Delta B_{\Lambda\Lambda} = 4.9$ MeV (attractive), the Q-values to produce double-Λ hypernuclei are much larger than those for twin-hypernuclei. However, if $\Delta B_{\Lambda\Lambda} = -4.9$ MeV (repulsive), the Q-values for the two types become comparable and the ratio is decreased.

The present experimental value of 0.67 (90%CI [0.14,3.9]) deviates from the theoretical estimates using an attractive $\Lambda\Lambda$ interaction ($\Delta B_{\Lambda\Lambda} = 4.9$ MeV) given in table 8.1. However, to compare with the theoretical estimates, the difference of the detection efficiency between double-Λ hypernuclei and twin-hypernuclei events must be considered. Following four cases are considered to be the main origin of the detection inefficiency.

a) If a hypernucleus decays in a neutral mode ($\Lambda \rightarrow \pi^0 n$ or $\Lambda n \rightarrow nn$) and only one or no track of the residual nucleus is visible, the identification is difficult. Both a double-Λ hypernucleus and a twin-hypernuclei emission

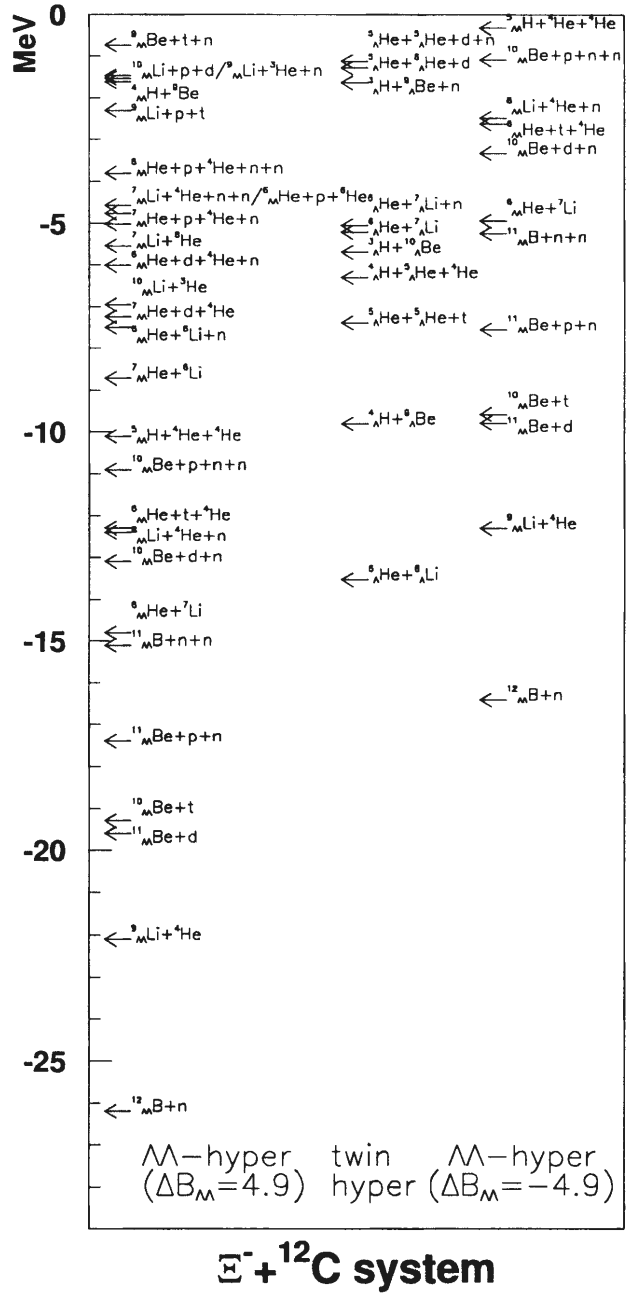

Figure 8.1: Energy levels of various systems measured from a Ξ^-+^{12}C state. The masses of double-Λ hypernuclei were calculated from $\Delta B_{\Lambda\Lambda}$.

Table 8.1: Theoretical estimations for the production probability of double-Λ hypernuclei and twin-hypernuclei, and their ratio. In Ref.[68], those from the compound states, ${}^{13}_{\Lambda\Lambda}\mathrm{B}^*$, ${}^{15}_{\Lambda\Lambda}\mathrm{C}^*$ and ${}^{17}_{\Lambda\Lambda}\mathrm{N}^*$, formed after a Ξ^- hyperon capture had been calculated. Quoted here are the values averaged with the weights of the molar ratio of ${}^{12}\mathrm{C}$, ${}^{14}\mathrm{N}$ and ${}^{16}\mathrm{O}$ in the emulsion. The values from Ref.[69][70] are those from $\Xi^-+{}^{12}\mathrm{C}$ atomic states. Only two body decay channels are considered in [69]. The parenthesized values are those excluding the fragmentation channels in which a double-Λ hypernucleus and only neutrons are emitted, like $\Xi^-+{}^{12}\mathrm{C}\rightarrow{}^{12}_{\Lambda\Lambda}\mathrm{B}+n$.

model	double-hyp. (exc. one charge frag.)	twin-hyp.	ratio
statistical decay (attractive)[68]	70% (57%)	12%	5.8 (4.8)
statistical decay (repulsive)[68]	30% (21%)	28%	1.1 (0.75)
doorway decay[69]	4.8% (3.3%)	0.11%	43 (30)
AMD-QL[70]	11.4% (9.8%)	1.2%	9.5 (8.2)

have two decay vertices. The inefficiencies due to the neutral decay are, therefore, considered to be the same.

b) If the distance between two decay vertices is very short, the separation is difficult. With the attractive $\Delta B_{\Lambda\Lambda}$ (4.9 MeV), Q-values for double-Λ hyperfragment channels are large and the range of a double-Λ hypernucleus is expected to be longer than that of a hypernucleus of the same mass number from a twin-hypernuclei event. As for the range of a daughter hypernucleus from a double-Λ hypernucleus, the range can become short when the parent nucleus decays in a mesonic mode. The branching ratio for the mesonic decay modes for such hypernuclei is expected to be about 20% from the data on single-Λ hypernuclei. The present discrepancy cannot be explained this way.

c) If a double-Λ hypernucleus and only neutrons are emitted from a Ξ^- stopping point like $\Xi^-+{}^{12}\mathrm{C}\rightarrow{}^{12}_{\Lambda\Lambda}\mathrm{B}+n$, the detection is also difficult. In table 8.1, the estimated production rates without these modes are also listed. Even without these modes, there is still a discrepancy between the present result and the theoretical estimations using an attractive $\Lambda\Lambda$ interaction.

d) When a double-Λ hypernucleus decays, the remaining Λ can escape from the nucleus. Especially in non-mesonic modes, the escaping probability might be high due to the large Q-values. In such a case, the identification as a double-Λ hypernucleus is almost impossible with emulsion. If the escaping probability for the remaining Λ is larger than 30%, the ratio of the detected

rates doesn't contradict the theoretical estimates by the statistical decay model with an attractive $\Lambda\Lambda$ interaction.

Consequently, the present result is suggesting that the remaining Λ at the first decay of a double-Λ hypernucleus can escape with a probability as high as 30% if the $\Delta B_{\Lambda\Lambda}$ is really about 5 MeV. And yet there are large discrepancies between the present result and the theoretical estimates by the doorway-decay model and the AMD-QL model. These discrepancy can be easily explained if the $\Delta B_{\Lambda\Lambda}$ is much weaker than 5 MeV.

The E373 experiment can detect escaping Λ's with the SciFi-block detectors with some probability.

The signals would appear in the image of the SciFi-detectors for the events having the topology of the single-Λ hypernucleus production from the Ξ^- capture as an unusually high-momentum Λ which can be produced via the non-mesonic decay of $\Lambda\Lambda \rightarrow \Lambda n$ in a double-Λ hypernucleus, or a Λ whose energy is too large to be produced from the Ξ^- capture point.

Chapter 9

Conclusion

A hybrid emulsion experiment KEK-PS E373 was carried out to study double-strangeness nuclei produced via Ξ^- hyperon capture at rest with the expectation of ten times larger statistics than previous experiments. The experiment was performed at the KEK proton synchrotron using a 1.66 GeV/c separated K^- beam and 69 l emulsion. The Ξ^- hyperons were produced in a diamond target via the (K^-, K^+) reaction and were brought to rest in the emulsion. The (K^-, K^+) reaction was tagged by the spectrometer system. The position and angle of the Ξ^- hyperon track was measured by the high-resolution tracking detector using scintillating microfibers. The two scintillating mono-fiber blocks located both upstream and downstream of the emulsion were used to select events in which the Ξ^- hyperons are likely to be stopped in the emulsion. For the selected events, tracks of the Ξ^- candidates were searched for and traced in the emulsion by a newly-developed automatic track scanning system. In the 1998 run, totally 2.7×10^9 K^-'s were delivered to the diamond target and emulsion, and 4.6×10^4 (K^-, K^+) reaction events were obtained.

Until now, 6% of the total emulsion has been analyzed. We found one twin Λ hypernuclei event and one double-Λ hypernucleus at Ξ^- hyperon stopping points. The two events were reconstructed kinematically using the information about the ranges and angles of the tracks.

The twin-hypernuclei event was interpreted as the fragmentation from a $\Xi^-+{}^{14}$N atomic state to ${}^{5}_{\Lambda}$He+${}^{5}_{\Lambda}$He+^{4}He+n. The binding energy of the Ξ^- hyperon is -2.6 ± 1.2 MeV. The species of the Ξ^--atom and the fragmentation products were uniquely identified for the first time for twin-hypernuclei events.

The double-Λ hypernucleus was produced accompanied by one charged particle from a Ξ^- hyperon stopping point. The track of the double-Λ hypernucleus and that of the residual particle are collinear within the measurement error. If a two-body decay from the Ξ^- capture is assumed, the event is uniquely identified as,

$$\Xi^- + {}^{12}\mathrm{C} \rightarrow {}^{10}_{\Lambda\Lambda}\mathrm{Be} + t.$$

Taking a value of $0.1^{+0.1}_{-0.05}$ MeV for the binding energy of the Ξ^- hyperon when

the absorption had occur-ed, the binding energy ($B_{\Lambda\Lambda}$) and interaction energy ($\Delta B_{\Lambda\Lambda}$) of the $\Lambda\Lambda$ are determined. The $B_{\Lambda\Lambda}$ and $\Delta B_{\Lambda\Lambda}$ are 12.31±0.21 MeV and -1.11 ± 0.21 MeV, respectively if it was produced in the ground state. If it was produced in the excited state at 3.0 MeV, then $B_{\Lambda\Lambda}$ and $\Delta B_{\Lambda\Lambda}$ are 15.35±0.21 MeV and 1.93±0.21 MeV, respectively. If the fragmentation involved neutrons, the nuclide was not determined uniquely and the lower limit for $\Delta B_{\Lambda\Lambda}$ was obtained as 1.4 MeV. Based on a simple phase-space analysis, the probabilities of the present topology to occur for the three-body reaction was estimated to be $4 \sim 6\%$. Combined with the result of E176, the allowed region for $\Delta B_{\Lambda\Lambda}$ are -1.11 ± 0.21 MeV and $+1.93 \pm 0.21$ MeV for ${}^{10}_{\Lambda\Lambda}$Be, and $+4.9 \pm 0.8$ MeV and 0.94 ± 0.47 MeV for ${}^{13}_{\Lambda\Lambda}$B.

In the experiments E176 and E373, two double-Λ hypernuclei and three twin-hypernuclei events have been found from Ξ^- hyperon captures on light emulsion nuclei. The ratio of the observation rate for double-Λ hypernuclei to twin-hypernuclei events is therefore 0.67 with the 90% confidence interval lying from 0.14 to 3.9. It is consistent with a theoretical estimation using a repulsive $\Lambda\Lambda$ interaction, and is much smaller than those using a strongly attractive $\Lambda\Lambda$ interaction with ($\Delta B_{\Lambda\Lambda} \sim 5$ MeV). The discrepancy will be reduced if the $\Lambda\Lambda$ interaction is weak ($\Delta B_{\Lambda\Lambda} \sim\leq 1$ MeV). The detection inefficiency for double-Λ hypernuclei due to the escape of the remaining Λ at the first decay may explain the deviation.

Finally, we would like to stress that we have overcome the experimental difficulties for the ambitious challenge to stop one thousand Ξ^- hyperons in nuclear emulsion by adopting the diamond target, scintillating fiber, spectrometer and nuclear emulsion hybrid system. Although the analysis is still under way, we can see the light at the end of the tunnel with the success of the development of the automatic emulsion scanning system. We believe that even ten times larger, i.e. ten thousands stopping Ξ^-'s can be obtained with these systems in near future. It will enable us to make a nuclear chart with $S = -2$.

Acknowledgement

It is my great pleasure to acknowledge the collaboration, advice, support and encouragement given by many people to complete the present work.

I would like to express my sincere gratitude to my supervisor, Prof. Ken'ichi Imai for his guidance, advice and especially encouragement. I have been impressed by his talent to create many ideas and been encouraged to make new ideas by myself.

I am deeply grateful to the spokesperson of the experiment, Prof. Kazuma Nakazawa from Gifu University for his continuous support for my working on the experiment.

The execution of the experiment described in this paper has been a combined effort of many individuals in the KEK-PS E373 collaboration. I am deeply grateful to these people for their collaboration. In particular, I would like to express my thanks to K. Yamamoto, Y. Kondo, H. Akikawa, D. Seki, H. Takahashi, H. Torii, and C. J. Yoon from Kyoto University, H. Tanaka from Aichi University of Education, and Y. H. Iwata, Y. S. Iwata, M. Mitsuhara and Y. Nagase from Gifu University. They were my coworkers and support me many times during the experiment. I enjoyed the preparation and execution of the experiment with them. Especially this work could not be completed without the supports by Mr. Hitoshi Takahashi, Hideyuki Tanaka and Hisayuki Torii. Dr. Kazuhiro Yamamoto guided me to experiments and support me during my years in graduate school. The support and advices by Mr. J. Tojo, M. Yosoi and L. Zhu from Kyoto University, H. M. Park, Y. S. Ra from Gifu University, H. Shibuya, K. Arai, K. Oyama from Toho University, F. Takeuti from Kyoto-Sangyo University, K. Tanida and N. Yasuda from University of Tokyo, K. M. Baik and K. S. Sim from Korea University, J. S. Song from Gyeongsang National University, H. Okabe from Osaka Prefectural Education Center are greatly acknowledged. I am appreciate to Dr. M. Ieiri from KEK for his support to tune the beamline, S. Aoki for the construction of the CCD DAQ system and T. Yoshida for the construction of the detectors. Prof. B. Bassalleck from University of New Mexico and Dr. A. Rusek from Brookhaven National Laboratory supported and encouraged me during the beamtime, and also taught me English grammar. Mr. T. Kawai and K .Hoshino support the construction of the emulsion mover system. I would like to acknowledge also the technical support of peoples at KEK-PS.

I spent invaluable and enjoyable years in the graduate school. I wish to thank all the members from "Experimental Nuclear Physics" group and "Parti-

cle and Nuclei" group in addition to the newly founded "Experimental Nuclear and Hadronic Physics" group for their hospitality and memberships. I am appreciate to Prof. Hideyo En'yo for his continuous encouragement and helpful advices on various subjects. Valuable discussions with Prof. Harutaka Sakaguchi and Masanobu Nakamura and Dr. Tetsuya Murakami, Masaru Yosoi, Haruhiko Funahashi are greatly acknowledged. Some of the members of KEK-PS E289 (SigN) (M. Yoshida and H. Kanda), E325 (ϕ) (S. Yokkaichi, S. Mihara, M. Ishino, K. Ozawa, T. Tabaru) and E337(Multi) (J. Murata) experiments helped me during the preparation and execution of our experiment. I spent enjoyable time with them at KEK. Dr. Sin'ya Sawada, Satoshi Mihara, Toshiyuki Takahashi, Yuji Goto and Ms. Mari Hayashi-Sawada introduced me the life in a graduate school. The secretarial and coffee-break support by Ms. Yuka Nakakoji-Sasaki and Terue Kiyosawa-Ishino are greatly acknowledged.

I am deeply appreciated to Dr. Yasuhiro Kondo. He supported me not only in the research but also in my whole life through out my time in graduate school. I have spent so happy time with him. Finally I would address my heartfelt thanks to my parents, sister and brother for their continuous patient support.

Appendix A

Connection of tracks from Fiber-bundle to emulsion

In order to determine the search condition for the emulsion plate #1 scanning, the precision of the connection of tracks from Fiber-bundle to plate #1 was evaluated by connecting sample tracks.

The sample tracks were selected by the following procedure. Among the event data obtained during the normal runs, the cut with the Fiber-bundle brightness was applied in the same manner as that described in Sec.3.2.2 for the events whose image dose not overlap with others. The image of the selected events were scanned by human eyes. The events in which just one highly ionizing particle passed through the Fiber-bundle were selected and the position and angle of the tracks were determined in the same way as that described in Sec.3.2.2. Among them, tracks whose angle (θ) satisfy the condition, $0.4 < \tan\theta < 1.0$ were finally selected because in this angular region, the multiplicity of track candidates found in the emulsion is moderate. The relative position between Fiber-bundle and plate #1 was determined using the X-ray marks. However, during the '98 run, due to the trouble of the emulsion mover, horizontal position of the mover stage measured with the linear encoder had a systematic error of about 100 μm depending on the direction of the movement in horizontal. The magnitude of the systematic error was estimated from the position of X-ray marks at four corners. Therefore an offset value was added for the horizontal position measured after the stage had moved in the left direction.

For the selected tracks, the corresponding tracks were searched for in the plate #1 in the area of 900×900 μm^2 around the expected position. As described in Sec.4.3, the area is divided into regions of about one picture size ($\sim 110\times90\mu m^2$). Tracks were searched for at each region with the automatic track scanning algorithm described in Sec.4.1.2 in the region of ±0.1 ($\tan\theta$) around the angle calculated by the following equations,

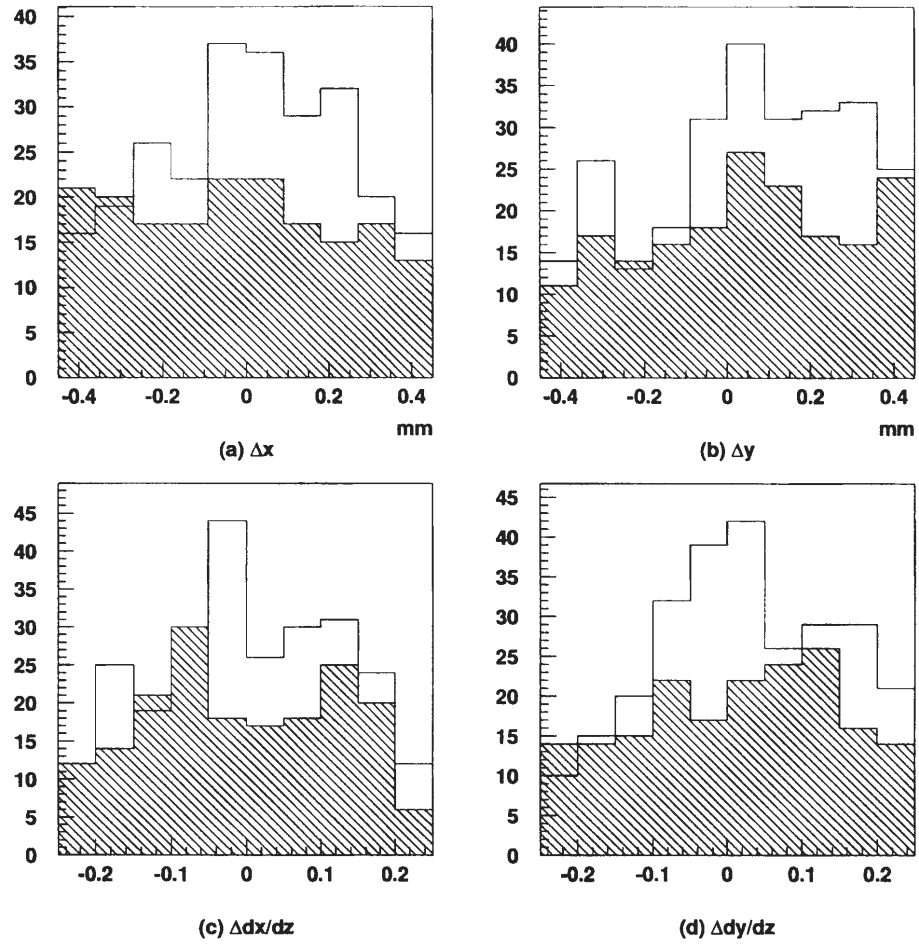

Figure A.1: Differences of position ((a),(b)) and angle((c),(d)) of the found tracks from the predicted values. Hatched areas correspond to those obtained with the "dummy scan".

$$\begin{aligned} &\frac{dx}{dz}|_{\text{pred}} + \frac{(X_0 - x_{\text{pred}})}{L}, \\ &\frac{dy}{dz}|_{\text{pred}} + \frac{(Y_0 - y_{\text{pred}})}{L}, \end{aligned} \tag{A.1}$$

where $(\frac{dx}{dz}|_{\text{pred}}, \frac{dy}{dz}|_{\text{pred}})$ and $(x_{\text{pred}}, y_{\text{pred}})$ represent the angle (slopes) and position predicted by Fiber-bundle. The (X_0, Y_0) is the center position of the searching region, and L is the distance between the Fiber-bundle and the plate #1 ($\sim$ 2.2 mm). With these equations, the angle was corrected depending on the position of the searching region, thinking that due to the error of the predicted angle

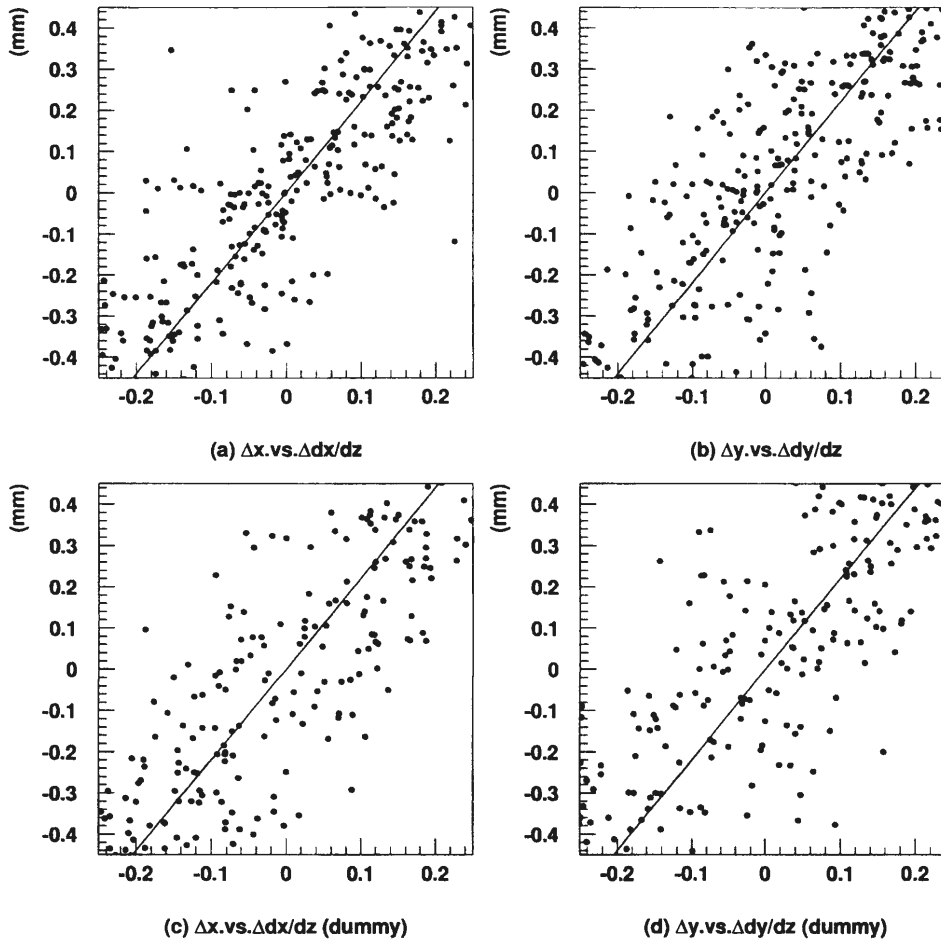

Figure A.2: Upper two plot shows correlation between the discrepancy in the position and that in the angle. The lower two plots are those obtained with the "dummy scan"

$(\Delta\frac{dx}{dz}, \Delta\frac{dy}{dz})$, the predicted position is displaced from the real position by $(\Delta\frac{dx}{dz} \times L, \Delta\frac{dy}{dz} \times L)$.

Tracks were also searched at the position shifted from the predicted place by 3 mm in order to estimate the contribution from the background tracks. This is called as "dummy scan".

Figure A.1 shows distributions of the differences of position and angle of the found tracks from the predicted values together with those obtained with the "dummy scan". Compared with the distribution obtained with the "dummy scan", signals from the really corresponding tracks can be seen.

Figure A.2 shows the correlation between the discrepancy in the position and the discrepancy in the angle. This relation indicates that a part of the positional

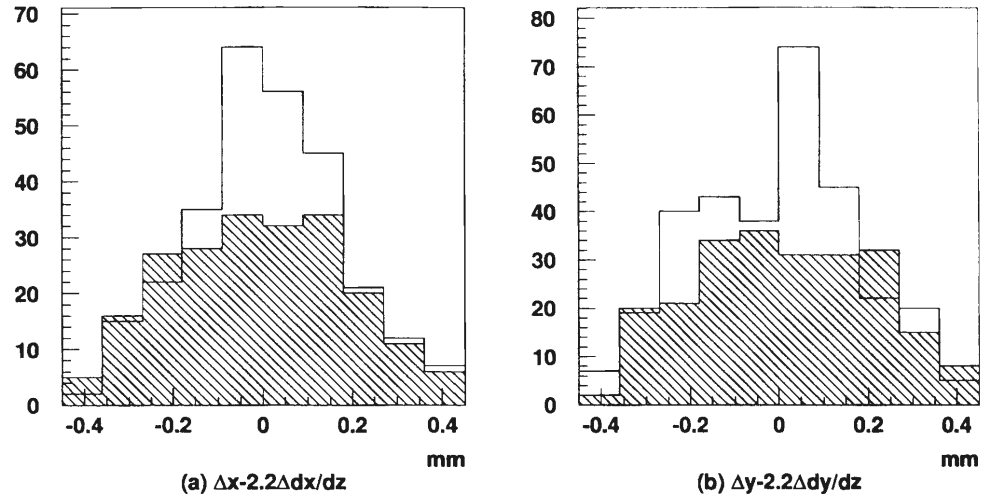

Figure A.3:

error is due to the angular error, because there was a gap between the fiber bundle sheets and the emulsion. This correlation is consistent with the relation,

$$\Delta x = L \times \Delta\frac{dx}{dz}, \Delta y = L \times \Delta\frac{dy}{dz}, \tag{A.2}$$

where $(\Delta x, \Delta y)$ and $(\Delta\frac{dx}{dz}, \Delta\frac{dy}{dz})$ are the discrepancy of the position and angle of the found tracks from the prediction. The weak correlation seen in Figs.A.2(c) and (d) obtained with the "dummy scan" is due to the angle correction by Eq.A.1 at the scanning.

FigureA.3 shows the discrepancy of position remained after the angle correction, $(\Delta x - 2.2\Delta\frac{dx}{dz}, \Delta y - 2.2\Delta\frac{dy}{dz})$.

From these results, we set the search condition for plate #1 scanning as,

$$\begin{aligned}
-0.45 < \quad & \Delta x(\mathrm{mm}) & < 0.45, \\
-0.45 < \quad & \Delta y(\mathrm{mm}) & < 0.45, \\
-0.1 < \quad & \Delta\tfrac{dx}{dz}|_{\mathrm{cor}} & < 0.1, \\
-0.1 < \quad & \Delta\tfrac{dy}{dz}|_{\mathrm{cor}} & < 0.1, \\
-0.3 < \quad & \Delta x - L \times \Delta\tfrac{dx}{dz} & < 0.3, \\
-0.3 < \quad & \Delta y - L \times \Delta\tfrac{dy}{dz} & < 0.3,
\end{aligned}$$

where $(\frac{dx}{dz}|_{\mathrm{cor}}, \frac{dy}{dz}|_{\mathrm{cor}})$ is the corrected angle for the search region using Eq.A.1 and $(\frac{dx}{dz}, \frac{dy}{dz})$ is the angle predicted by Fiber-bundle.

Bibliography

[1] R. Jaffe, Phys. Rev. Lett. **38**, 195 (1977).

[2] T. Sakai, K. Shimizu, and K. Yazaki, Prog. Theor. Phys. Suppl. **137**, 121 (2000), `nucl-th/9912063`.

[3] R. E. Chrien, Nucl. Phys. **A629**, 388C (1998).

[4] B. Bassalleck, Nucl. Phys. **A639**, 401 (1998).

[5] B. O. Kerbikov, Yad. Fiz. **39**, 816 (1984).

[6] H. Bando, Prog. Theor. Phys. **67**, 699 (1982).

[7] Y. Yamamoto, H. Takaki, and K. Ikeda, Prog. Theor. Phys. **86**, 867 (1991).

[8] Y. Yamamoto, T. Motoba, H. Himeno, K. Ikeda, and S. Nagata, Prog. Theor. Phys. Suppl. **117**, 361 (1994).

[9] H. Himeno, T. Sakuda, S. Nagata, and Y. Yamamoto, Prog. Theor. Phys. **89**, 109 (1993).

[10] S. B. Carr, I. R. Afnan, and B. F. Gibson, Nucl. Phys. **A625**, 143 (1997), `nucl-th/9709003`.

[11] T. Yamada and C. Nakamoto, Phys. Rev. **C62**, 034319 (2000).

[12] J. Schaffner *et al.*, Ann. Phys. **235**, 35 (1994).

[13] M. Danysz *et al.*, Nucl. Phys. **49**, 121 (1963).

[14] R. H. Dalitz *et al.*, Proc. Roy. Soc. Lond. **A426**, 1 (1989).

[15] D. J. Prowse, Phys.Rev.Lett. **17**, 782 (1966).

[16] S. Aoki *et al.*, Prog. Theor. Phys. **85**, 1287 (1991).

[17] N. Ushida *et al.*, Nucl. Instrum. Meth. **A224**, 50 (1984).

[18] S. Aoki *et al.*, Nucl. Instrum. Meth. **A274**, 64 (1989).

[19] K. Kodama *et al.*, Nucl. Instrum. Meth. **A289**, 146 (1990).

[20] E. Eskut *et al.* (CHORUS), Nucl. Instrum. Meth. **A401**, 7 (1997).

[21] M. Nakamura (DONUT), Nucl. Phys. Proc. Suppl. **77**, 259 (1999).

[22] M. Guler *et al.* (OPERA) CERN-SPSC-2000-028.

[23] C. B. Dover, D. J. Millener, A. Gal, and D. H. Davis, Phys. Rev. **C44**, 1905 (1991).

[24] S. Aoki *et al.*, Prog. Theor. Phys. **89**, 493 (1993).

[25] S. Aoki *et al.*, Phys. Lett. **B355**, 45 (1995).

[26] T. Iijima *et al.*, Nucl. Phys. **A546**, 588 (1992).

[27] C. B. Dover and A. Gal Brookhaven Nat. Lab. Upton - BNL-31728 (REC.SEP.82) 75p.

[28] A. Yamamoto *et al.*, Nucl. Instr. Meth. **203**, 35 (1982).

[29] M. Ishino *et al.*, Nucl. Instr. Meth. **457**, 581 (2001).

[30] D. E. Alburger and M. May, Nucl. Instrum. Meth. **A443**, 27 (2000).

[31] S. Yamashita, *H-Dibaryon Search via* (K^-, K^+) *Reactions in Scintillating Fiber Traget*, Ph.D. thesis, Kyoto University (1995).

[32] H. Torii, Master's thesis, Kyoto University (1995).

[33] C. Angelini *et al.* (WA84), Nucl. Instrum. Meth. **A289**, 342 (1990).

[34] C. Angelini *et al.* (WA84), Nucl. Instrum. Meth. **A295**, 299 (1990).

[35] M. Adinolfi *et al.* (A84), Nucl. Instrum. Meth. **A310**, 485 (1991).

[36] M. Adinolfi *et al.*, Nucl. Instrum. Meth. **A315**, 67 (1992).

[37] C. D'Ambrosio, T. Gys, H. Leutz, U. Gensch, and S. Schlenstedt, Nucl. Instrum. Meth. **A322**, 20 (1992).

[38] C. D'Ambrosio, H. Leutz, T. Shimizu, and O. Shinji, Nucl. Instrum. Meth. **A325**, 161 (1993).

[39] C. D'Ambrosio *et al.*, Nucl. Instrum. Meth. **A332**, 134 (1993).

[40] P. Destruel *et al.*, Nucl. Instrum. Meth. **A276**, 69 (1989).

[41] C. D'Ambrosio *et al.*, Nucl. Instrum. Meth. **A307**, 430 (1991).

[42] B. Baumbaugh *et al.*, Nucl. Instrum. Meth. **A345**, 271 (1994).

[43] A. Ichikawa *et al.*, Nucl. Instrum. Meth. **A417**, 220 (1998).

[44] H. Takahashi, Master's thesis, Kyoto University (1996).

[45] H. Takahashi *et al.*, to be submitted to Nucl. Instrum. Meth. .

[46] H. Akikawa *et al.*, will be submitted to Nucl. Instrum. Meth. .

[47] H. Tanaka, Master's thesis, Aichi University of Education (1995).

[48] Y. Kondo, *Measurement of $\Sigma^- p$ Elastic Scattering Cross Sections with a Scintillating-Fiber Active Target*, Ph.D. thesis, Kyoto University (2000).

[49] H. Takahashi, Ph.D. thesis, Kyoto University, to be written.

[50] T. K. Ohsuka *et al.*, KEK report 85-10, KEK (1985).

[51] Y. Itow, *Search for H dibaryon in $\Sigma^- p$ decay with scintillating fiber target as triggerable visual detector*, Ph.D. thesis, Kyoto University (1995).

[52] S. Aoki *et al.*, Nucl. Instrum. Meth. **B51**, 466 (1990).

[53] S. Aoki *et al.* To be submitted.

[54] J. F. Ziegler and J. P. Biersack, *Srim-2000* (2000), ©IBM Co.

[55] C. F. Powell, P. H. Fowler, and D. H. Perkins, *The Study of Elementary Particles by the Photographic Method* (Pergamon Press, 1959), and references in there.

[56] J. F. Ziegler, J. P. Biersack, and U. Littmark, *THE STOPPING AND RANGE OF IONS SOLIDS* (Pergamon Press, 1985).

[57] H. H. Heckman *et al.*, Phys. Rev. **117**, 544 (1960).

[58] C. J. Batty, E. Friedman, and A. Gal, Phys. Rev. **C59**, 295 (1999), `nucl-th/9809042`.

[59] H. Akikawa, Ph.D. thesis, Kyoto University, to be published.

[60] M. M. Nagels, T. A. Rijken, and J. J. de Swart, Phys. Rev. **D12**, 744 (1975).

[61] M. M. Nagels, T. A. Rijken, and J. J. de Swart, Phys. Rev. **D15**, 2547 (1977).

[62] M. M. Nagels, T. A. Rijken, and J. J. de Swart, Phys. Rev. **D20**, 1633 (1979).

[63] P. M. M. Maessen, T. A. Rijken, and J. J. de Swart, Phys. Rev. **C40**, 2226 (1989).

[64] T. A. Rijken, V. G. J. Stoks, and Y. Yamamoto, Phys. Rev. **C59**, 21 (1999), `nucl-th/9807082`.

[65] Y. Fujiwara, C. Nakamoto, and Y. Suzuki, Phys. Rev. Lett. **76**, 2242 (1996).

[66] Y. Fujiwara, C. Nakamoto, and Y. Suzuki, Phys. Rev. **C54**, 2180 (1996).

[67] D. Zhu, C. B. Dover, A. Gal, and M. May, Phys. Rev. Lett. **67**, 2268 (1991).

[68] M. Sano, M. Wakai, and Y. Yamamoto, Prog. Theor. Phys. **87**, 957 (1992).

[69] T. Yamada and K. Ikeda, Phys. Rev. **C56**, 3216 (1997).

[70] Y. Hirata, Y. Nara, A. Ohnishi, T. Harada, and J. Randrup, Prog. Theor. Phys. **102**, 89 (1999), `nucl-th/9711063`.

List of Tables

List of Figures